Interannual and Decadal Variability in the Air-Sea Exchange of CO_2 - a Model Study

Patrick Wetzel

Hinweis

Die Berichte zur Erdsytemforschung werden vom Max-Planck-Institut für Meteorologie in Hamburg in unregelmäßiger Abfolge heraus-gegeben.

Sie enthalten wissenschaftliche und technische Beiträge, inklusive Dissertationen.

Die Beiträge geben nicht notwendigerweise die Auffassung des Instituts wieder.

Die "Berichte zur Erdsystemforschung" führen die vorherigen Reihen "Reports" und "Examensarbeiten" weiter.

Notice

The Reports on Earth System Science are published by the Max Planck Institute for Meteorology in Hamburg. They appear in irregular intervals.

They contain scientific and technical contributions, including Ph. D. theses.

The Reports do not necessarily reflect the opinion of the Institute.

The "Reports on Earth System Science" continue the former "Reports" und "Examensarbeiten" of the Max Planck Institute.

Anschrift / Address

Max-Planck-Institut für Meteorologie
Bundesstrasse 53
20146 Hamburg
Deutschland

Tel.: +49-(0)40-4 11 73-0
Fax: +49-(0)40-4 11 73-298
Web: www.mpimet.mpg.de

Layout:

Bettina Diallo, PR & Grafik

Titelfotos:
vorne:
Christian Klepp - Jochem Marotzke - Christian Klepp
hinten:
Katsumasa Tanaka - Christian Klepp - Clotilde Dubois

Interannuale und Dekadische Variabilität im CO$_2$ Austausch zwischen Ozean und Atmosphäre - eine Modell Studie

Interannual and Decadal Variability in the Air-Sea Exchange of CO$_2$ - a Model Study

Dissertation zur Erlangung des Doktorgrades der Naturwissenschaften
im Fachbereich Geowissenschaften der Universität Hamburg
vorgelegt von

Patrick Wetzel
aus Freiburg

Hamburg 2004

Patrick Wetzel
Max-Planck-Institut für Meteorologie
Bundesstrasse 53
20146 Hamburg
Germany

Interannual and Decadal Variability
in the Air-Sea Exchange of CO_2
- a Model Study
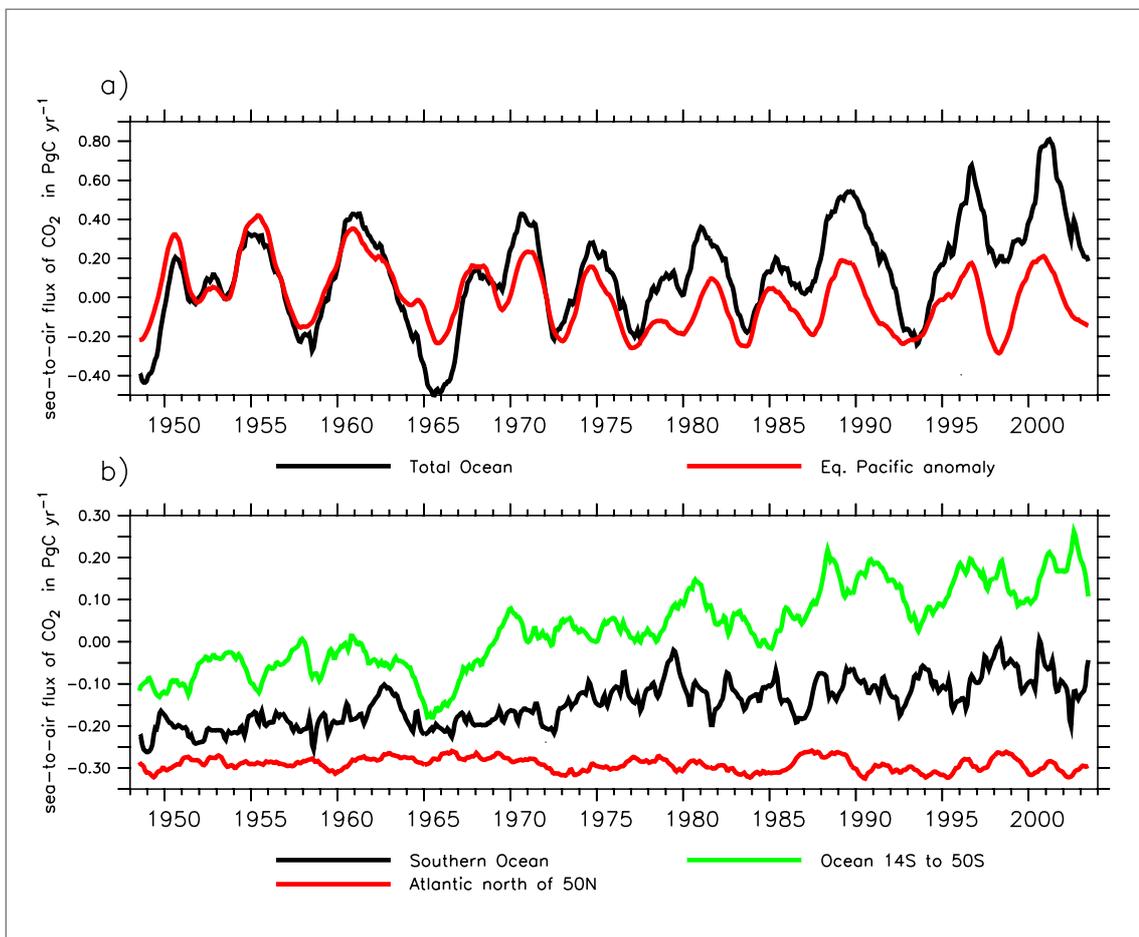
Patrick Wetzel

Hamburg 2004

CONTENTS

Abstract

Trends and variability in the ocean-atmosphere CO_2-flux and the uptake of anthropogenic CO_2 are simulated for the period 1948-2003, using a biogeochemical carbon cycle model (HAMOCC5) coupled on-line to a global Ocean General Circulation Model (MPI-OM). The coupled model is forced by daily NCEP/NCAR reanalysis data. The NCEP/NCAR reanalysis is a consistent set of atmospheric data from 1948 until today and shows trends and variability on interannual and decadal timescales. For the first time it is thus possible to analyze the physical and biological processes that drive the air-sea CO_2 fluxes on long timescales and in non-equilibrium conditions.

The simulated total interannual variability is ± 0.50 PgC yr^{-1} ($2\,\sigma$) and is largely dominated by ocean dynamics in the equatorial Pacific (65 %). In addition to the interannual variability, the Pacific climate also undergoes decadal-scale shifts with effects on the sea surface temperature and the trade winds. Because of the regime shift in 1975-1977, the modeled interannual variability of the equatorial Pacific changes from ± 0.32 PgC yr^{-1} to ± 0.23 PgC yr^{-1}. The Southern Ocean accounts for over 20% of the interannual CO_2 flux variability, which is mostly controlled by the winter mixed layer depth. Although one third of the global uptake of anthropogenic carbon occurs in the Southern Ocean, little anthropogenic CO_2 is actually stored there. Half of the anthropogenic CO_2 taken up by the Southern Ocean in the simulation is transported northward into the subtropical convergence zone. Trends in the modeled CO_2 fluxes over the 56 years period are caused by the increasing wind speed forcing, mostly over the southern hemisphere. We estimate an average CO_2 flux into the ocean of 1.74 PgC yr^{-1} for 1990 to 1999 which consists of an anthropogenic component of 1.91 PgC yr^{-1} and a flux of 0.17 PgC yr^{-1} out of the ocean from variablity within the physical forcing. The extremes are 1.20 PgC yr^{-1} at the La Niña event in 1996 and 2.10 PgC yr^{-1} during the El Niño events in 1993 and 1998. As a consequence of the rising CO_2 concentrations the upper ocean becomes more acidic. This slows down the uptake of anthropogenic CO_2 towards the end of the simulation. Overall about 124 Pg of anthropogenic carbon accumulated the simulation in the model ocean by the end of 2003. The inclusion of the effect of iron limitation on the biological production significantly changes the behavior of the model. It strengthens the south-north gradient by limiting the production on the Southern Ocean and lowers the interannual variability by altering the distribution of dissolved inorganic carbon (DIC) in the Southern Ocean and the equatorial Pacific.

Zusammenfassung

Gegenstand dieser Arbeit ist die interannuale bis dekadische Variabilität im CO_2 Gasaustausch zwischen Ozean und Atmosphere. Untersucht wird der Zeitraum zwischen 1948 und 2003. Die CO_2 Flüsse werden mit einem biogeochemischem Kohlenstoff-Kreislauf Model (HAMOCC5) simuliert, das on-line an ein globales Ozean-Meereismodell (MPI-OM) gekoppelt ist. Das gekoppelte Modell wird mit täglichen, atmosphärischen Feldern aus den NCEP/NCAR Reanalysen angetrieben. Die NCEP/NCAR Reanalyse enthält eine konsistente Beschreibung der Atmosphäre seit 1948. Erstmals ist es hiermit möglich, die physikalischen und biologischen Prozesse zu analysieren, die die Variabilität des Kohlenstoff-Kreislaufs auf interannualen bis dekadischen Zeitskalen bestimmen. Die simulierte interannuale Variabilität beträgt global ± 0.50 PgC yr^{-1} ($2\,\sigma$). Sie wird zum überwiegenden Teil von physikalischen Prozessen im äquatorialen Pazifik bestimmt. Zusätzlich zu der interannualen Variabilität unterliegt das Klima im Pazifik multidekadischen Verschiebungen, mit Auswirkungen auf die Temperatur und die Winde. Aufgrund einer solchen Verschiebung um 1975, ändert sich die interannuale Variabilität im quatorialen Pazifik von ± 0.32 PgC yr^{-1} auf ± 0.23 PgC yr^{-1}. Die Variabilität im Südlichen Ozean erklärt über 20% der globalen interannualen Variabilität. Bestimmender Faktor ist die Varianz der Dicke der oberen durchmischten Schicht in Südwinter. Obwohl im Bereich des Südlichen Ozeans mehr als ein Drittel der globalen Aufnahme anthropogenen Kohlenstoffs stattfindet, ist die Konzentration von anthropogenem CO_2 gering. Ungefähr die Hälfte des aufgenommenen anthropogenen Kohlenstoffs wird nordwärts in den Bereich der subtropischen Konvergenz transportiert. Der größte Trend in den simulierten CO_2 Flüssen wird durch die zunehmende Stärke der Winde, vorallem über der Südhalbkugel, hervorgerufen. Für den Zeitraum vom 1990 bis 1999 errechnet das Modell einen Fluss von 1.74 PgC yr^{-1} in den Ozean, der sich aus einer anthropogenen Komponente von 1.91 PgC yr^{-1} und einem Fluss in engegengesetzter Richtung von 0.17 PgC yr^{-1}, begründet in der Variabilität des physikalischen Antriebs, zusammensetzt. Extremwerte von 1.20 PgC yr^{-1} ergeben sich durch das La Niña Ereignis von 1996, sowie bis zu 2.10 PgC yr^{-1} während der starken El Niños in den Jahren 1993 und 1998. Aufgrund des steigenden CO_2 Gehalts werden vor allem die obere Schichten im Ozean saurer. Gegen Ende der Simulation hin verlangsamt sich hierdurch die weitere Aufnahme von anthropogenem CO_2. Vom Beginn der Industrialisierung bis Ende 2003 hat der Ozean eine Gesamtmenge von 124 Pg anthropogenem Kohlenstoffs aufgenommen. Beachtliche Veränderungen ergaben sich durch die Limitierung der biologischen Produktion durch Eisen. Verstärkt wurde der Transport von CO_2 von der Nord- auf die Südhalbkugel, vorwiegend durch geringeres Phytoplankton-Wachstums im Südlichen Ozean. Verändert wurde auch die vertikale Struktur der biogeochemischen Elemente in der Wassersäule, was zu einer Abnahme der interannuale Variabilität der CO_2 Flüsses führt.

1. INTRODUCTION

The Third Assessment Report (Houghton *et al.*, 2001) of the Intergovernmental Panel on Climate Change (IPCC) presents scientific evidence that human activities, mostly the emission of greenhouse gases and land-use change, are already influencing the climate on Earth. This comes more than a century after Arrhenius (1896) first concluded that continued emissions of carbon dioxide would lead to a warmer climate. Greenhouse gases, such as water vapor (H_2O), carbon dioxide (CO_2), methane (CH_4) and nitrous oxide (N_2O) absorb and emit infrared radiation and play an essential role in the Earth's energy budget. In addition, clouds, aerosols and complex atmospheric chemistry affect the radiative balances in the atmosphere and are of high importance for the global climate system. Understanding and predicting possible future changes of the climate requires an understanding of the interactions between these components of the system. The aim of this work is to add to the understanding of the mechanisms which drive the variability and the trends of air-sea CO_2 fluxes.

1.1 Global and Oceanic Carbon Cycle
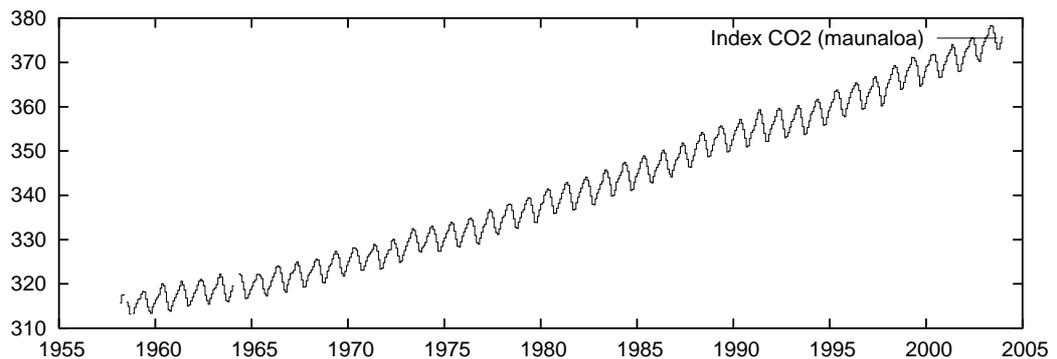
Fig. 1.1: *Concentration of CO_2 measured at Mauna Loa, Hawaii, U.S.A. at 19° 32' N, 155° 35' W, 3397 m above sea level (Keeling and Whorf, 2004).*

The most important anthropogenic greenhouse gas is carbon dioxide (CO_2). It is almost evenly distributed worldwide and has been measured in
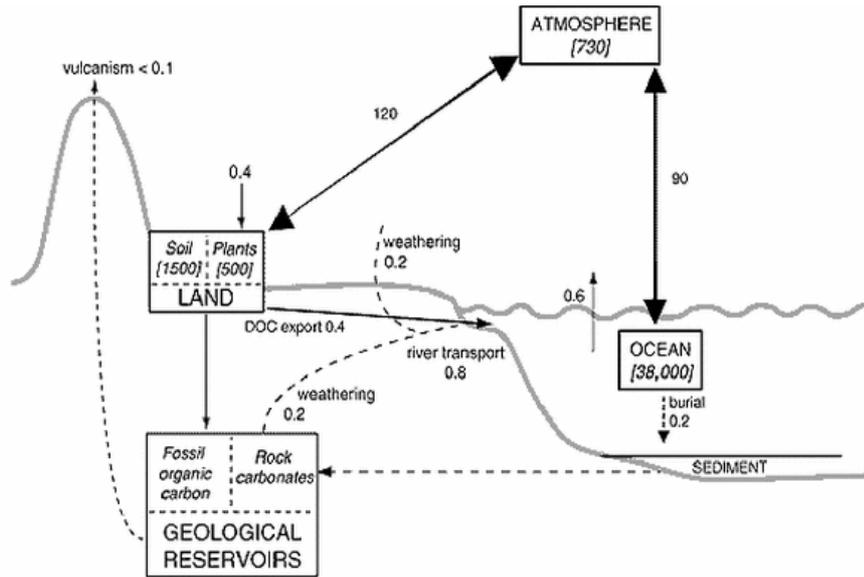
Fig. 1.2: *Simplified schematic overview of the main components of the global carbon cycle, taken from the IPCC report (Houghton et al., 2001).*

the atmosphere for more then 5 decades (Keeling and Whorf, 2004, figure 1.1). The strongest signal is the steady increase of CO_2 due to the combustion of fossil fuel, cement production, and land use change. From the beginning of industrialization in 1800 (labeled the anthropocene) until 1994 about 244±20 PgC (1Pg = 10^{15}g) were emitted (Marland *et al.*, 2004). About two-thirds of those anthropogenic emissions have accumulated in the atmosphere. The other third have been taken up by the ocean and the terrestrial biosphere. The atmospheric CO_2 concentration has increased from 281 ppm in 1800 (Enting *et al.*, 1994) to 359 ppm in 1994 (Keeling and Whorf, 2004), which is equivalent to an increase of about 165 PgC. Sabine *et al.* (2004a) calculate a global ocean anthropogenic CO_2 inventory of 118±19 PgC up until 1994. Subtracting the atmospheric change and the ocean inventory from the total emissions constrains the net carbon flux out of the terrestrial biosphere to be 39±19 PgC. Over the past two decades of the 1980s and the 1990s the emissions from fossil fuel combustion and cement production were 117±5 PgC, which is almost half of the total anthropogenic emissions (Sabine *et al.*, 2004b). Of these, about 65±1 PgC have accumulated in the atmosphere and about 37±8 PgC have been taken up by ocean. In the 1980s and the 1990s the uptake of CO_2 by the terrestrial biosphere was higher than the level of emissions from land use change, resulting in a net carbon uptake of about 15±9 PgC by the terrestrial biosphere.

The reason for the high accumulation of CO_2 in the ocean is that CO_2 is taken up by the ocean much more effectively than other gases (e.g., O_2 and

N_2). First, the solubility of CO_2 in sea water is about 56 time higher (at 24°C) than the solubility of N_2 (Broecker and Peng, 1982). Second, due to the carbon chemistry only about 1% of the total dissolved inorganic carbon (DIC) in sea water is in the form of non-ionic dissolved CO_2, the rest is dissociated into bicarbonate ions (HCO_3^-, about 91%), and carbonate ions (CO_3^{2-}, about 8%). Overall, the total amount of carbon in the ocean is about 50 times greater than the amount of carbon in the atmosphere. The total exchange time depends on the turnover timescale of the ocean and is of the order of several hundred years (Broecker and Peng, 1982).
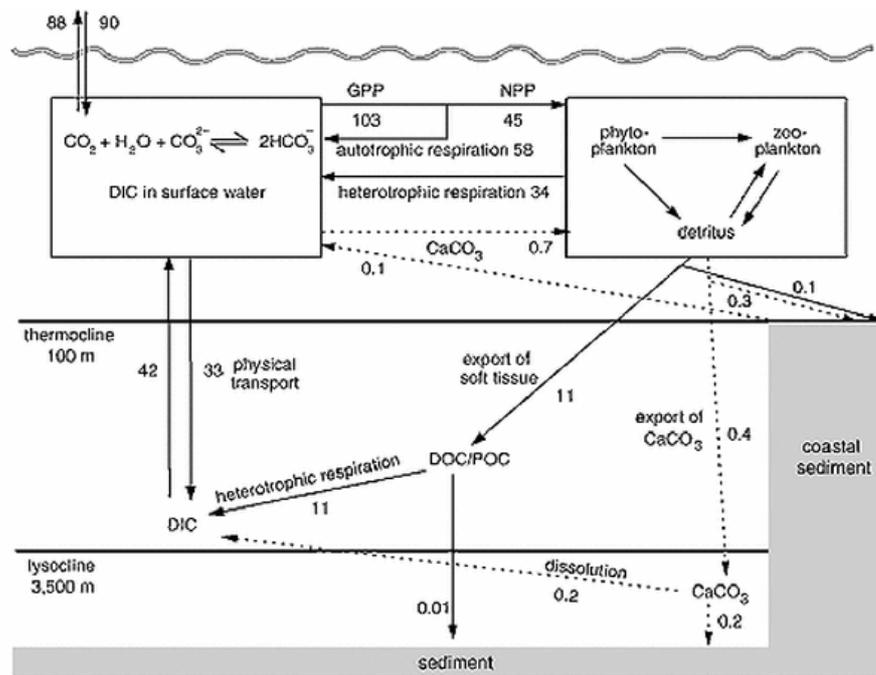

Fig. 1.3: *Simplified schematic overview of the main components of the ocean carbon cycle, taken from the IPCC report (Houghton et al., 2001).*

In addition, a vertical gradient in the oceanic DIC concentrations is generated by the so-called solubility and biological pumps. The solubility pump results from the higher solubility of CO_2 in colder water. When cold water sinks it takes the CO_2 with it into the deep ocean. It is estimated that the atmospheric CO_2 partial pressure would be up to 260 ppm higher without the solubility pump (Volk and Hoffert, 1985). The biological pump results from the export of organic material from the ocean's surface. The production of $CaCO_3$ is referred to as the biological counter pump. A schematic overview of the ocean carbon cycle is given in figure 1.3. The total amount of organic carbon produced by photosynthesis (gross primary production) in the euphotic zone (the upper layers of the ocean where light is available) is estimated to be of the order of 100 PgC yr^{-1} (Bender *et al.*, 1994). Export

of carbon out of the euphotic zone is in the form of particulate organic carbon (POC), composed of dead organisms and detritus, as well as downward oceanic transport of dissolved organic carbon (DOC). Estimates for global export production are much lower than for the gross primary production and are of the order of 11 PgC yr^{-1} (Schlitzer, 2000). Only a small fraction (about 0.1 PgC) of the export production is buried in sediments (Gattuso *et al.*, 1998). The rest is remineralized back into DIC and nutrients by bacteria in deeper layers of the ocean. In the absence of marine biology the preindustrial atmospheric CO_2 concentration could have been up to 2.4 times as high (Maier-Reimer *et al.*, 1996). Remineralized DIC and nutrients are eventually transported back to the surface by ocean advection and mixing. The balance of these two mechanisms causes the vertical gradient in the DIC concentration. Some photosynthetic organisms form calcium carbonate ($CaCO_3$) shells. The flux of $CaCO_3$ to the deep ocean is much smaller than total export production (Sarmiento *et al.*, 2002, 0.6 PgC yr^{-1}) but is an important process for the marine carbon cycle, as it influences the alkalinity of sea water, which has an effect on the CO_2 partial pressure.

1.2   Trends and Variability in the Air-Sea CO_2 Flux

The atmospheric CO_2 pool is part of the global carbon cycle (figure 1.2). The amount of carbon exchanged annually between ocean and atmosphere is about 15 times larger than the anthropogenic input and more than 10% of the atmospheric CO_2 content (figure 1.3). Carbon exchange between land and atmosphere is even larger. Any perturbation of this balance, natural or human induced, can easily have an effect of the same size as the current greenhouse gas emissions. To understand how the oceanic carbon cycle and the sea-air CO_2 fluxes change with a changing global environment one has to analyze and understand the physical, chemical and biological processes that determine them.

Predictions of future CO_2 fluxes require models that couple the climate system and the carbon cycle. But confidence in predictions can only be gained if the models realistically simulate currently observed processes, including interannual to decadal variability. In addition to being of scientific interest, the Kyoto Protocol and related future international negotiations will require credible carbon budgets for different continental and ocean regions. The budgets are computed from observed CO_2 concentrations using 3-D inverse atmospheric transport models (Gurney, 2004), but the estimates are very sensitive to their *a priori* assumptions of the oceanic CO_2 flux. Often used are the CO_2 flux estimates derived from the pCO_2 climatology by Takahashi *et al.* (2002), and time dependent CO_2 fluxes have never been considered as a first guess estimate for the atmospheric inversions. Reduc-
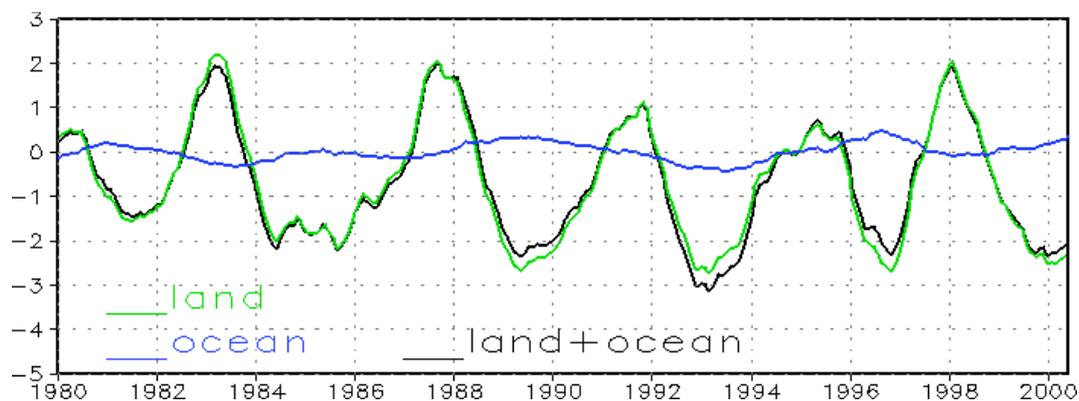
Fig. 1.4: *Simulated land-air and sea-air monthly CO_2 fluxes in PgC yr^{-1} from Zeng et al. (2004), smoothed with a 12 month running mean. The land-air fluxes are from a simulation with the terrestrial carbon cycle model VEGAS and the sea-air fluxes are results from this thesis.*

ing the uncertainties in CO_2 fluxes over the ocean will directly improve our ability to constrain the CO_2 fluxes over the continents.

This work is part of the EU project "Northern Ocean Carbon Exchange Study"(NOCES). An important aspect of the project is to constrain the air-sea CO_2 fluxes, particularly over the northern hemisphere. CO_2 fluxes produced in this work are used as *a priori* estimates in an inverse model approach to determine the northern hemisphere terrestrial sinks.

Until quite recently state-of-the-art ocean modeling has mostly been of the climatological mean state with evaluations in terms of seasonal variability (Sarmiento *et al.*, 2000) or anthropogenic perturbations (Orr *et al.*, 2001). An exception is the study by Winguth *et al.* (1994), who simulated the CO_2 fluxes related to the El Niño-Southern Oscillation. Reanalysis products from the European Center for Medium-Range Weather Forecasts (Gibson *et al.*, 1997, ECMWF) and from the National Centers for Environmental Prediction/ National Center for Atmospheric Research (Kalnay, 1996, NCEP/NCAR) are now available, which makes it feasible to simulate the interannual-to-decadal variability of the last 50 years. Ocean model simulations forced with the reanalysis products (Le Quéré *et al.*, 2000; Obata and Kitamura, 2003; McKinley *et al.*, 2004) find an interannual sea-to-air CO_2 flux variability of at most ± 0.5 PgC yr^{-1} (2σ, flux variability is given as two time the standard deviation σ throughout this thesis). Studies combining atmospheric CO_2, $\delta^{13}C$ and O_2 data indicate however, all with inevitable uncertainties, a sea-to-air flux variability of ± 1.0 to ± 2.5 PgC yr^{-1} (Joos *et al.*, 1999; Rayner *et al.*, 1999a; Keeling *et al.*, 1995; Francey *et al.*, 1995). Studies based on variations of the sea surface temperatures and CO_2 partial pressure (Lee *et al.*, 1998; Feely *et al.*, 1999) find a variability far below ± 0.5 PgC yr^{-1}. The atmospheric $\delta^{13}C$ signal and terrestrial studies (Zeng

et al., 2004) clearly indicate a dominant role of the terrestrial biosphere for the variability (figure 1.4). However, Keeling *et al.* (1995) suggest that a considerable sea-air gas exchange, mostly anti-correlated to the terrestrial flux, is needed to explain the atmospheric CO_2 signal. Recent atmospheric inversion estimates (Rödenbeck *et al.*, 2003) show an oceanic interannual variability that is more in line with the ocean model studies.
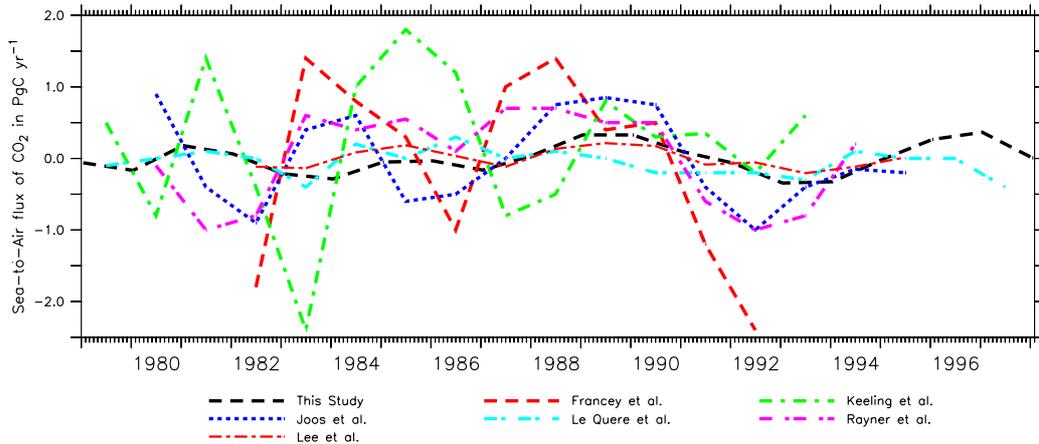
Fig. 1.5: *Comparison of atmosphere and ocean based sea-air CO_2 flux estimates.*

1.3 The Aim of this Work

In this thesis the trends and variability in the ocean-atmosphere CO_2 flux and the uptake of anthropogenic CO_2 are simulated for the period 1948 to 2003, using the biogeochemical carbon cycle model HAMOCC5 coupled on-line to the global ocean general circulation model MPI-OM. The coupled model is forced by daily NCEP/NCAR reanalysis data (Kalnay, 1996). The NCEP/NCAR reanalysis is a consistent set of atmospheric data from 1948 to 2003, which shows trends and variability on interannual and decadal timescales. This setup is used to analyze the physical and biological processes that drive the air-sea CO_2 fluxes on different time scales and in changing conditions.

Different regions of the ocean have profoundly different biochemical characteristics. Focus of this work is on the following regions:

1. **The Equatorial Pacific:**
   This has a substantial share of the interannual variability, because changes in the ocean dynamics act in phase over a large region.

2. **The Southern Ocean:**
   CO_2 fluxes there show a large trend over the full reanalysis period. It is controlled by high biological production in summer and deep mixing in winter.

3. **The North Atlantic:**
   This is a strong sink for CO_2. Locally the CO_2 flux variability is strong, but integrated over larger areas the variability averages out. Here it is important to separate the complex interplay of the different physical and biological processes.

Important questions are:

What is the relative importance of the different physical and biological processes that drive the air-sea CO_2 fluxes and the uptake of anthropogenic CO_2?

What is the relative importance of physical and biological processes in different ocean regions?

Patterns like the El Niño/Southern Oscillation, the Pacific Decadal Oscillation, the North Atlantic Oscillation and the Antarctic Oscillation show atmospheric variability on interannual to decadal timescales. Important questions are:

What processes, relevant for the marine carbon cycle, are sensitive to the atmospheric variations described by those patterns?

How do the CO_2 fluxes and the uptake of anthropogenic CO_2 react to the atmospheric variations described by those patterns?

Covering the years 1948 to 2003, the NCEP/NCAR reanalysis includes the global warming signal and various other trends, such as an increasing wind speed over the Southern Ocean. Important questions are:

What are the relevant trends in the reanalysis and how do they influence the behavior of the CO_2 fluxes and the uptake?

2. MODEL DESCRIPTION

2.1 Introduction

This work is based upon simulations with two numerical models, the ocean model MPI-OM and the carbon cycle model HAMOCC5. HAMOCC5 is coupled on-line to the ocean model MPI-OM, running with the same vertical and horizontal resolution and the same time step. A detailed technical description of HAMOCC5 will be available in the MPI-MET report series. A complete description of the ocean and sea ice components is given in Marsland *et al.* (2003) and Haak (2004).

2.2 The Ocean Model MPI-OM

The Hamburg Ocean Primitive Equation model is a z-coordinate global general circulation model based on primitive equations for a Boussinesq-fluid on a rotating sphere. Transport is computed with a second order total variation diminishing (TVD) scheme Sweby (1984). It includes parameterizations of sub grid-scale mixing processes like isopycnal diffusion of the thermohaline fields and eddy-induced tracer transport following Gent *et al.* (1995) and a bottom boundary layer slope convection scheme. The model contains a free surface and a state of the art sea ice model with viscous-plastic rheology and snow following Hibler (1979).

The model works on an orthogonal curvilinear C-grid with a formal resolution of 3°. In this setup, one pole is located over Greenland and the other over Antarctica. The horizontal resolution gradually varies between 20 km in the Arctic and about 350 km in the Tropics. It has 40 vertical levels with level thickness increasing with depth. Eight layers are within the upper 90 m and 20 are within the upper 600m. The time step is 2.4 hours. The models bathymetry was created by interpolation of the ETOPO-5 dataset (Data Announcement 88-MGG-02, Digital relief of the Surface of the Earth. NOAA, National Geophysical Data Center, Boulder, Colorado, 1988) to the model grid.

For details on MPI-OM and the grid versions, see Marsland *et al.* (2003).
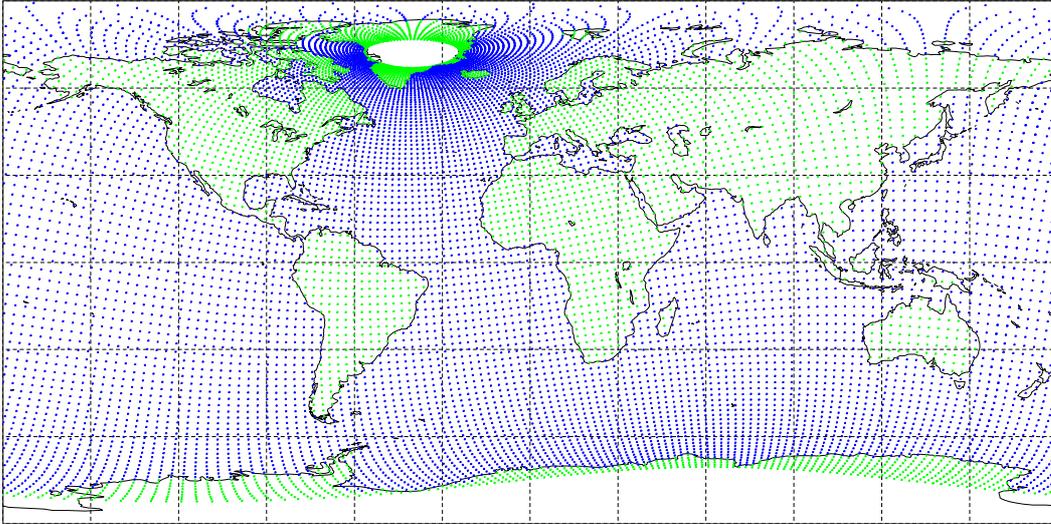
Fig. 2.1: *Curvilinear orthogonal grid of the coarse resolution global version of MPI-OM used in this work.*

2.3   The Marine Biogeochemistry Model HAMOCC5

The Hamburg Oceanic Carbon Cycle Model (HAMOCC5) simulates the marine biology and the biogeochemical tracers in the oceanic water column and the sediment. HAMOCC5 is coupled on-line to the circulation and diffusion of the MPI-OM ocean model; running with the same vertical and horizontal resolution and time step. Biochemical tracers are transported and mixed with the ocean advection and mixing schemes. However, the standard and not the isopycnal diffusion is applied to biochemical tracers, because they have larger gradients then the thermohaline fields and do not benefit from the numerically expensive isopycnal scheme. The carbon chemistry is identical to the HAMOCC3 version of Maier-Reimer (1993). The ecosystem model is based on nutrients, phytoplankton, zooplankton and detritus (NPZD-type) as described by Six and Maier-Reimer (1996). In addition new elements such as nitrogen, opal, calcium carbonate, dissolved iron and dust are accounted for, and new processes like denitrification and N-fixation, formation of calcium carbonate and opaline shells, DMS production, dissolved iron uptake and release by biogenic particles, and dust deposition and sinking are implemented. The dust fields for the experiments in this thesis are taken from an model simulation by Timmreck and Schulz (2004). The model contains a sediment module following the rules of Heinze *et al.* (2003).

2.3.1 Euphotic Zone and Upper Layer Biogeochemistry
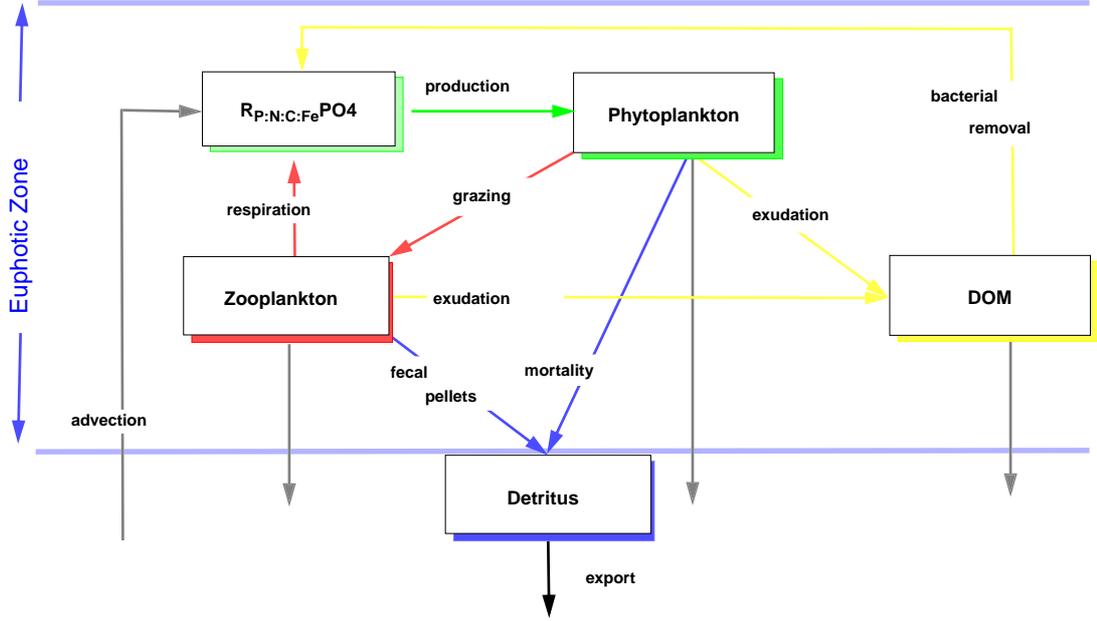
Fig. 2.2: *Simplified schematic overview of the marine ecosystem as simulated by the Hamburg Oceanic Carbon Cycle Model (HAMOCC5). The model is based on nutrients, phytoplankton, zooplankton and detritus (NPZD-type). Computation of photosynthesis and zooplankton grazing is restricted to the upper 100m of the water column (euphotic zone).*

Biological processes are regulated by light that decays towards depth. In the model, photosynthesis and zooplankton grazing is restricted to the upper 100m of the water column (euphotic zone) and all processes in the euphotic zone are considered to be aerobic. Below the euphotic zone, all organic matter ultimately remineralizes and denitrification occurs when oxygen saturation is low. The non-remineralized fraction of particulate matter falls onto the sediment. A schematic overview of the marine ecosystem as simulated by HAMOCC5 is given in figure 2.2. The following subsections address the different processes with respect to their depths, and to the components that are involved.

Phytoplankton Phytoplankton (PHY) growth depends on light (I) and nutrients. Light is attenuated by water (k_w) and chlorophyll (k_c), using a constant conversion factor for C:Chl, according to the equation:

$$I(z,t) = I(0,t)\, e^{-(k_w + k_c * Chl)z} \tag{2.1}$$

Photosynthesis is linear with light (α_{PHY}) and limited by the available nutrients. Light-saturated growth is not taken into account. It is assumed that phytoplankton take up nutrients in constant proportions of P:N:C:Fe of $1:R_{N:P}:R_{C:P}:R_{Fe:P}$ ($1:16:122:6.1*10^{-4}$).

$$photosynthesis \;\; = \;\; \frac{\text{PHY}\,\alpha_{\text{PHY}}*I(z,t)\,X}{K_{\text{PHY},\text{PO}_4}+X} \tag{2.2}$$
$$\text{with} \quad X = \min\left(\text{PO}_4\,,\frac{\text{NO}_3}{R_{N:P}},\frac{\text{FE}}{R_{Fe:P}}\right)$$

Phytoplankton exudate dissolved organic matter (DOM) with a constant rate of $\lambda_{\text{PHY},\text{DOM}}$ and die with a constant rate of $\lambda_{\text{PHY},\text{DET}}^{surf}$, but not below a minimum phytoplankton concentration of $2\,\text{PHY}_0$. Dead phytoplankton form detritus. The time derivative for phytoplankton is

$$\frac{\Delta\text{PHY}}{\Delta t} \;\; = \;\; photosynthesis - grazing \tag{2.3}$$
$$- \left(\lambda_{\text{PHY},\text{DET}}^{surf} + \lambda_{\text{PHY},\text{DOM}}\right)(\text{PHY} - 2\,\text{PHY}_0)$$

Zooplankton Phytoplankton is grazed by zooplankton (ZOO). The grazing rate follows a Michaelis-Menten function, reduced by the minimum phytoplankton concentration PHY_0:

$$grazing = \text{ZOO}\,\mu_{\text{ZOO}}\,\frac{\text{PHY}-\text{PHY}_0}{K_{\text{ZOO}}+\text{PHY}} \tag{2.4}$$

Photosynthesis and grazing are treated semi-implicitly. This avoids negative concentrations independently of the prescribed half-saturation constants of the Michaelis-Menten relation. Only a fraction of zooplankton (ZOO) grazing (ϵ_{ZOO}) is ingested by zooplankton (equation 2.5), the rest is immediately egested as fecal pellets. Of the fraction ingested, only $\omega_{graz,\text{ZOO}}$ is used for zooplankton growth; the remainder is excreted as nutrients (grazing related metabolism). Zooplankton have a basal metabolism, given by a constant rate $\lambda_{\text{ZOO},\text{DOM}}$, and die with a constant rate $\lambda_{\text{ZOO}}^{surf}$, but not below a minimum zooplankton concentration of $2\,\text{ZOO}_0$. A fraction ($\omega_{mort,\text{PO}_4}$) of the dead zooplankton immediately remineralizes, the other fraction forms detritus.

$$\frac{\Delta\text{ZOO}}{\Delta t} \;\; = \;\; grazing\,\epsilon_{\text{ZOO}}\,\omega_{graz,\text{ZOO}} \tag{2.5}$$
$$- \left(\lambda_{\text{ZOO},\text{DOM}} + \lambda_{\text{ZOO}}^{surf}\right)(\text{ZOO} - 2\,\text{ZOO}_0)$$

Detritus Detritus (DET) is formed by dead phyto- and zooplankton, and fecal pellets and sinks with a constant velocity.

$$
\begin{aligned}
\frac{\Delta \mathrm{DET}}{\Delta t} \;=\; & \lambda_{\mathrm{PHY,DET}}^{surf}\left(\mathrm{PHY} - 2\,\mathrm{PHY}_0\right) + grazing\left(1 - \epsilon_{\mathrm{ZOO}}\right) \quad (2.6) \\
& + \lambda_{\mathrm{ZOO}}^{surf}\left(\mathrm{ZOO} - 2\,\mathrm{ZOO}_0\right)\left(1 - \omega_{mort,\mathrm{PO_4}}\right)
\end{aligned}
$$

Dissolved organic matter Dissolved organic matter (DOM) is formed from phytoplankton exudation and zooplankton excretion. It remineralizes at a constant rate $\lambda_{\mathrm{DOM,PO_4}}^{surf}$.

$$
\begin{aligned}
\frac{\Delta \mathrm{DOM}}{\Delta t} \;=\; & \lambda_{\mathrm{PHY,DOM}}\left(\mathrm{PHY} - 2\,\mathrm{PHY}_0\right) \quad\quad\quad\quad\quad\quad (2.7) \\
& + \lambda_{\mathrm{ZOO,DOM}}\left(\mathrm{ZOO} - 2\,\mathrm{ZOO}_0\right) - \lambda_{\mathrm{DOM,PO_4}}^{surf}\,\mathrm{DOM}
\end{aligned}
$$

Biological production based on remineralized DOC is called "Regenerated Production", whereas biological production based on nutrients transported into the euphotic zone from below is referred to as "New Production".

Phosphate Phosphate ($\mathrm{PO_4}$) is depleted from photosynthesis and replenished by zooplankton excretion and DOM remineralization.

$$
\begin{aligned}
\frac{\Delta \mathrm{PO_4}}{\Delta t} \;=\; & -phosy + grazing\,\epsilon_{\mathrm{ZOO}}\left(1 - \omega_{graz,\mathrm{ZOO}}\right) \quad\quad\quad (2.8) \\
& + \lambda_{\mathrm{ZOO}}^{surf}\left(\mathrm{ZOO} - 2\,\mathrm{ZOO}_0\right)\omega_{mort,\mathrm{PO_4}} + \lambda_{\mathrm{DOM,PO_4}}^{surf}\,\mathrm{DOM}
\end{aligned}
$$

Nitrate For all processes except the sea-air N_2 flux and nitrogen-fixation, nitrate ($\mathrm{NO_3}$) and phosphate ($\mathrm{PO_4}$) are coupled by a constant stoichiometric ratio $R_{N:P}$.

$$
\frac{\Delta \mathrm{NO_3}}{\Delta t} \;=\; \frac{\Delta \mathrm{PO_4}}{\Delta t}\,R_{N:P} \quad\quad\quad\quad (2.9)
$$

N-fixation There is no explicit consideration of blue-green algae (diazotrophs). Instead, if there is more phosphate in the surface layer than nitrate, according to the stoichiometric ratio, N-fixation is parameterized as

$$
\frac{\Delta \mathrm{NO_3}}{\Delta t} = \mu_{NFix}\,\max\left(0, \mathrm{PO_4}\,R_{N:P} - \mathrm{NO_3}\right) \quad\quad (2.10)
$$

Oxygen Photosynthesis releases oxygen; respiration uses it. The changes in oxygen are opposite to the changes in phosphate, multiplied by the stoichiometric ratio $R_{O2:P}$.

$$\frac{\Delta O_2}{\Delta t} \;=\; -\frac{\Delta PO_4}{\Delta t}\, R_{O2:P} \tag{2.11}$$

Dissolved iron Dissolved (biologically available) iron (FE) is deposited by dust on the surface. Iron is taken up by marine organisms with a fixed ratio to phosphate ($R_{Fe:P}$), iron scavenging is parameterized in analogy to Johnson *et al.* (1997). This approach assumes that dissolved iron beyond the limit of 0.6 nmol L^{-1} (FE_0) is complexed by strong iron binding ligands with a time constant λ_{FE}. This iron is lost to the biogeochemical cycle.

$$\frac{\Delta FE}{\Delta t} = -\frac{\Delta PO_4}{\Delta t}\, R_{Fe:P} - \lambda_{FE} \; \max\left(0, FE - FE_0\right) \tag{2.12}$$

The dust fields in the experiments for this work are taken from a state of the art model simulation with ECHAM4 by Timmreck and Schulz (2004).

Silicic acid and opal Diatoms utilize silicic acid ($SI(OH)_4$) to form opal (OPAL) frustules, whereas coccolithophorids build skeletons made of calcium carbonate ($CACO_3$). Living phytoplankton do not sink or dissolve in the model. The model accounts for three phytoplankton groups, diatoms, coccolithophorids, and flagellates. It does not explicitly model the groups, but once phytoplankton cells have died, the shell material is divided into calcium carbonate and opal as a function of the detritus production. The formation of opal (Δsil) is parameterized as:

$$\Delta sil \;=\; \min\left(\frac{\Delta DET}{\Delta t}\, R_{Si:P}\, \frac{SI(OH)_4}{K_{PHY}^{SI(OH)_4} + SI(OH)_4},\, 0.5\, SI(OH)_4\right) \tag{2.13}$$

$R_{Si:P}$ denotes the Si:P ratio required by diatoms, $K_{PHY}\,SI(OH)_4$ the half-saturation constant for silicate uptake. Opal (OPAL) production by diatoms reduces silicate ($SI(OH)_4$). Opal itself degrades with constant ratio, $\lambda_{OPAL,SI(OH)_4}$. Thus,

$$\frac{\Delta SI(OH)_4}{\Delta t} \;=\; -\Delta sil + \lambda_{OPAL,SI(OH)_4}\; OPAL \tag{2.14}$$

$$\frac{\Delta OPAL}{\Delta t} \;=\; +\Delta sil - \lambda_{OPAL,SI(OH)_4}\; OPAL \tag{2.15}$$

Dissolved inorganic carbon, calcium carbonate production and alkalinity Diatoms grow faster than coccolithophorids. This implies that the fraction of calcium carbonate shell material depends on the availability of silicate. The formation of calcium carbonate (Δcar) is parameterized as:

$$\Delta car \quad = \quad R_{Ca:P} \frac{\Delta\text{DET}}{\Delta t} \frac{K_{\text{PHY}}^{\text{SI(OH)}_4}}{K_{\text{PHY}}^{\text{SI(OH)}_4} + \text{SI(OH)}_4} \tag{2.16}$$

In the surface layer DIC and phosphate are coupled by a constant stoichiometric ratio $R_{C:P}$. In addition, the formation of calcium carbonate (CACO_3) shells during phytoplankton growth reduces the dissolved inorganic carbon (DIC) concentration and decreases the alkalinity. The concomitant changes in nitrate concentration also change the alkalinity.

$$\frac{\Delta\text{DIC}}{\Delta t} \quad = \quad \frac{\Delta\text{PO}_4}{\Delta t} R_{C:P} - \Delta car \tag{2.17}$$

$$\frac{\Delta\text{A}_T}{\Delta t} \quad = \quad \frac{\Delta\text{PO}_4}{\Delta t} R_{N:P} - 2\,\Delta car \tag{2.18}$$

DMS The DMS production in the model depends on the growth of diatoms and coccolithophorids, modified by temperature, T, its decrease depends on temperature and irradiance I. This is regulated via 5 parameters, $D_1 - D_5$, and only takes place in the euphotic zone, i.e., in the upper few layers of the water column.

$$\frac{\Delta\text{DMS}}{\Delta t} \quad = \quad (D_5\,delsil + D_4\,\Delta car)\left(1 + \frac{1}{(T+D_1)^2}\right) \tag{2.19}$$
$$- (D_2\,8\,I + D_3\,|T+3|)\,\text{DMS}$$

2.3.2 Deep Ocean Biogeochemistry

Deep aerobic remineralization Below the euphotic zone phytoplankton and zooplankton die with constant rates $\lambda_{\text{PHY,DET}}^{deep}$ and $\lambda_{\text{ZOO,DET}}^{deep}$. If the oxygen concentration is sufficient, detritus and DOM are remineralized with constant rates $\lambda_{\text{DET,PO}_4}^{deep}$ and $\lambda_{\text{DOM,PO}_4}^{deep}$ to phosphate.

$$remin_{\text{DET}}^{aerob} \quad = \quad \min\left(\lambda_{\text{DET,PO}_4}^{deep}\,\text{DET}, \frac{0.5\,\text{O}_2}{R_{-O2:P}\,\Delta t}\right)$$

$$remin_{\text{DOM}}^{aerob} \quad = \quad \min\left(\lambda_{\text{DOM},\text{PO}_4}^{deep}\text{DOM}\,,\frac{0.5\,\text{O}_2}{R_{-O2:P}\,\Delta t}\right)$$

$$\frac{\Delta\text{PHY}}{\Delta t} \quad = \quad -\lambda_{\text{PHY},\text{DET}}^{deep}\max\left(0,\text{PHY}-\text{PHY}_0\right) \qquad (2.20)$$

$$\frac{\Delta\text{ZOO}}{\Delta t} \quad = \quad -\lambda_{\text{ZOO},\text{DET}}^{deep}\max\left(0,\text{ZOO}-\text{ZOO}_0\right) \qquad (2.21)$$

$$\frac{\Delta\text{DET}}{\Delta t} \quad = \quad +\lambda_{\text{PHY},\text{DET}}^{deep}\max\left(0,\text{PHY}-\text{PHY}_0\right) \qquad (2.22)$$

$$+\lambda_{\text{ZOO},\text{DET}}^{deep}\max\left(0,\text{ZOO}-\text{ZOO}_0\right)-remin_{\text{DET}}^{aerob}$$

$$\frac{\Delta\text{DOM}}{\Delta t} \quad = \quad -remin_{\text{DOM}}^{aerob} \qquad (2.23)$$

$$\frac{\Delta\text{PO}_4}{\Delta t} \quad = \quad remin_{\text{DET}}^{aerob}+remin_{\text{DOM}}^{aerob} \qquad (2.24)$$

Nitrate, DIC, alkalinity and oxygen are calculated analog to phosphate using the respective stoichiometric ratios.

$$\frac{\Delta\text{NO}_3}{\Delta t} \quad = \quad \frac{\Delta\text{PO}_4}{\Delta t}\,R_{N:P} \qquad (2.25)$$

$$\frac{\Delta\text{DIC}}{\Delta t} \quad = \quad \frac{\Delta\text{PO}_4}{\Delta t}\,R_{C:P} \qquad (2.26)$$

$$\frac{\Delta\text{A}_T}{\Delta t} \quad = \quad -\frac{\Delta\text{PO}_4}{\Delta t}\,R_{N:P} \qquad (2.27)$$

$$\frac{\Delta\text{O}_2}{\Delta t} \quad = \quad -\frac{\Delta\text{PO}_4}{\Delta t}\,R_{-O2:P} \qquad (2.28)$$

$$(2.29)$$

Depending on the oxygen saturation (S_{O2}), a fraction of N_2 is oxidized to N_2O

$$oxidize \quad = \quad 0.0001\begin{cases} 1 & : & S_{O2}-\text{O}_2 < 1.97\times10^{-4} \\ 4 & : & S_{O2}-\text{O}_2 \geq 1.97\times10^{-4} \end{cases}$$

$$\frac{\Delta\text{N}_2}{\Delta t} \quad = \quad -\left(remin_{\text{DET}}^{aerob}+remin_{\text{DOM}}^{aerob}\right)R_{-O2:P}\,oxidize \quad (2.30)$$

$$\frac{\Delta\text{N}_2\text{O}}{\Delta t} \quad = \quad \left(remin_{\text{DET}}^{aerob}+remin_{\text{DOM}}^{aerob}\right)R_{-O2:P}\,oxidize \qquad (2.31)$$

Opal goes into dissolution with a constant rate $\lambda_{\text{OPAL},\text{SI}(\text{OH})_4}$:

$$\frac{\Delta\text{OPAL}}{\Delta t} \quad = \quad -\lambda_{\text{OPAL},\text{SI}(\text{OH})_4}\text{OPAL} \qquad (2.32)$$

$$\frac{\Delta\text{SI}(\text{OH})_4}{\Delta t} \quad = \quad +\lambda_{\text{OPAL},\text{SI}(\text{OH})_4}\text{OPAL} \qquad (2.33)$$

The dissolution of calcium carbonate depends on the CO_3^{2-} undersaturation of sea-water and a dissolution rate constant $\lambda_{CACO_3,DIC}$. Undersaturation is calculated from the average of the almost uniform Ca^{2+} concentration in sea water and the CO_3^{2-} solubility product, S_{Ca}, of calcite:

$$dissol = \min\left(\frac{U_{CO3}}{\Delta t}, \lambda_{CACO_3,DIC} \, CACO_3\right) \quad \text{with} \quad (2.34)$$

$$U_{CO3} = \max\left(0, [Ca^{2+}] \, S_{Ca} - CO_3^{2-}\right) \qquad (2.35)$$

$$\frac{\Delta CACO_3}{\Delta t} = -dissol \qquad (2.36)$$

$$\frac{\Delta DIC}{\Delta t} = dissol \qquad (2.37)$$

$$\frac{\Delta A_T}{\Delta t} = 2\,dissol \qquad (2.38)$$

Deep anaerobic remineralization and denitrification In the absence of sufficient oxygen organic matter (detritus) is remineralized by denitrification. Bacteria (not modeled explicitly) take the oxygen from nitrate as final electron acceptor, and reduce the nitrate to N_2. Two moles of nitrate are utilized to oxidize three moles of organic carbon. Under aerobic conditions this would take three moles of oxygen; therefore the anaerobic remineralization ratio is $2/3\,R_{-O2:P}$. Nitrate is also produced by remineralization. The alkalinity with the same ratio $(R_{N:P})$ as the nitrate production.

$$remin_{DET}^{anaerob1} = 0.5\,\lambda_{DET,PO_4}^{deep} \min\left(DET, \frac{0.5\,NO_3}{\frac{2}{3}R_{-O2:P}\,\Delta t}\right)$$

$$\frac{\Delta DET}{\Delta t} = -remin_{DET}^{anaerob1} \qquad (2.39)$$

$$\frac{\Delta NO_3}{\Delta t} = \left(R_{N:P} - \frac{2}{3}\,R_{-O2:P}\right)remin_{DET}^{anaerob1} \qquad (2.40)$$

$$\frac{\Delta N_2}{\Delta t} = \frac{1}{3}\,R_{-O2:P}\,remin_{DET}^{anaerob1} \qquad (2.41)$$

$$\frac{\Delta PO_4}{\Delta t} = remin_{DET}^{anaerob1} \qquad (2.42)$$

$$\frac{\Delta DIC}{\Delta t} = R_{C:P}\,remin_{DET}^{anaerob1} \qquad (2.43)$$

$$\frac{\Delta A_T}{\Delta t} = -R_{N:P}\,remin_{DET}^{anaerob1} \qquad (2.44)$$

Analogous to denitrification a fraction of detritus remineralizes by N_2O reduction. Two moles of nitrate are utilized to oxidize one moles of organic carbon. Under aerobic conditions this would take one moles of oxygen; therefore the anaerobic remineralization ratio is $2\,R_{-O2:P}$.

$$
remin_{\text{DET}}^{anaerob2} \;\; = \;\; 0.01 \min \left(\text{DET}\,, \frac{0.003\,\text{N}_2\text{O}}{2\,R_{-O2:P}\,\Delta t} \right)
$$

$$
\frac{\Delta \text{DET}}{\Delta t} \;\; = \;\; -remin_{\text{DET}}^{anaerob2} \tag{2.45}
$$

$$
\frac{\Delta \text{NO}_3}{\Delta t} \;\; = \;\; R_{N:P}\,remin_{\text{DET}}^{anaerob2} \tag{2.46}
$$

$$
\frac{\Delta \text{N}_2\text{O}}{\Delta t} \;\; = \;\; -2\,R_{-O2:P}\,remin_{\text{DET}}^{anaerob2} \tag{2.47}
$$

$$
\frac{\Delta \text{N}_2}{\Delta t} \;\; = \;\; 2\,R_{-O2:P}\,remin_{\text{DET}}^{anaerob2} \tag{2.48}
$$

$$
\frac{\Delta \text{PO}_4}{\Delta t} \;\; = \;\; remin_{\text{DET}}^{anaerob2} \tag{2.49}
$$

$$
\frac{\Delta \text{DIC}}{\Delta t} \;\; = \;\; R_{C:P}\,remin_{\text{DET}}^{anaerob2} \tag{2.50}
$$

$$
\frac{\Delta \text{A}_T}{\Delta t} \;\; = \;\; -R_{N:P}\,remin_{\text{DET}}^{anaerob2} \tag{2.51}
$$

2.3.3   Marine Carbon Chemistry

The treatment of carbon chemistry is similar to the one described in Maier-Reimer and Hasselmann (1987; see also Heinze and Maier-Reimer, 1999b). CO_2 in seawater is discussed in detail in Zeebe and Wolf-Gladrow (2001).

The model explicitly simulates total dissolved inorganic carbon DIC, borate and total alkalinity A_T, defined as

$$
[DIC] \;\; = \;\; [CO_2] + \left[HCO_3^- \right] + \left[CO_3^{2-} \right] \tag{2.52}
$$

$$
[A_T] \;\; = \;\; \left[HCO_3^- \right] + 2\left[CO_3^{2-} \right] + \left[B(OH)_4^- \right] + \left[OH^- \right] - \left[H^+ \right] \tag{2.53}
$$

Aqueous carbon dioxide $CO_2(aq)$ and true carbonic acid H_2CO_3 are chemically not separable; the sum of both is denoted by CO_2. Changes in total carbon concentration and alkalinity due to biogeochemical processes have been described above. Changes due to sea-air gas exchange (see section 2.3.4) and calcium carbonate dissolution depend on surface layer pCO_2 and carbonate ion concentration, $[CO_3^{2-}]$, which are evaluated numerically from DIC and A_T in the following way:

The carbonate system is defined by the two dissociation steps from CO_2 to carbonate, CO_3^{2-}, and the borate buffer, via:

$$
H_2O + CO_2 \;\; \rightleftharpoons \;\; HCO_3^- + H^+ \tag{2.54}
$$

$$HCO_3^- \rightleftharpoons CO_3^{2-} + H^+ \qquad (2.55)$$
$$H_2O + B(OH)_3 \rightleftharpoons B(OH)_4^- + H^+ \qquad (2.56)$$
$$H_2O \rightleftharpoons (OH)^- + H^+ \qquad (2.57)$$
$$\qquad (2.58)$$
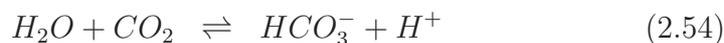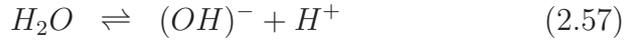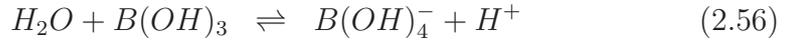
with $B_T = [B(OH)_3] + \left[B(OH)_4^-\right] \propto S$, ($S$ = salinity) computed at every timestep. The dissociation constants

$$K_1 = \frac{\left[HCO_3^-\right][H^+]}{[CO_2]} \qquad (2.59)$$

$$K_2 = \frac{\left[CO_3^{2-}\right][H^+]}{\left[HCO_3^-\right]} \qquad (2.60)$$

$$K_B = \frac{\left[B(OH)_4^-\right][H^+]}{[B(OH)_3]} \qquad (2.61)$$

$$K_W = \left[(OH)^-\right]\left[H^+\right] \qquad (2.62)$$

$$\qquad (2.63)$$

are computed from temperature and salinity (Dickson and C. Goyet, 1994).

Using the dissociation constants and equation 2.52, [CO_3^{2-}] and [HCO_3^-] are expressed as funktions of [DIC] and [H$^+$]. With the given values for [DIC[and [Alkainity], equation 2.53 is solved numerically for [H$^+$]. With [H$^+$], CO_2 and pCO_2 are calculated for the air-sea gas exchange (section 2.3.4), and CO_3^{2-} is calculated for the dissolution of calcium carbonate.

Calcium carbonate is dissolved with a maximal rate of $\lambda_{\text{CACO}_3,\text{DIC}}$, depending on the undersaturation of Ca^{2+} (equation 2.36, section 2.3.2).

2.3.4 Air-Sea Gas Exchange

The fluxes of O_2, N_2, N_2O, DMS and CO_2 across the sea-air interface equal the gas transfer velocity (K) multiplied by the solubility (S) and the the partial pressure difference between air and water of the respective tracer x.

$$Fx = Kx * Sx * (pPx_{water} - pPx_{air}) \qquad (2.64)$$

Solubilities of CO_2, O_2, N_2 and N_2O are calculated from temperature and salinity according to Weiss (1970). CO_2 concentrations are computed from total dissolved organic carbon (DIC), as described in section 2.3.3.

The gas transfer velocity (Kw) is computed with the following equation adapted from Wanninkhof (1992) (eq. 3),

$$Kw = (1 - F_{ice}) \frac{u^2}{(Sc/660) ** 1/2} * 0.337 \qquad (2.65)$$

where F_{ice} is the partial sea-ice cover, u is the wind speed and Sc is the Schmidt number. The Schmidt numbers for CO_2, O_2 and DMS are computed analogous to Wanninkhof (1992), Keeling *et al.* (1998) and Saltzmann (1993) respectively; Schmidt numbers for N_2 and N_2O are identical to the Schmidt number for O_2.

2.3.5 The sediment

The sediment module basically follows Heinze *et al.* (2003). It is resolved into 12 vertical layers, with increasing thickness and decreasing porosity (pore water content). From the top, it is fed by particle rain of detritus, opal and calcium carbonate, and the pore water is in diffusive exchange with the water column above. It is assumed, that the porosity of the sediment remains constant over time. Changes in porosity from accumulation or degradation of particulate matter are compensated by sediment shifting, thus simulating bioturbation. Inside the sediment, the aerobic and anaerobic decomposition of detritus, and the dissolution of opal and calcium carbonate is considered. Below the biologically active 12 layers, there is additionally a diagenetic consolidated layer, containing all the particulate tracers that have been shifted downward.

Sediment biogeochemistry

Decomposition of particulate matter (particulate organic matter, opal and calcium carbonate) is computed simultaneously with the input of particles from the water column, and the diffusive exchange of pore water with the lowest layer of the water column (phosphate, nitrate, alkalinity, oxygen, silicate and dissolved inorganic carbon). The fraction of solid sediment is denoted by ϕ, the fraction of pore water is $1 - \phi$. Input from particle rain at the top is given by Q^*, the term for diffusive exchange of pore water with the water column by D^*. D^* and Q^* are zero for all layers but the top layer. For details see Heinze *et al.* (2003).

Silicate and opal   The dissolution rate of opal depends on the undersaturation of silicate in pore water, $U_{\text{SI(OH)}_4} = Sat_{\text{SI(OH)}_4} - \text{SI(OH)}_4$, times a constant $\kappa_{\text{OPAL,SI(OH)}_4}$.

$$\frac{\Delta\text{OPAL}}{\Delta t} = -\kappa^{sedi}_{\text{OPAL},\text{SI(OH)}_4}\, U_{\text{SI(OH)}_4}\,\text{OPAL} + Q^*_{\text{OPAL}} \quad (2.66)$$

$$\frac{\Delta U_{\text{SI(OH)}_4}}{\Delta t} = D^* - \kappa^{sedi}_{\text{OPAL},\text{SI(OH)}_4}\, U_{\text{SI(OH)}_4}\,\text{OPAL}\, \frac{\phi}{1-\phi} \quad (2.67)$$

The system is solved for the new undersaturation $U^{t+\Delta t}_{\text{SI(OH)}_4}$, from with the new silicate and opal concentrations are computed.

Detritus decomposition/Aerobic conditions   If oxygen is available, detritus (DET_s) degrades with a constant rate $\kappa^{sedi}_{\text{DET},\text{PO}_4}$ to phosphate. The degradation depends on the available oxygen.

$$\frac{\Delta\text{DET}}{\Delta t} = -\kappa^{sedi}_{\text{DET},\text{PO}_4}\, O_2\,\text{DET} + Q^*_{\text{DET}} \quad (2.68)$$

$$\frac{\Delta O_2}{\Delta t} = D^* - \kappa^{sedi}_{\text{DET},\text{PO}_4}\, O_2\,\text{DET}\, R_{O2:P}\, \frac{\phi}{1-\phi} \quad (2.69)$$

The system is solved for the new oxygen concentration, from with the new detritus and pore water phosphate concentrations are computed. The changes of nitrate, dissolved inorganic carbon and alkalinity in the pore water are computed via the stoichiometric ratios.

Anaerobic conditions/denitrification   In the absence of sufficient oxygen detritus is remineralized by denitrification. The process is modeled analogous to the denitrification in the water column (section 2.3.2.

$$\frac{\Delta\text{DET}}{\Delta t} = \lambda_{\text{DET},\text{PO}_4}\, \min\left(\text{DET}, \frac{0.5\,\text{NO}_3}{\frac{2}{3}R_{-O2:P}\,\Delta t}\right) \quad (2.70)$$

$$\frac{\Delta\text{PO}_4}{\Delta t} = \frac{\Delta\text{DET}}{\Delta t}\, \frac{\phi}{1-\phi} \quad (2.71)$$

$$\frac{\Delta\text{NO}_3}{\Delta t} = \left(R_{N:P} - \frac{2}{3}R_{-O2:P}\right)\frac{\Delta\text{DET}}{\Delta t} \quad (2.72)$$

$$\frac{\Delta\text{N}_2}{\Delta t} = \frac{1}{3}R_{-O2:P}\,\frac{\Delta\text{DET}}{\Delta t} \quad (2.73)$$

$$\frac{\Delta\text{DIC}}{\Delta t} = +R_{C:P}\,\frac{\Delta\text{DET}}{\Delta t} \quad (2.74)$$

$$\frac{\Delta\text{A}_T}{\Delta t} = -R_{N:P}\,\frac{\Delta\text{DET}}{\Delta t} \quad (2.75)$$

Calcium carbonate dissolution and inorganic carbon cycle Dissolution of calcium carbonate in the sediment is modeled analogous to the water column. First, the carbonate ion concentration, $[CO_3^{2-}]$, is computed. Second, the apparent solubility product of calcite, S_{Ca}, and the total $[Ca^{2+}]$ concentration are used to calculate the undersaturation of the pore water carbonate, $U_{CO3} = \max\left(0, \frac{S_{Ca}}{[Ca^{2+}]} - [CO_3^{2-}]\right)$, using a constant dissolution rate $\kappa_{CACO_3,DIC}^{sedi}$.

$$\frac{\Delta CACO_3}{\Delta t} = -\kappa_{CACO_3,PO_4}^{sedi}\, U_{CO3}\, CACO_3 + Q_{CACO_3}^* \qquad (2.76)$$

$$\frac{\Delta U_{CO3}}{\Delta t} = D^* - \kappa_{CACO_3,PO_4}^{sedi}\, U_{CO3}\, CACO_3\, \frac{\phi}{1-\phi} \qquad (2.77)$$

The system is solved for the new undersaturation, $U_{CO3}^{t+\Delta t}$ and the new calcium carbonate and pore water DIC and alkalinity concentrations are computed.

Sediment upward and downward advection

Bioturbation, the way in which burrowing organisms move the sediment downwards and upwards, is modeled depending on the concentration of solid matter. It is assumed, that the porosity and the volume of the sediment remain constant over time. If the actual volume of the solid constituents of a layer (i.e. the weight of its solids constituents divided by their density) exceeds the volume prescribed, solid sediment will be successively shifted downwards. If the actual volume of the solid constituents of a layer is too low to fill the prescribed volume, solid sediment will be successively shifted upwards. The last layer empties its excess solid matter into a final diagenetic consolidated layer. In case of upward shifting, material from the buried layer goes back to the sediment. If there are no biogenic components available in the buried layer, an infinite supply of clay is assumed.

3. EXPERIMENT DESCRIPTION

3.1   Introduction

Chapter 2 introduces the numerical models, the ocean model MPI-OM and the carbon cycle model HAMOCC5. This section deals with the atmospheric forcing, the spinup of the models, the sensitivity to the initial conditions and the setup of the experiments.

3.2   NCEP/NCAR Atmospheric Forcing

The model is forced with daily heat, freshwater and momentum fluxes from the NCEP/NCAR reanalysis (Kalnay, 1996), interpolated onto the model grid. The daily 2 m air and dew point temperatures, precipitation, cloud cover, 10 m wind speed and surface wind stress are taken without modification. Dew point temperature T_{Dew} is derived from specific humidity q and air pressure p according to Oberhuber (1988). On global average NCEP/NCAR downward short wave radiation is appr. 10% higher than reanalysis data from the European Center for Medium-Range Weather Forecasts (Gibson *et al.*, 1997, ECMWF) and 20% higher than estimates from the Earth Radiation Budget experiment (Trenberth and Solomon, 1994, ERBE). To correct for this systematic offset in the NCEP/NCAR downward short wave radiation a global scaling factor of 0.89 is applied. The sensible, latent, and long wave heat flux at the air/sea interface is computed by bulk formulae of the ocean model. This work uses the same formulae as described in Haak (2004).

3.2.1   Detrended forcing

The NCEP/NCAR reanalysis includes trends such as the global warming signal. Particularly the Southern Ocean shows a trend in the wind fields over the full forcing period (Figure 3.1). This inevitably leads to a different mean state at the beginning of the forcing period, compared to the end of the forcing period. When the forcing is repeated consecutively, there is an initial "shock" each time the system has to start over. Such a "shock" causes

an initial artificial variability and a trend back to the new mean state of the system. To get a best estimate of the initial conditions, consistent with the beginning of the NCEP/NCAR reanalysis period, we have computed a detrended set of the NCEP/NCAR fields from 1948 to 2001 with respect to the first years of the reanalysis. This is done by putting a linear regression through each forcing parameter on each point, and subtract the trend in each point of the grid separately. As an example, figure 3.1 shows the average 10 m windspeed for the Southern Ocean from detrended and the original NCEP/NCAR forcing and the CO_2 flux, simulated with the respective forcing sets.
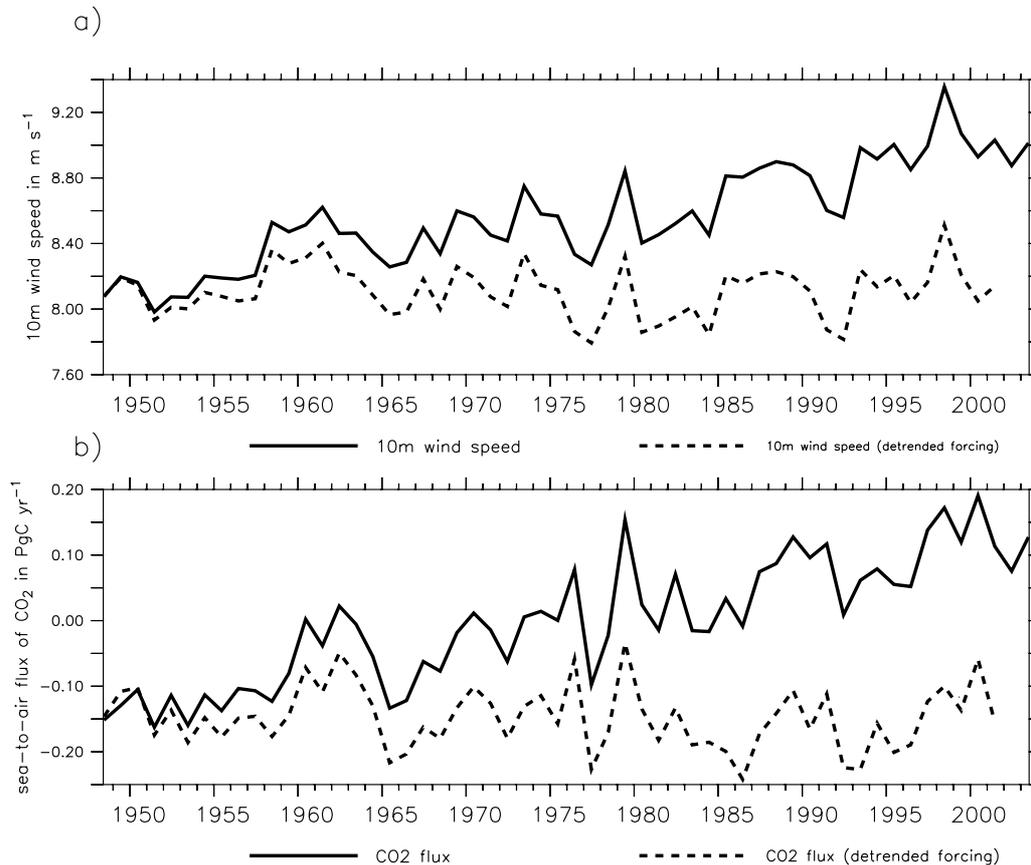

Fig. 3.1: *Comparison of the NCEP/NCAR forcing to the detrended forcing set for the Southern Ocean from 40° S to 60° S. Shown in a) the annual average 10 m wind speed and in b) the simulated CO_2 flux.*

3.3   Initialization, Spinup and Run Description

3.3.1   Initialization and Spinup

The ocean model is initialized with annual mean temperature and salinity data from Levitus *et al.* (1998) climatology and the ocean velocities at rest. It is integrated for one year using daily NCEP/NCAR data for 1948 forcing and a global three dimensional restoring of temperature and salinity to the Levitus climatology. The subsurface restoring is applied everywhere below 40 m with a time constant chosen to be 1 month during this first year. This procedure brings the models velocities and sea ice distribution to near equilibrium with the Levitus climatology. After this initialization procedure the subsurface restoring is switched off. The surface salinity relaxation within the upper model level (0-12 m) is released to a time constant of 180 days. The biogeochemical model is started with an uniform tracer distribution. Biogeochemical tracers are not restored to data, to be fully consistent with the biological, chemical and physical dynamics of the model.

After initialization the model is integrated for 1700 years (spinup run), periodically repeating the forcing with the detrended fields, while the inventory of alkalinity is adjusted to match a preindustrial CO_2 level of 278 ppm. Fluxes and tracer distribution stabilized after about 1000 model years. This model version did not have an iron limitation. After the iron limitation was implemented in the model, the model is again integrated for another 1000 years, starting from the distribution after the 1700 years of the initial spinup. The main experiment (Experiment ID: ANT55) is initialized with the system state at the end of the last spinup run, after 2700 model years of integration. It is discussed in detail in section 3.3.2. All results presented in this thesis, if not stated otherwise, refer to this experiment

As a sensitivity study on the influence of iron-limitation on the CO_2 flux variability, an experiment without iron-limitation is started from the system state at the end of the last year of the spinup without iron limitation (Experiment ID: NoIron34). All other parameters are identical and the experiment follows the exact same protocol as the main experiment (Experiment ID: ANT55). Results from this experiment are discussed in detail in chapter 7.

3.3.2   Experiment Description

After the spinup, the system is in a preindustrial state, cyclo-stationary over the the detrended forcing period. From this preindustrial state the main experiment (Experiment ID: ANT55) is started. It consists of a run with rising
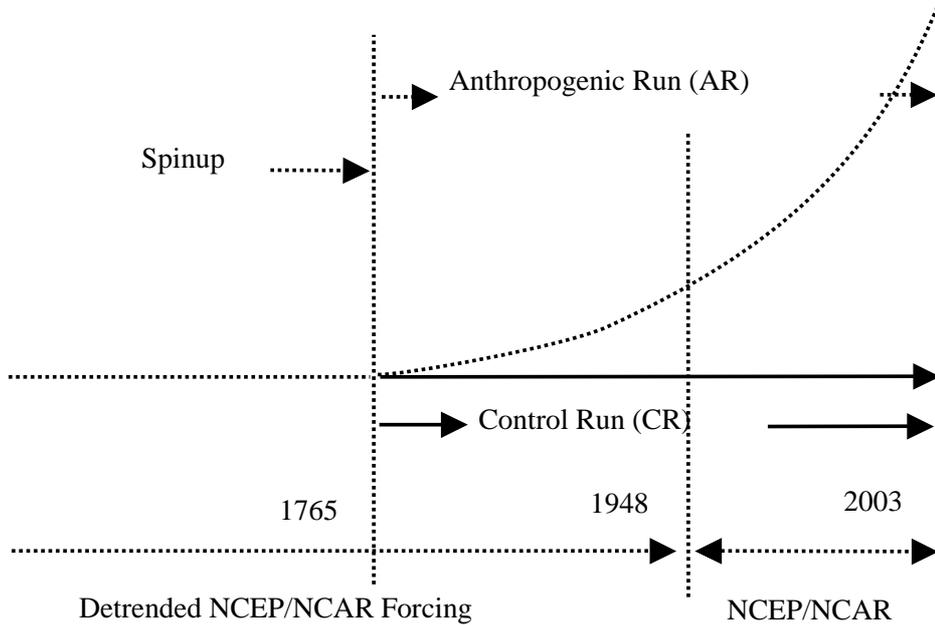
Fig. 3.2: *Schematic setup of the control run (CR) and the anthropogenic run (AR).*

atmospheric CO_2 levels for the years 1765 to 2003 and an otherwise identical control run with atmospheric CO_2 kept at a preindustrial level of 278 ppm. For the years 1765 to 1947 both experiments are forced with the detrended fields and, from the year 1948 on, with the original NCEP/NCAR fields with their inherent trends. Hereafter on we will refer to the two experiments as the AR (anthropogenic run) and the CR (control run). To extract the oceanic uptake variability from fluctuations caused by varying atmospheric CO_2 concentrations, a smoothed, strictly monotonic increasing atmospheric CO_2 concentration is used. It is taken from a spline fit to ice core and Mauna Loa CO_2 data (Enting *et al.*, 1994, www.ipsl.jussieu.fr/OCMIP/).

Interpretation of variability in this work is focused on the years 1948 to 2003, which are computed with the non-detrended NCEP/NCAR reanalysis forcing fields.

3.3.3   Sensitivity to Initial Conditions

Simulation experiments are determined by the initial and the boundary conditions. While in our case the surface boundary conditions are taken from the NCEP/NCAR reanalysis, there exists almost no knowledge about the ocean and biogeochemical initial conditions. To constrain the uncertainty,
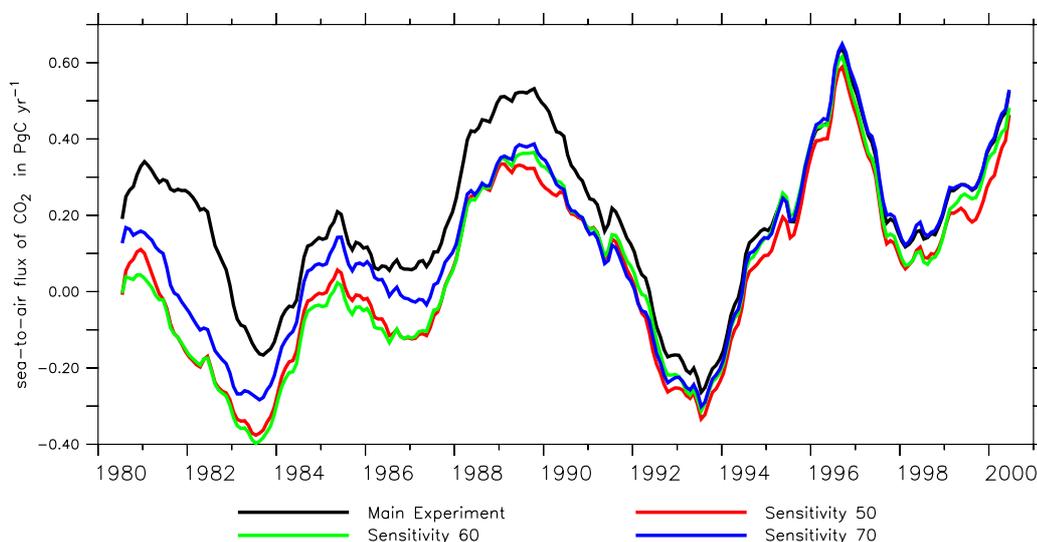
Fig. 3.3: *Sensitivity tests started from initial conditions from the beginning of year 1950, 1960 and 1970 of the control run of the main experiment.*

sensitivity tests are computed with different starting conditions from different years. Upper layer ocean properties are reasonably robust after about 5 years. The CO_2 fluxes follow the forcing almost directly and the amplitude of the signal adjusts after about 15 years. The timescale corresponds to the timescale of changes in the main thermocline in the equatorial Pacific. Therefore, the first model years should not be interpreted as they are influenced by the last years of the previous (detrended) forcing period, and because the first years of the NCEP/NCAR reanalysis suffer from the sparseness of the database.

4. PHYSICAL AND BIOGEOCHEMICAL MEAN STATE

4.1 Introduction

Focus of this work is the interannual and decadal variability. But one of the most important prerequisites for a meaningful estimate of the variability in a non-linear system is the mean state. The critical question one has to ask such a numerical model is: Are its physical and biochemical mechanisms able to reproduce the observed mean state? In this section the simulated mean state of oceanic and biochemical properties are described and compared with observations.

4.2 Physical Properties

The spatial distributions of biogeochemical tracers are governed by the combination of physics, chemistry and biology. Deficiencies in the ocean dynamics lead to errors in the simulated CO_2 fluxes and the predicted uptake of anthropogenic CO_2 (Doney *et al.*, 2004). The physical properties are computed by the ocean general circulation model MPI-OM (see chapter 2). A more detailed description of the simulated oceanic mean state with MPI-OM is given in Haak (2004) and Marsland *et al.* (2003).

4.2.1 Mixed Layer

The oceanic Mixed Layer (ML), within which salinity, temperature, density and biochemical tracers are almost vertically uniform, is one of the most important properties of the upper ocean. As biological activity is restricted to the upper ocean within the euphotic zone, the Mixed Layer Depth (MLD) determines the amount of nutrients available to phytoplankton. But also mixing of phytoplankton is important. The shallowing of the mixed layer depth in the high latitudes in spring, due to warming of upper waters, stops

the mixing of phytoplankton out of the euphotic zone and triggers the spring bloom.
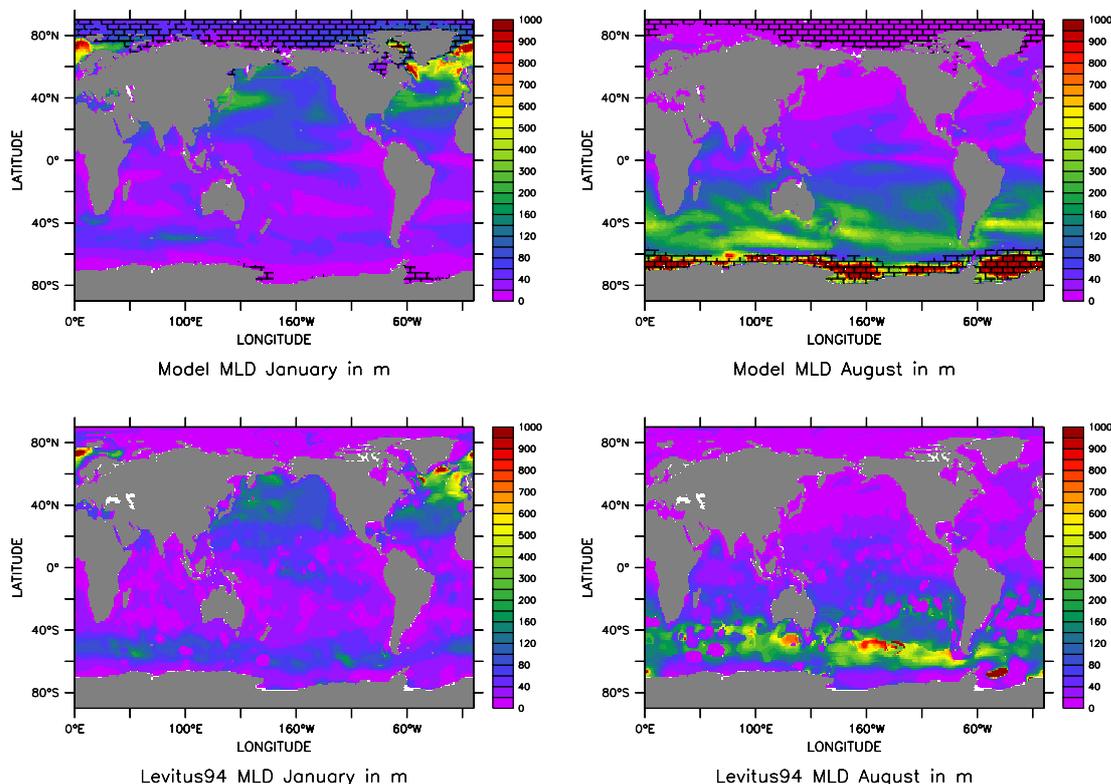
Fig. 4.1: *Upper row: Simulated Mixed Layer Depth, averaged for the period 1948-2003. The gridded areas show the simulated sea ice cover. Lower row: Mixed Layer Depth derived from the World Ocean Atlas 1994 (Monterey and Levitus, 1997).*

In the high latitude deep water formation areas the MLD can be less than 20 m in summer and up to the full water column in winter. Figure 4.1 shows the simulated MLD, averaged for the period 1948-2003, and the MLD derived from the World Ocean Atlas 1994 (Monterey and Levitus, 1997) [1]. Both, the simulated and the data derived MLD are defined by the density criteria $\sum_1^k \delta\rho_{insitu}(z) < 0.125$. For better comparison, the model results are interpolated to the 1°by 1°grid of Monterey and Levitus (1997). Seasonal and spatial pattern of the modeled MLD are generally consistent with the data compilation. The ocean model realistically simulates the two

---

[1] NODC (Levitus) World Ocean Atlas 1994 data provided by the NOAA-CIRES Climate Diagnostics Center, Boulder, Colorado, USA, from their Web site at http://www.cdc.noaa.gov/

main sinking sites in the northern North Atlantic and the deep convection in the Southern Ocean.

## 4.2.2   Distribution of CFCs
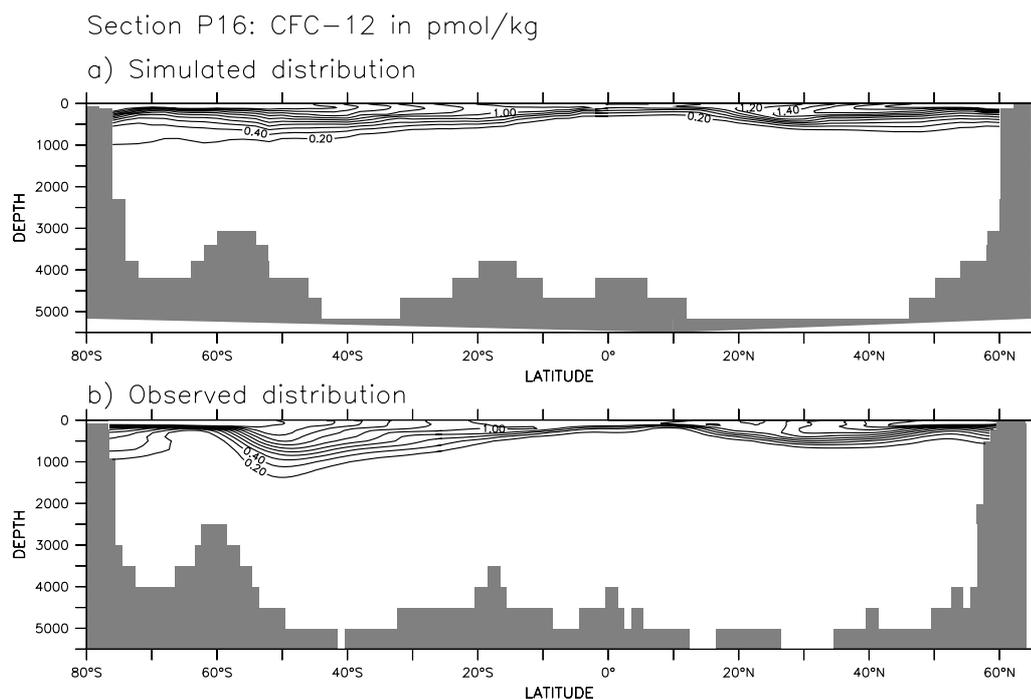
Fig. 4.2: *CFC-12 distribution (in pmol/kg) along the WOCE section P16 (150°W) in the Pacific. A) model results from the simulated year 1995; and b) observations taken from Key* et al. *(2004).*

Chlorofluorocarbons (CFCs, CFC-11 and CFC-12), are very inert gases of anthropogenic origin. They enter the surface ocean via gas exchange and are carried within the ocean as passive and conservative tracers of circulation and mixing processes. Oceanic accumulation of CFCs and anthropogenic CO_2 are different because of differences in the gas exchange, the solubility and because CFCs do not participate in the carbonate chemistry. Nevertheless, CFCs are often used as water "age"tracers, giving information about the amount of time since the parcel of water was last at the surface. This method is applied to evaluate the ability of ocean circulation models to simulate the uptake and redistribution of anthropogenic CO_2 in the oceans (Dutay *et al.*, 2002) The uptake of CFCs follows the CFCs partial pressure in the atmosphere, increasing from zero since the 1930s. It is high in regions of cold winter SST and strong vertical mixing such as the Southern
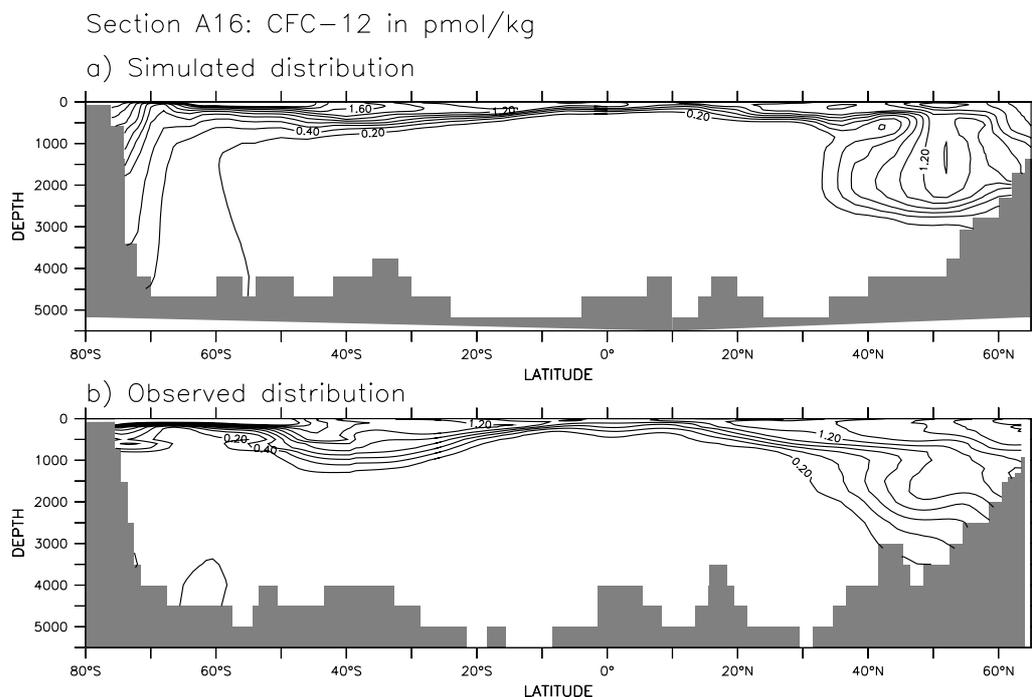
Fig. 4.3: *CFC-12 distribution (in pmol/kg) along the WOCE section A16 (25°W) in the Atlantic. A) model results from the simulated year 1995; and b) observations taken from Key et al. (2004).*

Ocean and the North Atlantic Ocean and very low in the subtropics. Despite the warm SST there is some uptake of CFCs in the Equatorial Pacific due to upwelling of subsurface waters with very low CFC concentration. Uptake is lowest in the subtropical gyres where, due to warm SSTs and low mixing with subsurface waters, CFCs equilibrate fast with the atmospheric concentration.

In figure 4.2 and 4.3, the modeled CFC-12 distribution is compared to measurements from the recent World Ocean Circulation Experiment (WOCE) for section P16 along 150°W in the Pacific and section A16 along 25°W in the Atlantic. No deep water is formed in the North Pacific so the penetration of CFCs is restricted to the thermocline, both for the model and observations. Model and observations show the deepest penetration in the subtropical gyre between 20°N and 40°N, but the penetration depth is slightly underestimated by the model. Stratification in the North Pacific subpolar gyre north of 40°N is not as pronounced in the model as in the observations. In the North Atlantic model and observations show a transport of CFCs down to over 3000 m with the formation of Lower North Atlantic Deep Water. The maximum at about 1800 m corresponds to the Upper North Atlantic Deep Water.

Differences between model and observation are largest in the Southern Ocean. Poorly captured by the model is the formation of Subantarctic Mode Water that causes the sharp subsurface tracer penetration down to approximately 1000 m depth occurring between 55°S and 40°S. Formation of Antarctic Bottom Water brings some CFCs down into the deep Southern Ocean, for both observation and simulation. In the Weddell Sea between 60°E and 20°W the model produces deep convection in coherence with the formation of sea ice which is entraining more CFCs into the deep Southern Ocean as indicated by observations.

4.2.3 Meridional Overturning

Biogeochemical tracers show a complex layered structure that is partly due to the large scale thermohaline circulation (THC). Modeled global, Pacific and Atlantic overturning stream functions show the two cell structure, associated with the THC (figure 4.4). The upper overturning cell has an average depth of about 3000 m and with a strength of 18 Sv at 24°N. It mostly represents the formation and the southward penetration of salty North Atlantic Deep Water (NADW) and compares well to the observational estimates of 17-18 Sv by Hall and Bryden (1982) and Roemmich and Wunsch (1985). Below is northward penetration at the bottom of Antarctic Bottom Water (AABW) formed around Antarctica.

Central Water (CW) is formed by subduction in the subtropical convergence (STC), which is not well captured in the model as the distribution of CFC's (section 4.2.2) demonstrates. Nevertheless, the meridional overturning stream function shows the subtropical convergence cells (STC), associated with the formation of Central Water (CW) and upwelling in the equatorial current system. This process is of high importance for the CO_2 flux variability. Variations of the equatorial upwelling in the Pacific control about 65% of the total interannual CO_2 flux variability. The South Atlantic STC strength is appr. 10 Sv in the simulation, which is in agreement with estimates by Zhang *et al.* (2003). In the Pacific the STC average strength is appr. 46 Sv and 44 Sv for the southern and the northern cell respectively. The upwelling in the equatorial strip between 9°N and 9°S is 33 Sv on average in the simulation. This simulated mean and the slowdown of the overturning circulation by about 25% since the 1970s is in agreement with observational evidence (McPhaden and Zhang, 2002).

a) Total Ocean

b) Pacific & Indian Ocean
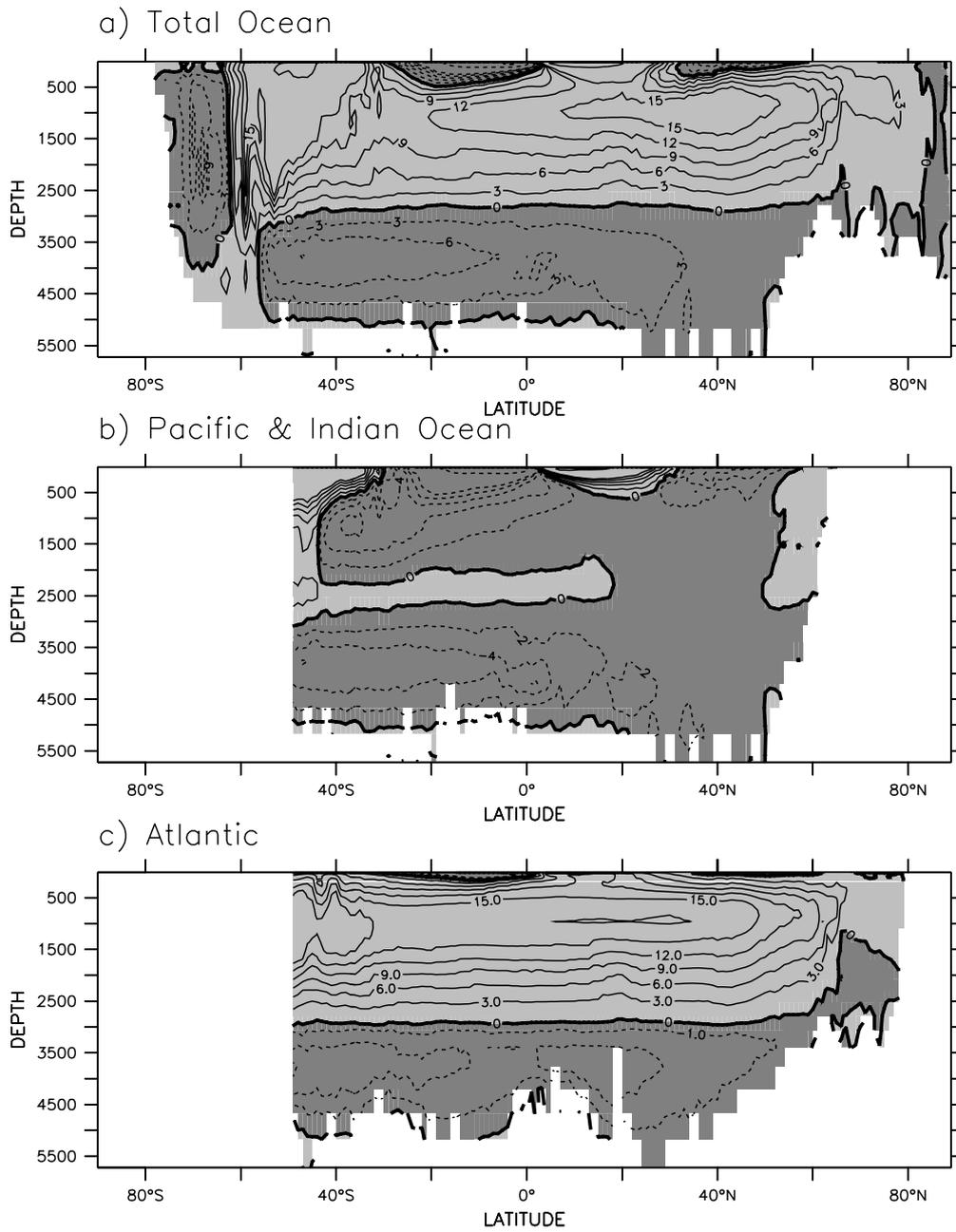
c) Atlantic

Fig. 4.4: *Meridional overturning averaged over the full 56 year NCEP/NCAR reanalysis period for the total ocean (a), the Pacific (b) and the Atlantic (c). Negative values are dark shaded; the contour interval is 4 Sv.*

4.3 Biogeochemical Properties

4.3.1 Biological Production

On average, the simulated global total production is about 24 PgC yr^{-1}. Export production out of the euphotic zone is about 5 PgC yr^{-1}, so the resulting global f-ratio (the ratio of new to primary production) is about 0.2. General estimates for the f-ratio are of the order of 0.1 to 0.2 with maximum numbers up to 0.5 (Broecker and Peng (1982), Laws *et al.* (2000)). Laws *et al.* (2000) estimate the global organic carbon export production to be 11 PgC yr^{-1}. The simulated export-ratio (the ratio of CACO$_3$ to organic carbon export) is tuned to be 0.07 on average. This ratio results in a realistic alkalinity distribution and is within the estimate of 0.06 $\pm$0.03 that Sarmiento *et al.* (2002) give.

Figure 4.5 shows a yearly averaged chlorophyll distribution from the SeaWIFS Satellite [2] and the simulated surface chlorophyll. The chlorophyll concentration of the model is determined from the modeled phytoplankton biomass multiplied by a variable, empirically derived CHL:P ratio (Cloern *et al.*, 1995), based on temperature, light and nutrient availability. The global patterns match well. High chlorophyll concentrations in costal areas cannot be reproduced by the model, because shelf processes and riverine input of nutrients are not captured. Predominantly in the Southern Ocean and the subtropical gyres modeled concentrations are generally larger than the satellite estimates. A possible explanation for this is the dynamic of the ocean model. The CFC distribution (section 4.2.2) indicates that the mixing in the Southern Ocean may be too strong in the model, while the downwelling in the subtropical gyres may be to weak. The simulated living marine biomass of phytoplankton and zooplankton is 0.5 Pg Carbon and 0.3 Pg Carbon on average.

4.3.2 Biochemical Tracer Distribution

Most important for the interannual variability and the trends in the simulated CO$_2$ flux are the changes in ocean circulation and mixing, acting on biogeochemical tracers such as DIC. The general distribution of the biogeochemical tracers is governed by physical (transport and mixing by the ocean), chemical and biological processes. Therefore it is not only ocean physics that is important for the interannual variability, but also the marine biology has a significant influence by shaping the distribution of the biogeochemical tracers. For a meaningful estimate of variability and trends,

---

[2] Data are provided by the SeaWiFS Project (Code 970.2) and the Distributed Active Archive Center (Code 902) at the Goddard Space Flight Center, Greenbelt, MD 20771. These activities are sponsored by NASA's Mission to Planet Earth Program.
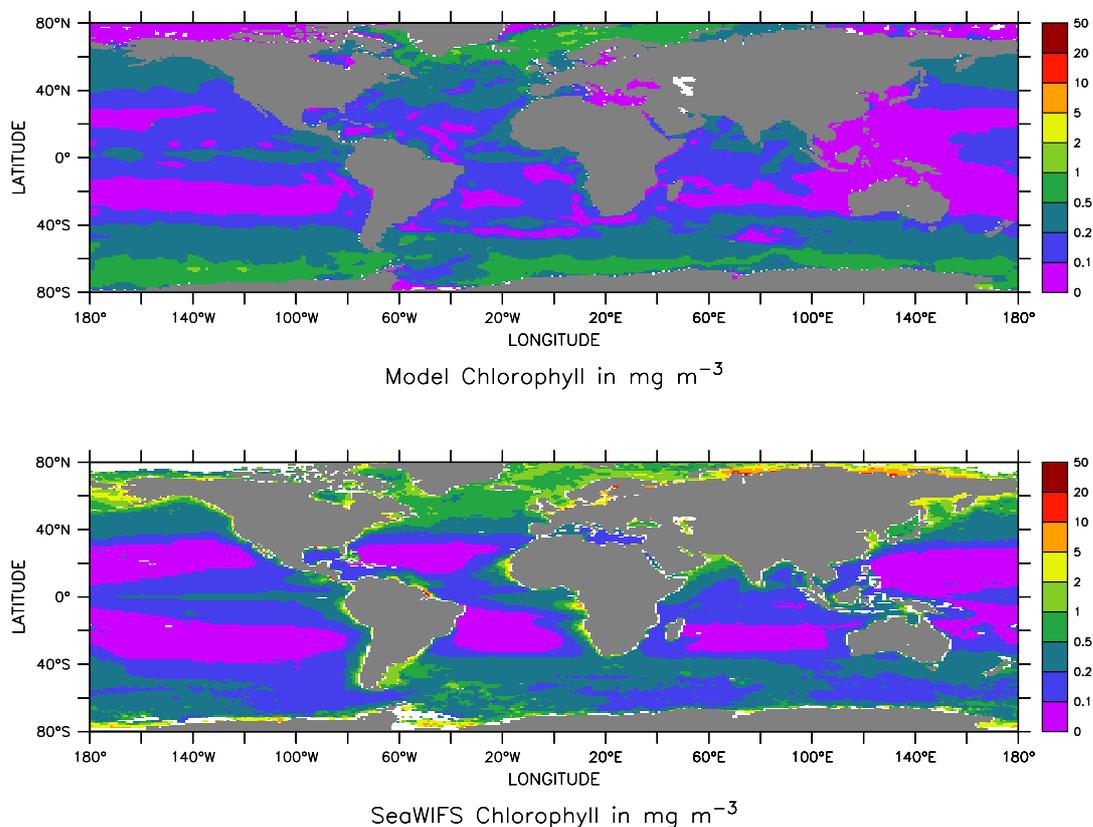
Fig. 4.5: *Yearly averages of chlorophyll distribution from the SeaWIFS Satellite and simulated surface chlorophyll.*

ocean dynamics and biological production have to be realistic and have to be consistent with each other.

The resulting distribution of biogeochemical tracers can be compared to observations. In figures 4.8 to 4.11, the simulated distributions of phosphate, oxygen, dissolved organic carbon (DIC) and total alkalinity are compared to surface distribution maps and along the WOCE sections P16 at 150°W in the Pacific and A16 at about 25°W in the Atlantic. Phosphate and oxygen data are taken from the World Ocean Atlas 1998 [3] (Conkright *et al.*, 1998). DIC and alkalinity date are provided by the GLODAP project [4] (Key *et al.*, 2004). In general the patterns of the biochemical tracers are consistent with the observations.

---

[3] World Ocean Atlas 1998 data provided by IRI/LDEO Climate Data Library from their Web site at http://iridl.ldeo.columbia.edu/SOURCES/.NOAA/.NODC/.WOA98

[4] GLobal Ocean Data Analysis Project data are taken from their Web site at http://cdiac.ornl.gov/oceans/glodap
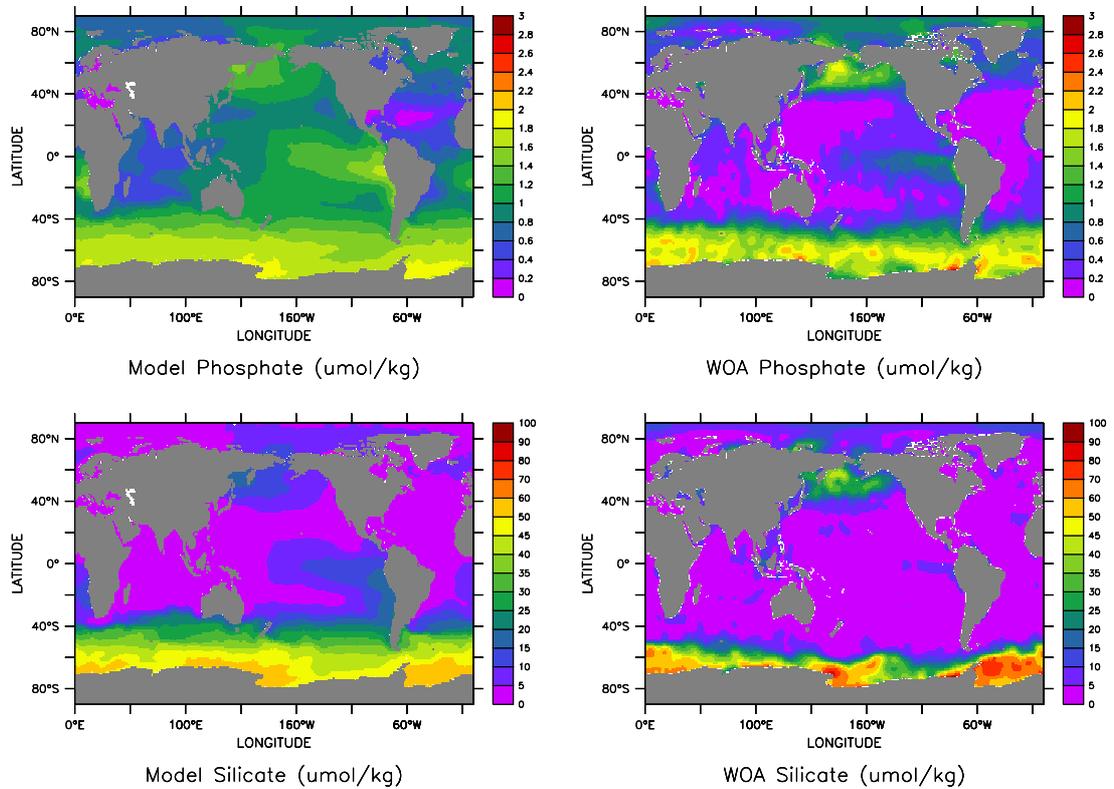
Fig. 4.6: *Phosphate and silicate surface distributions (in micromol/kg) from the simulated year 1995 and data compilations taken from the WOA 1998 (Conkright* et al., *1998).*

Nutrient distribution In equatorial regions the wind driven upwelling causes a constant flux of nutrients to the surface (figure 4.6). The Southern Ocean and the high northern latitudes of the Atlantic have a deep MLD in winter and nutrients are mixed to the surface. In the subtropical gyres Ekman pumping is primarily downward and the mixed layer depth (MLD) is low, so very few nutrients are mixed to the surface; therefore nutrient concentrations are low. Biological production (figure 4.5) and surface nutrient concentration (figure 4.6) in the subtropical gyres are overestimated by the model. Along the sections through the Pacific and the Atlantic (figure 4.8) the vertical distribution of nutrients in the upper 1000 m is also higher in the model than in the observations. This model behavior is consistent with the properties of the meridional stream function (section 4.2.3) and the distribution of CFCs (section 4.2.2). The subtropical convergence cells in the model reach down to down to 500 m while observations show a depth of more than 1000 m. Surface nutrient concentration are lower in the Atlantic because dust input from the Saharan desert supplies a lot of iron to
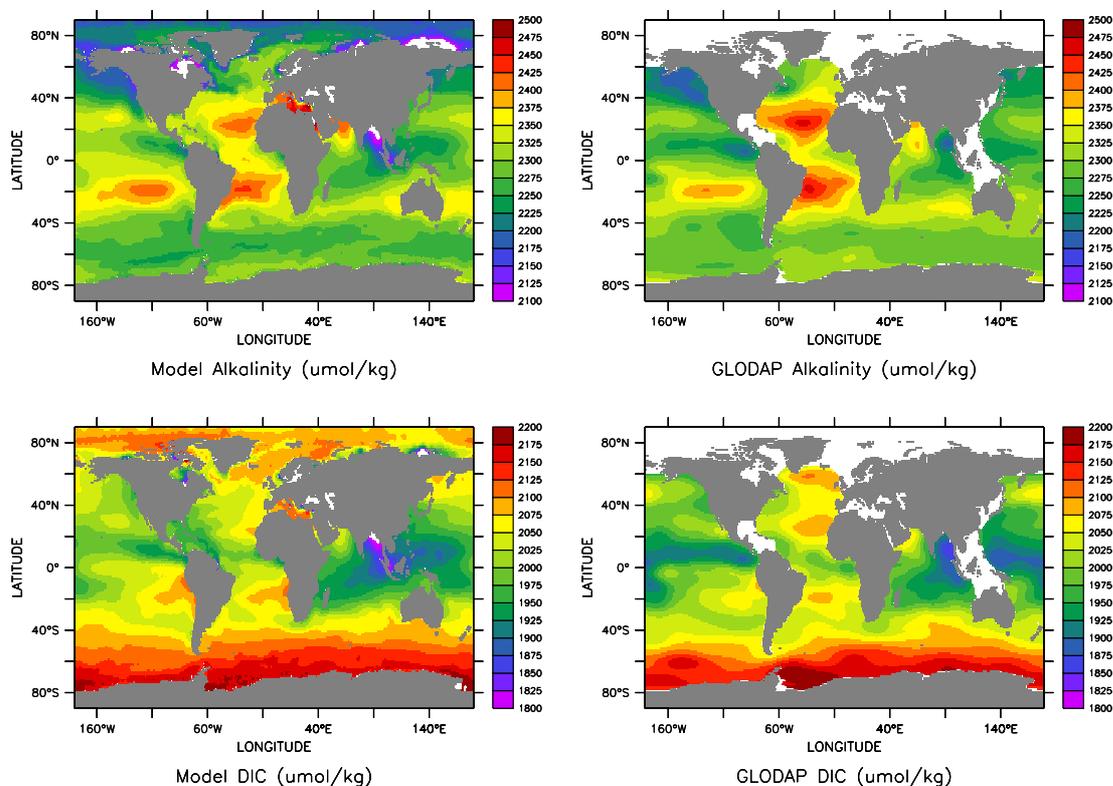
Fig. 4.7: *Alkalinity and Dissolved Inorganic Carbon surface distributions (in micromol/kg) from the simulated year 1995 and data compilations taken from the GLobal Ocean Data Analysis Project (Key et al., 2004).*

the surface waters and thus the biological pump is stronger (high export of nutrients out of the euphotic zone). Biological production in the Pacific and the Southern Ocean is iron limited in the model and there is observational evidence that in the real ocean this is the case in the equatorial and subarctic Pacific and the Southern Ocean (Fung *et al.*, 2000). In other words, in the model the Ekman pumping in the subtropical gyres is too low leaving too many nutrients at the surface that can not be taken up, because the biological production is iron limited. Without the iron limitation the simulated nutrient concentration in the subtropical gyres is closer to observations, but at the cost of much larger than observed biological production.

Deep ocean concentrations of nutrients are usually higher than surface concentrations, while deep ocean oxygen concentrations are usually lower than surface concentrations. Phosphate concentrations in the newly formed deep water in the North Atlantic are low, and the water is rich in oxygen. As the water masses travel with the "conveyor belt" southward to the Southern

Ocean and then onto the Pacific the nutrient concentration rises and oxygen is consumed. The reason is the remineralization of organic matter exported from the surface by organisms within the water column. Deep winter mixing in the Southern Ocean brings nutrients to the surface and also the newly formed Antarctic Bottom Water has higher oxygen concentrations. Very important is the upwelling of nutrient rich deep water in the equatorial Pacific and Atlantic. The high biological production and the subsequent high export of organic material and its remineralization causes a nutrient maximum and an oxygen minimum underneath the equatorial regions ("nutrient trapping"). In the deep Equatorial Pacific, oxygen concentrations are low and denitrification, remineralization by nitrate reduction instead of oxygen consumption, is an important process.

Iron limitation affects the biological production and export from the surface and therewith changes the biogeochemical tracer distribution in the water column below. Changes in the subsurface DIC and alkalinity distributions have a considerable impact on the simulated interannual CO_2 flux variability. The effects of iron limitation are discussed in detail in section 7.1.

DIC and Total Alkalinity The surface distribution of dissolved inorganic carbon (DIC) and Total Alkalinity (TA) is mostly controlled by the factors that control salinity. Normalized to salinity the distribution would look similar to the distribution of phosphate. In the deep ocean the DIC and TA distribution is governed by the biological pump and ocean transport (as discussed for phosphate above). But one has to keep in mind that in addition to phosphate DIC and TA are affected by the formation and dissolution of mineral calcium carbonate and that DIC is also subject to the CO_2 air-sea gas exchange and therefore on the surface also depends on the water temperature.

Section P16: Phosphate in micromol/kg

a) Simulated distribution

b) Observed distribution

Section A16: Phosphate in micromol/kg

a) Simulated distribution


b) Observed distribution
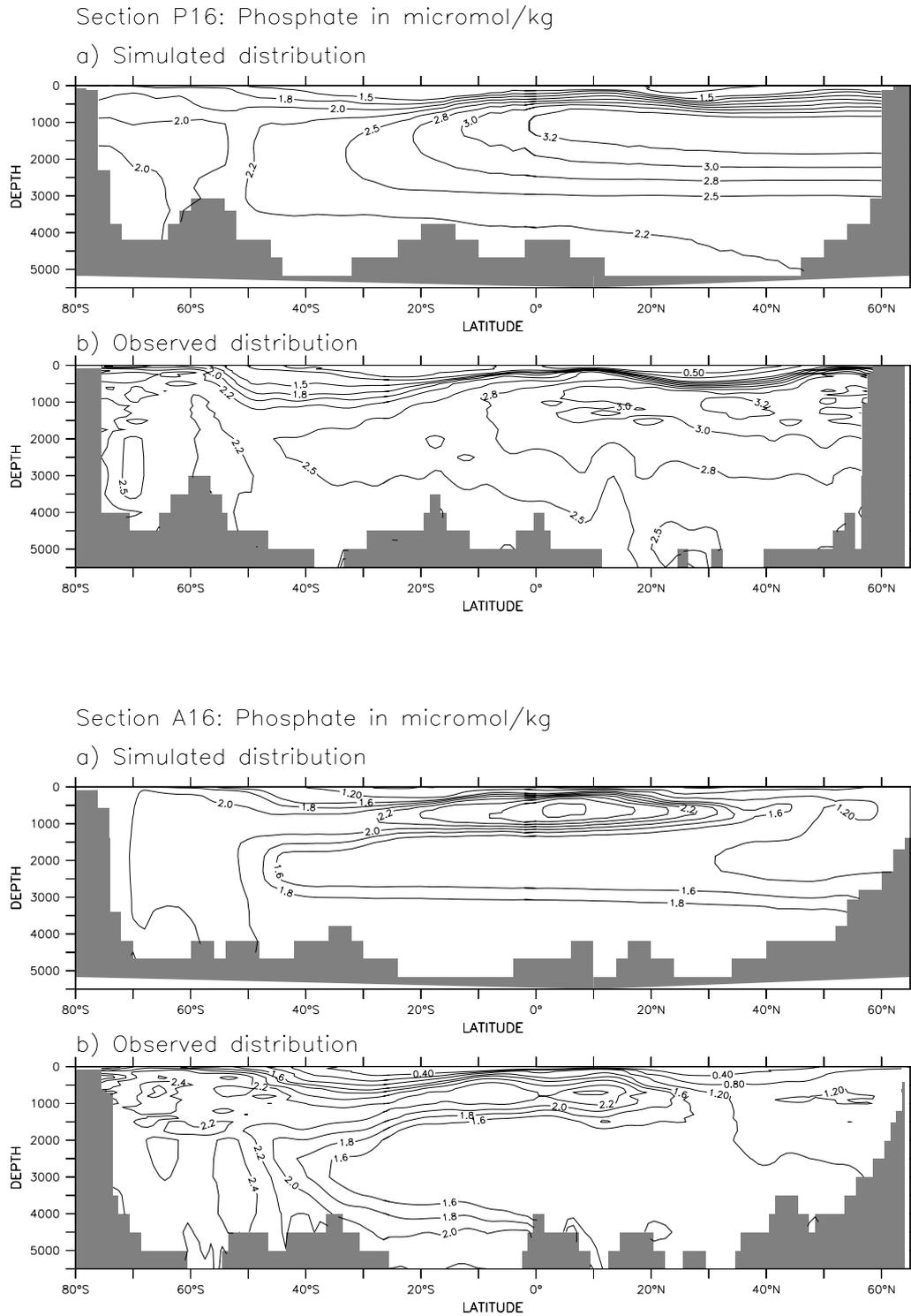
Fig. 4.8: *Phosphate distribution (in micromol/kg) along the WOCE sections P16 (150° W) in the Pacific and A16 (25° W) in the Atlantic. A) model results from the simulated year 1995; and b) observations taken from Conkright* et al. *(1998).*

Section P16: Oxygen in micromol/kg

a) Simulated distribution
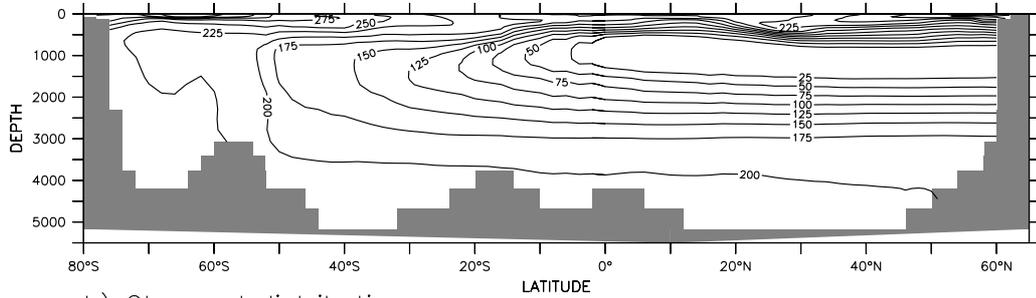
b) Observed distribution
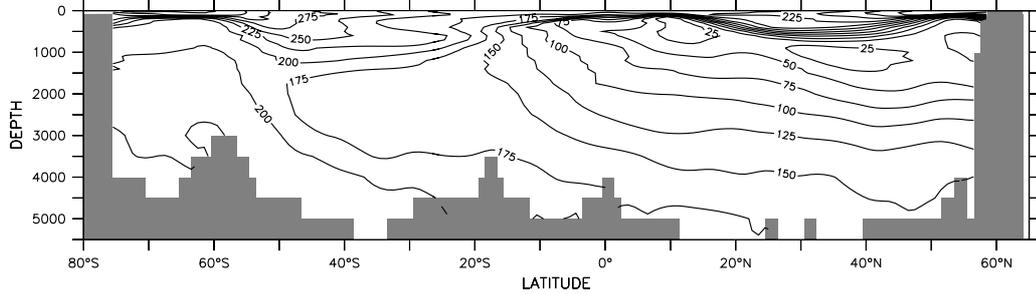
Section A16: Oxygen in micromol/kg

a) Simulated distribution
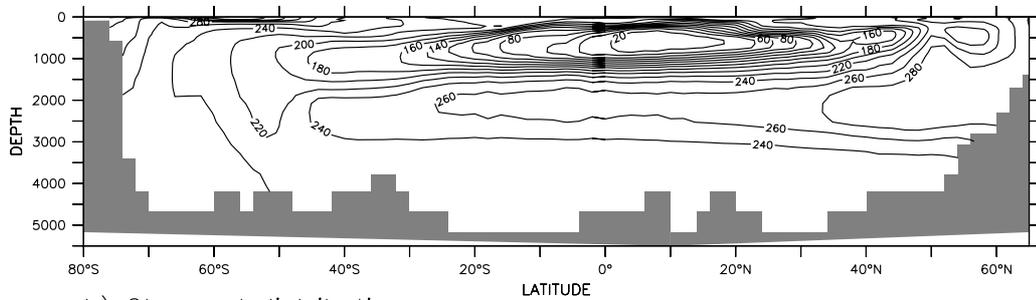
b) Observed distribution
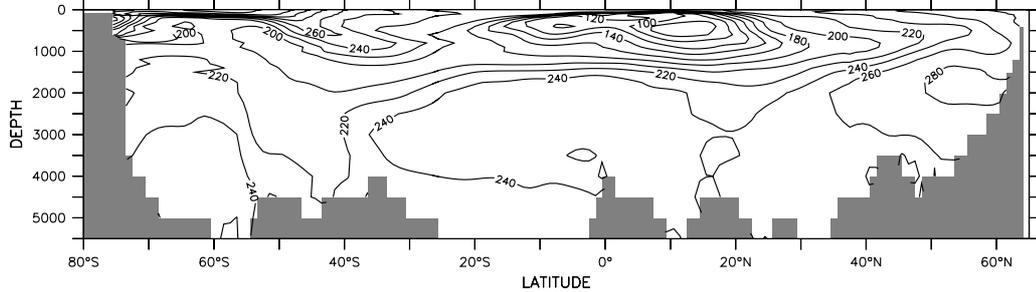
Fig. 4.9: *Oxygen distribution (in micromol/kg) along the WOCE sections P16 (150° W) in the Pacific and A16 (25° W) in the Atlantic. A) model results from the simulated year 1995; and b) observations taken from Conkright et al. (1998).*

Section P16: DIC in micromol/kg

a) Simulated distribution

b) Observed distribution

Section A16: DIC in micromol/kg

a) Simulated distribution

b) Observed distribution
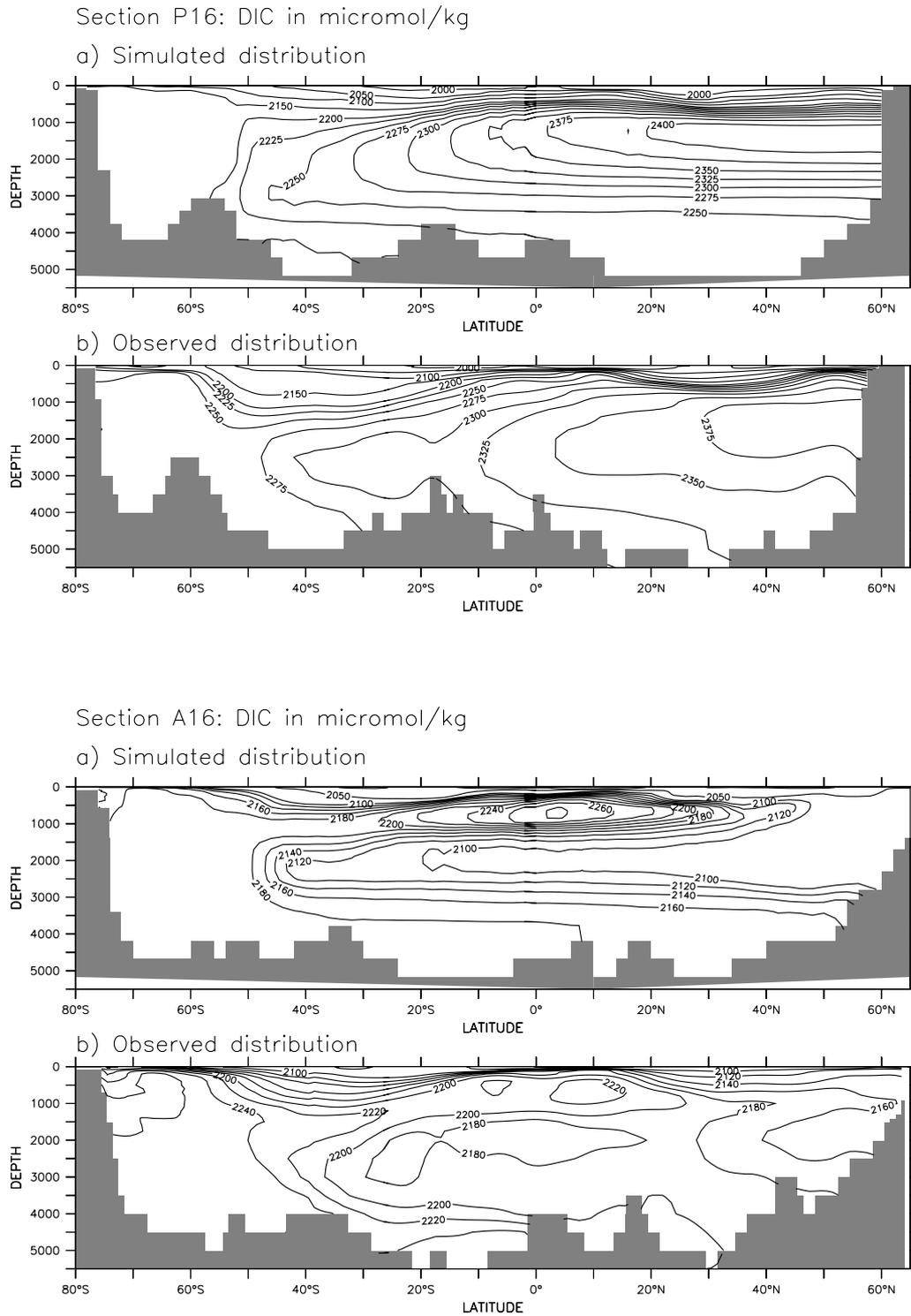

Fig. 4.10: *Dissolved inorganic carbon (DIC) distribution (in micromol/kg) along the WOCE sections P16 (150° W) in the Pacific and A16 (25° W) in the Atlantic. A) model results from the simulated year 1995; and b) observations taken from Key et al. (2004).*

Section P16: Alkalinity in micromol/kg

a) Simulated distribution
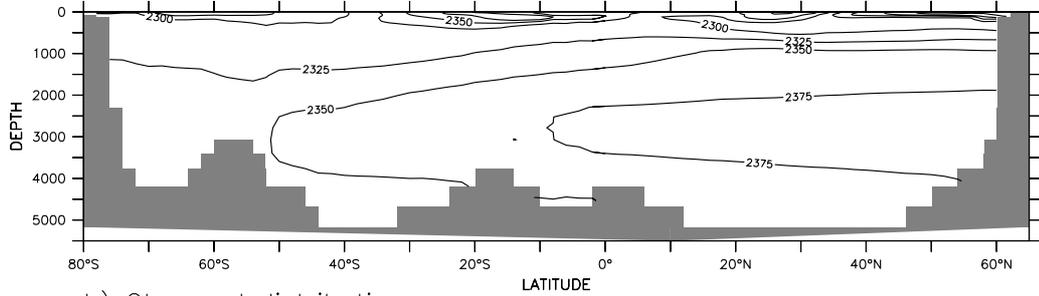
b) Observed distribution
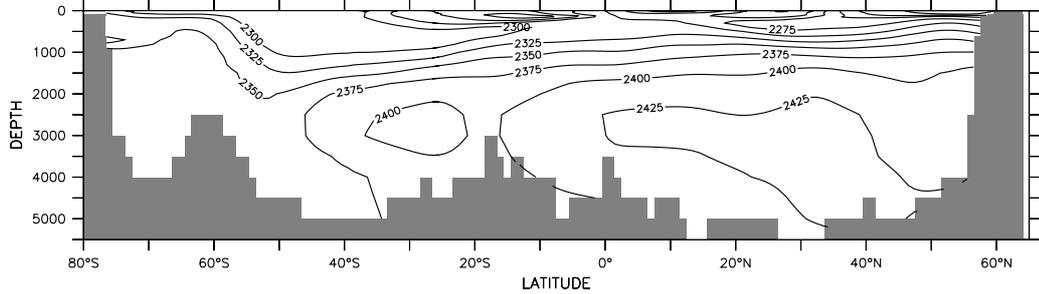
Section A16: Alkalinity in micromol/kg

a) Simulated distribution
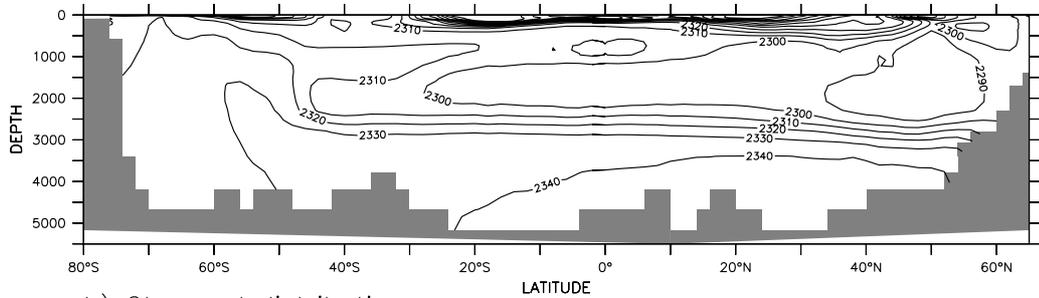
b) Observed distribution
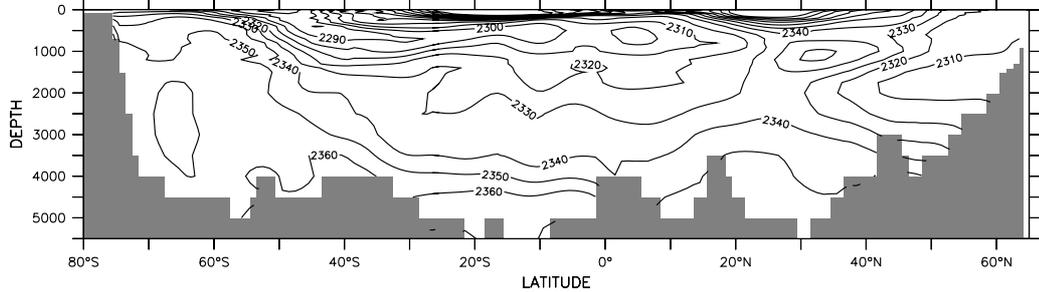
Fig. 4.11: *Total Alkalinity distribution (in micromol/kg) along the WOCE sections P16 (150° W) in the Pacific and A16 (25° W) in the Atlantic. A) model results from the simulated year 1995; and b) observations taken from Key* et al. *(2004).*

4.3.3   Mean CO_2 Flux and Partial Pressure

The global average CO_2 fluxes for the year 1995 from the anthropogenic run (AR) experiment are shown in Figure 4.12. Positive CO_2 fluxes go from the ocean to the atmosphere. Fluxes are dominated by upwelling with high outgassing of CO_2 in the equatorial Pacific, Atlantic and Arabian Sea. The weak CO_2 flux into the ocean in the mid latitudes is mostly due to the cooling of warmer waters flowing to higher latitudes. The high influx in the Southern Ocean and in the northern high-latitude areas can primarily be attributed to photosynthetic utilization of CO_2 in their respective summers. Uptake of CO_2 is also associated with deep water formation in the Labrador, Greenland, Iceland and Norwegian Seas.
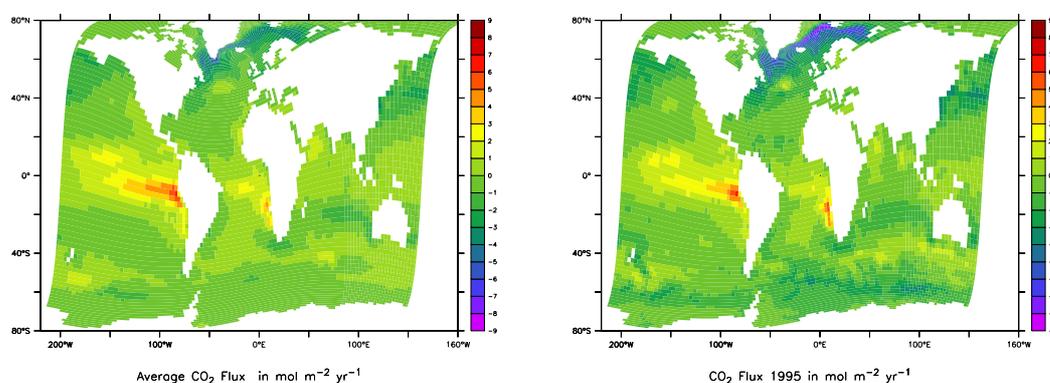

Fig. 4.12: *Left: CO_2 flux of the control run averaged over the full 56 year NCEP/NCAR reanalysis period. Right: CO_2 flux in the simulated year 1995 from the run with anthropogenic CO_2 forcing.*

The CO_2 fluxes and the CO_2 partial pressure difference between the ocean and the atmosphere (ΔpCO_2) are connected. In Figure 4.13, the mean spatial pattern of ΔpCO_2 for the reference year 1995 of the "climatological"data compilation from Takahashi *et al.* (2002) is compared with corresponding values of the year 1995 from the AR experiment. For better comparison the model results are interpolated to the 4°x 5°grid of Takahashi *et al.* (2002). The modeled pattern agrees reasonably well with the observations, but there are local differences. For example, small areas in the Greenland, Iceland, Norway and Labrador Seas are not well resolved in the coarse grid of Takahashi *et al.* (2002). The model shows very low ΔpCO_2 in the areas during the northern summer together with a high uptake of CO_2. In low latitudes, model and data are generally in good agreement. An exception is the Arabian Sea, where the model underestimates the upwelling caused by the monsoon. In the southern hemisphere this study predicts, in comparison with Takahashi *et al.* (2002), lower ΔpCO_2 south of 50°S and higher ΔpCO_2 between 14°S and 50°S. The seasonal cycle of the model is

generally larger than in Takahashi *et al.* (2002) (data not shown).
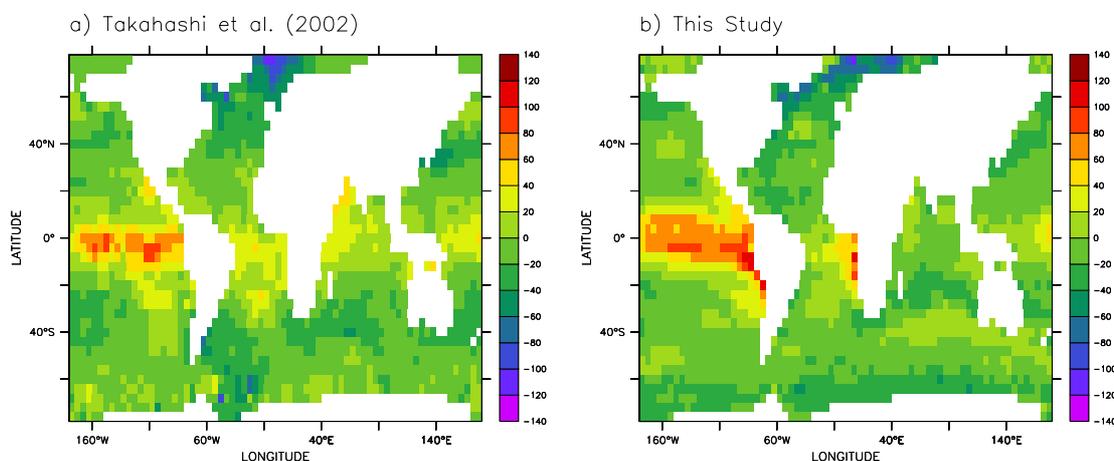
**Fig. 4.13:** *A) mean ΔpCO_2 values from Takahashi* et al. *(2002), computed for the reference year 1995 in ppm. B) mean ΔpCO_2 of the year 1995 of the anthropogenic run in ppm; interpolated to the $4°x$ $5°$ grid of Takahashi* et al. *(2002).*

CO_2 fluxes derived from the Takahashi *et al.* (2002) climatology are often used as *a priori* input in an inverse model approach (Gurney, 2002) or for carbon cycle model comparison (McKinley *et al.*, 2004). The flux is computed by multiplying the ΔpCO_2 map with a gas transfer coefficient (Wanninkhof, 1992), using the 10 m wind speed from the year 1995 of the NCEP/NCAR reanalysis. But one has to be aware, that if ΔpCO_2 is a fix climatology the flux is a linear function of the gas exchange coefficient. In the real ocean and in coupled carbon cycle models, the CO_2 flux and pCO_2 are not independent and the total CO_2 flux is relatively insensitive to the gas exchange parameterization This subject is discussed in more detail in section 7.2 and CO_2 fluxes from Takahashi *et al.* (2002) are compared to results from this work in table 6.4.

5. INTERANNUAL CO$_2$ FLUX VARIABILITY

5.1 Introduction

Atmospheric CO$_2$ data show high natural variability on interannual and decadal timescales (Keeling and Whorf, 2004). This natural variability is larger than the changes in emissions and is mainly caused by variations in land and ocean carbon cycle. Estimates of the interannual variability of the sea-to-air CO$_2$ flux differ considerably. Ocean model simulations forced with ECMWF or NCEP/NCAR reanalysis products (Le Quéré *et al.*, 2000; Obata and Kitamura, 2003; McKinley *et al.*, 2004) find an interannual sea-to-air CO$_2$ flux variability of ±0.4 to ±0.5 PgC yr^{-1}. In contrast, studies combining CO$_2$, δ^{13}C and O$_2$ data indicate a sea-to-air flux variability between ±1.0 PgC yr^{-1} and ±2.5 PgC yr^{-1}, but all with the inevitably uncertainties. (Joos *et al.*, 1999; Rayner *et al.*, 1999a; Keeling *et al.*, 1995; Francey *et al.*, 1995).

This chapter is organized as follows. Section 5.2 contains a discussion of the global variability patterns. Single regions which are of high importance for the global sea-to-air CO$_2$ flux are discussed in detail in sections 5.3 to 5.6. Focus is on the processes which are relevant for the marine carbon cycle in each single regions. If not stated otherwise all results in this chapter are taken from the control run (CR) of the main experiment as described in chapter 3.

5.2 Global Variability

Empirical orthogonal function (EOF) analysis is one way to determine the most significant pattern of the flux variability. The EOFs are the Eigenvectors of the Covariance Matrix, therefore EOF analysis is a technique that can be used to identify patterns of simultaneous variation (Storch and F.W.Zwiers, 1999). The first EOF (EOF1, figure 5.1) explains 28% of the global interannual variance. The pattern is mostly focused in a wide range around the equator with a center just off the coast of Peru in the Equatorial Pacific. Clearly the pattern can be interpreted as the El Niño Southern

Oscillation and the Pacific Decadal Oscillation. The second EOF (EOF2, figure 5.1) still explains over 11% of the global interannual variance. It is more difficult to clearly associate the second (and higher-order) EOF with a physical process, because it is constrained to be orthogonal to the first EOF, but one can still see that the dominating patterns are within the North Atlantic and the "Roaring Forties" in the Southern Ocean. Both pattern are discussed in more detail in section 5.3.

First EOF in mol C m^2 yr^{-1} Second EOF in mol C m^2 yr^{-1}
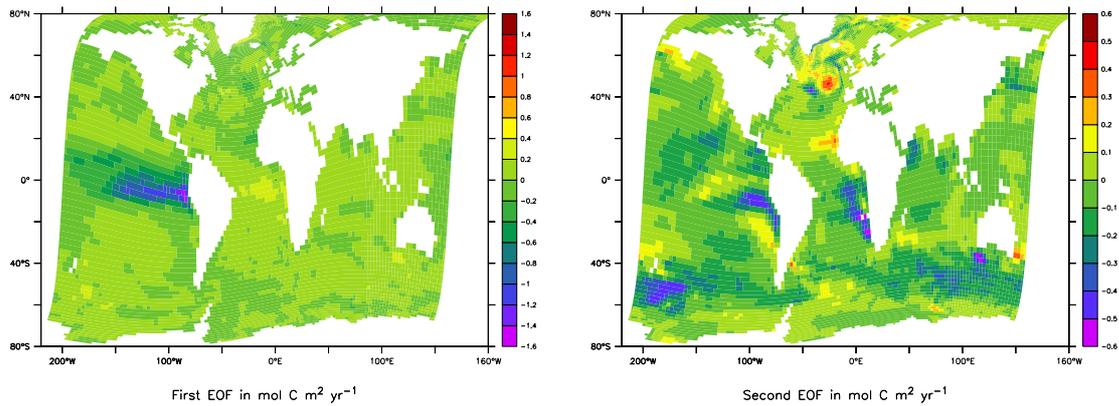
Fig. 5.1: *First and second Empirical Orthogonal Function (EOF1 and EOF2) of the interannual CO$_2$ flux variance over the full 56 year simulation period.*

CO$_2$ flux variability (2 Sigma in gC m^{-2} yr^{-1})   Average CO$_2$ Flux in mol m^{-2} yr^{-1}
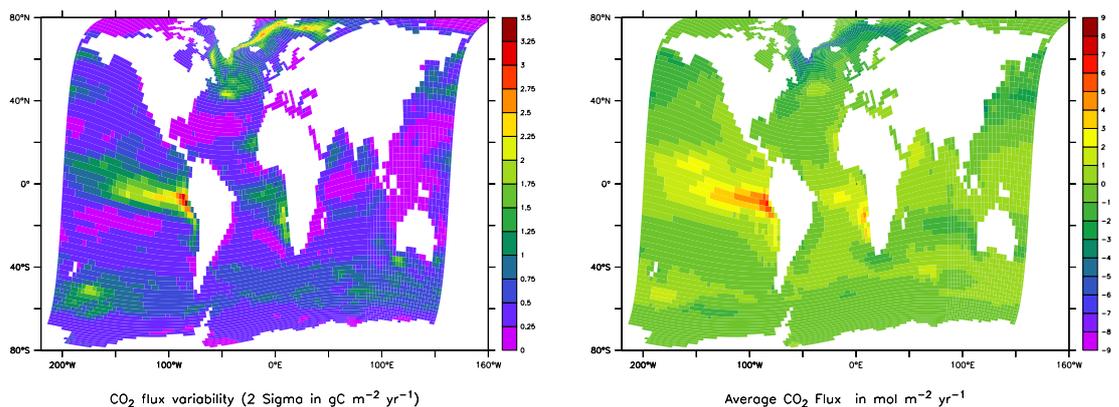
Fig. 5.2: *Left:Interannual CO$_2$ flux variability ($2\,\sigma$) of the control run for the full 56 year NCEP/NCAR reanalysis period. Right: CO$_2$ flux of the control run averaged over the full 56 year NCEP/NCAR reanalysis period.*
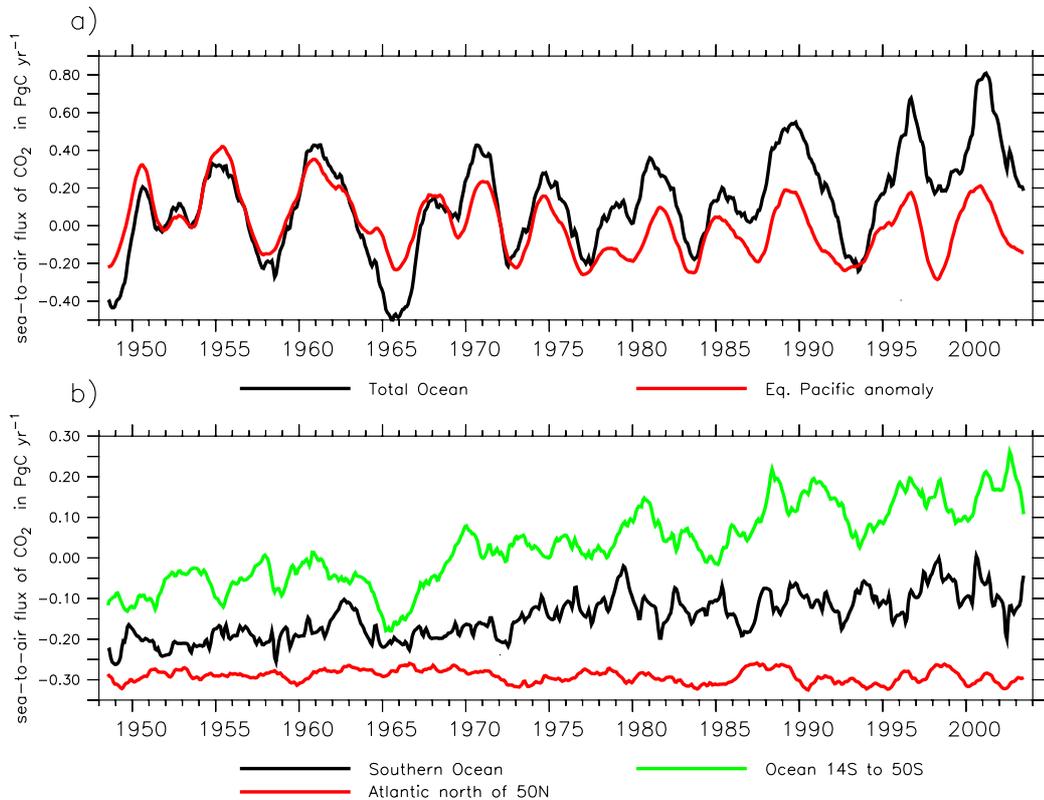
Fig. 5.3: *Simulated sea-to-air fluxes of CO_2 in $PgC\,yr^{-1}$ of the control run (CR), smoothed with a 12 month running mean. a) CO_2 flux anomaly in the equatorial Pacific and the CO_2 fluxes of the total ocean. b) CO_2 fluxes for the area from $14°\,S$ to $50°\,S$, the Southern Ocean south of $50°\,S$ and the Atlantic north of $50°\,N$.*

Figure 5.2 shows a global picture of the average sea-air CO_2 flux on the left and the interannual CO_2 flux variance on the right. Identical to the pattern of the EOF analysis there are three regions with high interannual variability. First, the equatorial Pacific (see section 5.3) that dominates the interannual CO_2 flux variability in our simulation with over 65%. Second, the Southern Ocean (see section 5.4) that accounts for over 20% of the interannual CO_2 flux variability and, in the AR experiment, for one third of the global uptake of anthropogenic CO_2. It shows the highest trend of all regions throughout the NCEP/NCAR reanalysis period. Third, the deep water formation regions in the North Atlantic, Greenland, Iceland and Norwegian Seas (see section 5.5) which are of high importance for the global carbon cycle and characterized by a pronounced seasonal cycle. Regionally these areas show a very high interannual variability, but integrated over the large area (Atlantic north of 50°N) the variability is rather small. Figure

5.3 is a timeseries plot of the interannual CO$_2$ flux variability in different ocean regions for 1948-2003. The global annual CO$_2$ flux variability for 1948-2003 is ± 0.50 PgC yr^{-1} $(2\,\sigma)$. The trend originates in the southern hemisphere, and is equivalent to an overall atmospheric increase of 4.7 ppm over the 56 years. It is not related to an internal model drift, but it reflects a strengthening in the forcing wind fields.

5.3 Equatorial Pacific

The global interannual CO$_2$ flux variability is governed by the equatorial Pacific (Figure 5.3). This result is in agreement with other ocean carbon cycle model studies (Winguth *et al.*, 1994; Le Quéré *et al.*, 2000; Obata and Kitamura, 2003; McKinley *et al.*, 2004). In the control run (CR) experiment, the equatorial Pacific from 10°N to 10°S accounts for ± 0.33 PgC yr^{-1} $(2\,\sigma)$, which is about 65% of the global interannual CO$_2$ flux variability.

5.3.1 Pacific Decadal Oscillation

In addition to the interannual variability, the Pacific climate also undergoes decadal-scale shifts (Trenberth and Hurrell, 1994). This interdecadal mode of variability is represented by the Pacific Decadal Oscillation (PDO). The PDO is defined as the leading mode of the October-March SST variability poleward of 20°(Mantua *et al.*, 1993). The decadal fluctuation is less well understood than the interannual El Niño Southern Oscillation (Latif and Barnett, 1994), but alike the El Niño cycles it has strong effects on the SST and the strength of the trade winds. There is evidence for two cold phases from about 1900 to 1925 and 1950 to 1975 and warm phases from about 1925 to 1950 and 1970 to 1995 (Chavez *et al.*, 2003). The transition from one phase to the other has been labeled a regime shift. The regime shift in 1975-77, that can be seen in the Pacific Decadal Oscillation Index (figure 5.4), is also inherent in the NCEP/NCAR reanalysis. It is most pronounced in the equatorial Pacific, but it is evident in the Atlantic and the Southern Ocean, too. The simulated interannual CO$_2$ flux variability in the equatorial Pacific changes from ± 0.33 PgC yr^{-1} (1948 to 1976) to ± 0.27 PgC yr^{-1} (1977 to 2003). The wind-driven meridional overturning circulation is a good measure for the upwelling in the equatorial Pacific. The sum of both equatorial overturning cells changes from 100$\pm$11 Sv to 77$\pm$5 Sv. This goes along with a reduction of the mean outgassing of CO$_2$ from 0.70 PgC yr^{-1} to 0.58 PgC yr^{-1}. This simulated slowdown of the overturning circulation by about 25% is in agreement with observational evidence (McPhaden and Zhang, 2002).
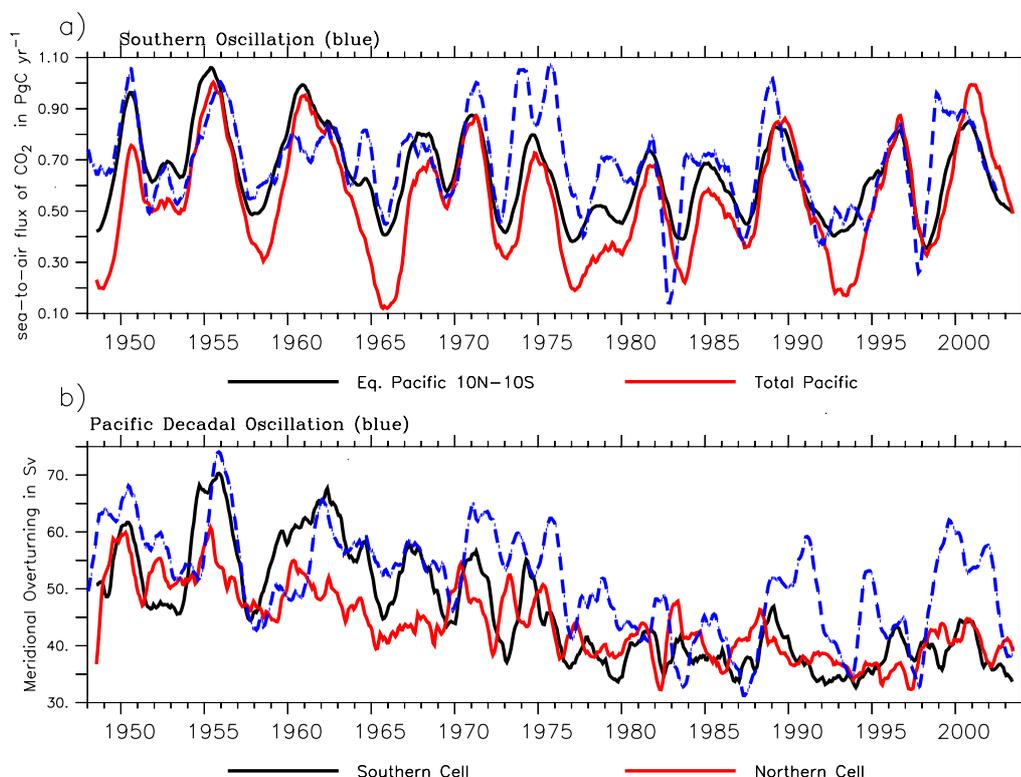
Fig. 5.4: *a) Sea-to-air CO_2 fluxes of the control run (smoothed with a 12 month running mean) of the total Pacific and of equatorial Pacific from $10°N$ to $10°S$ and $80°W$ to $135°E$. The Southern Oscillation Index is shown in blue. b) Overturning of the southern and northern Equatorial Cell in the Pacific. The Pacific Decadal Oscillation Index is shown in blue.*

5.3.2 El Niño Southern Oscillation

The equatorial Pacific has a substantial share of the interannual variability, because the changes in the ocean dynamics are acting in phase over a large region. During the unusually strong El Niño events in 1965/66 and 1991-1994 the correlation between the CO_2 flux and ocean dynamics is pronounced, resulting in the two largest sea-to-air flux minima in the 56-year period of the experiment. The flux integrated from 10°S to 10°N and from 80°W to 135°E correlates with the Southern Oscillation Index (SOI) at r = 0.67 (2 month lag, figure 5.4) and locally up to r = 0.90 (no lag, figure 5.5) in the central equatorial Pacific at 170°W.

The first EOF explains 41% of the CO_2 flux variance in the Pacific. It stretches ±10°along the equator and is centered around 110°W, with
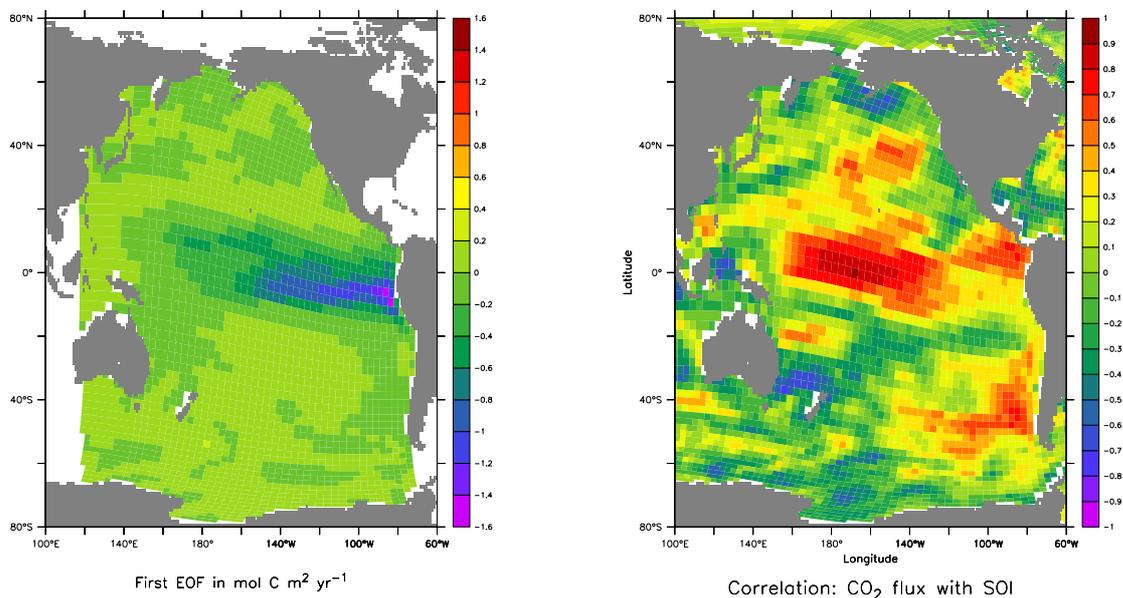
Fig. 5.5: *First Empirical Orthogonal Function (EOF1) of the interannual CO_2 flux variance in the Pacific and the correlation of the CO_2 fluxes with the Southern Oscillation Index (no lag).*

a maximum at about 4°S just of the coast off Peru. The first principal component (PC1) correlates with the SOI at r = 0.55 for 1948 to 2003, but with at r = 0.81 (no lag) for 1980 to 2003. McKinley *et al.* (2004) find the same correlation of PC1 for the Pacific for 1980 to 2003, and they also find the maximum correlation of the PC1 with zero lag and of the CO_2 fluxes for 1 to 2 month lag. Thus, the simulation by McKinley *et al.* (2004) and this study do not support the idea that the ocean CO_2 flux anomaly leads the SOI, as suggested by Rayner *et al.* (1999b).

In general, the other ocean regions are characterized by counter acting dynamical, chemical and biological processes, which result in an overall weak signal in the air-to-sea CO_2 flux anomalies.

5.3.3   Physical and Biochemical Processes

The variability of dissolved inorganic carbon (DIC), temperature (T), total alkalinity (ALK), salinity (S) and the biological productivity is controlled by the trade-wind driven, Ekman-induced upwelling. The upwelled waters from below are cold, rich in nutrients and DIC and of higher salinity and alkalinity than the surface waters. The magnitude of the CO_2 flux depends on the gas exchange and $\Delta p CO_2$. $\Delta p CO_2$ is dominantly affected by DIC, T, ALK and S. The relative importance of the different components can
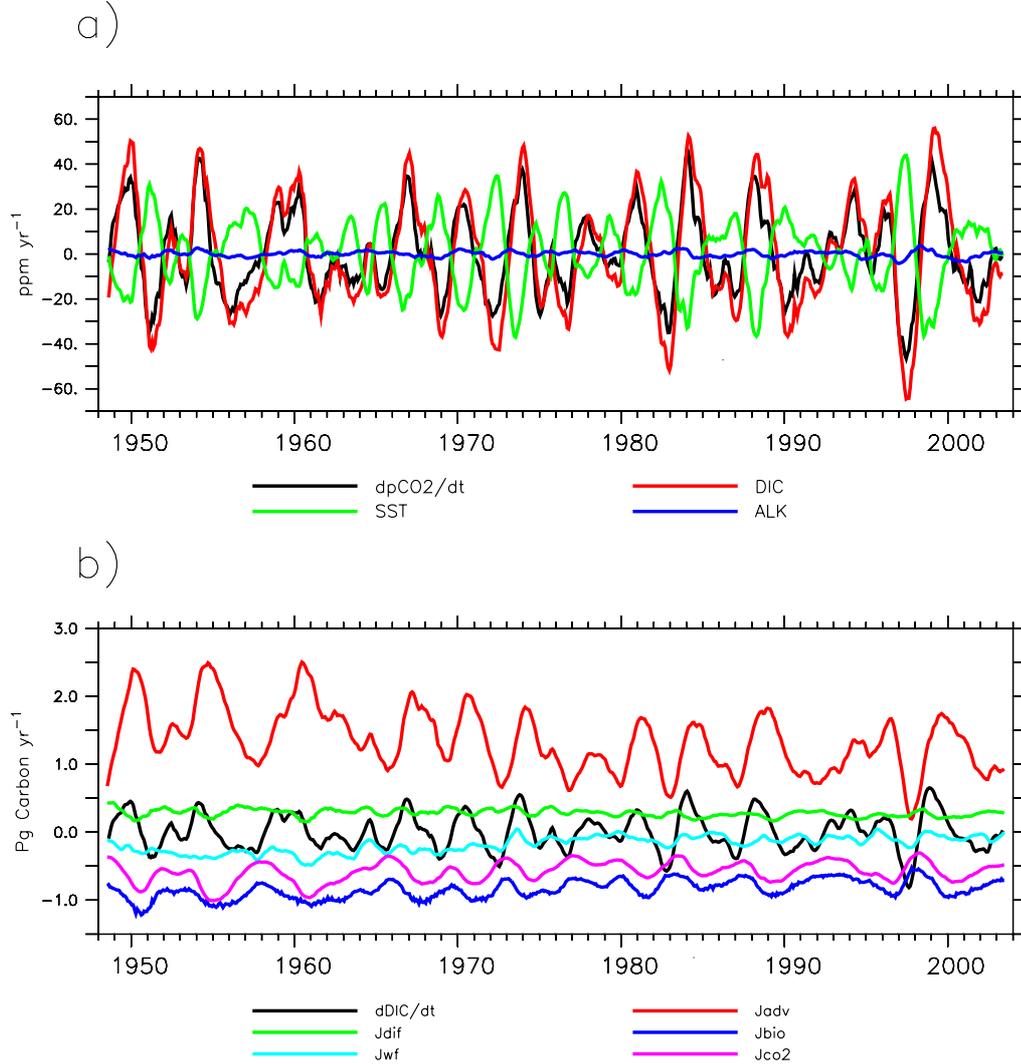
Fig. 5.6: *a) Component analysis for the terms of equation (5.1) in the surface box of the equatorial Pacific from 10° S to 10° N and 80° W to 135° E. The components for DIC and Alkalinity are normalized to salinity. b) Components of equation (5.2) for the upper 42 m of the same area. All fluxes are from the control run and smoothed with a 12 month running mean.*

be quantified by a component analysis (Takahashi *et al.*, 1993). The total derivative of $p\mathrm{CO}_2$ with respect to time can be written as:

$$
\begin{aligned}
\frac{dpCO_2}{dt} \quad &= \frac{\partial pCO_2}{\partial DIC}\frac{dDIC}{dt} + \frac{\partial pCO_2}{\partial T}\frac{dT}{dt} \\
&+ \frac{\partial pCO_2}{\partial ALK}\frac{dALK}{dt} + \frac{\partial pCO_2}{\partial S}\frac{dS}{dt}
\end{aligned}
\tag{5.1}
$$
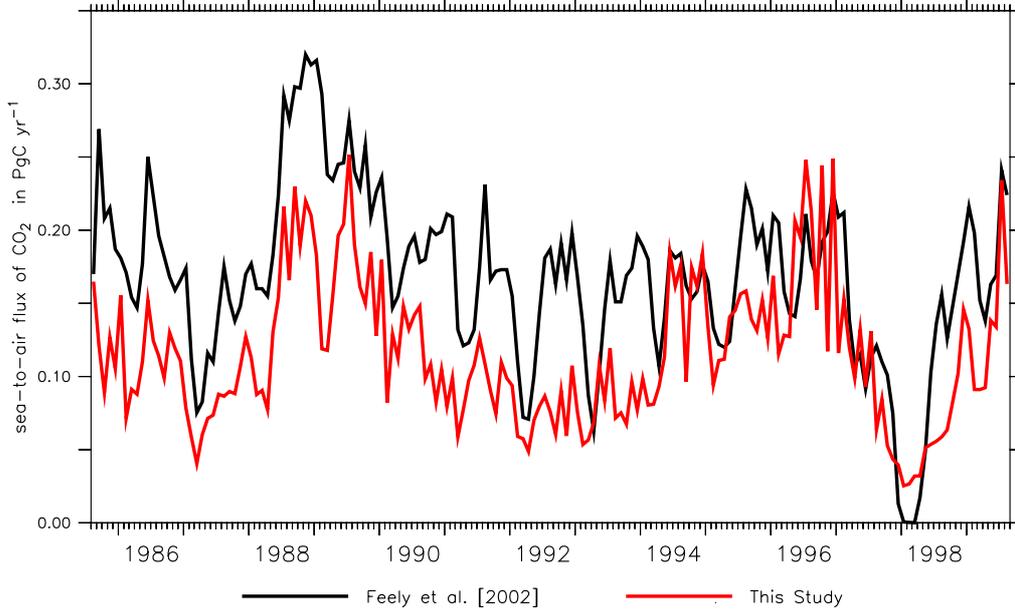
**Fig. 5.7:** *CO$_2$ flux estimate from Feely* et al. *(2002) for the equatorial Pacific from 0° to 5°S and the simulated CO$_2$ flux from the experiment with anthropogenic CO$_2$ forcing.*

Analogous to Le Quéré *et al.* (2000) figure 5.6a shows all terms of equation (5.1) except salinity, which only has a minor direct influence on pCO$_2$. The effects of temperature and alkalinity are of similar magnitude and directly anti-correlated to DIC. Together they damp the pCO$_2$ variability by about 50%. The changes in alkalinity are for the most part influenced by fresh water fluxes. Normalizing the changes in DIC and alkalinity to salinity almost annihilates the alkalinity term of equation (5.1); the DIC term of equation (5.1) changes likewise, so the sum of both remains. The variation of the DIC concentration can be written as a linear combination of sources and sinks:

$$\frac{dDIC}{dt} = J_{adv} + J_{dif} + J_{wf} + J_{co2} + J_{bio} \qquad (5.2)$$

J$_{adv}$ and J$_{dif}$ represent the transport by ocean advection and diffusion, J$_{wf}$ is the dilution or concentration from fresh water fluxes. The air-sea exchange of CO$_2$ and uptake by biological production are represented by J$_{co2}$ and J$_{bio}$. A positive sea-to-air flux as well as biological carbon export leads to a lower DIC concentration, and hence corresponds to negative J$_{co2}$ and J$_{bio}$ respectively. The influence of J$_{co2}$ and J$_{bio}$ on the total variation

is about 25% of (J_{adv}), each. J_{wf} and J_{dif} show no clear correlation and are of lesser importance. The relatively low biological productivity in the equatorial Pacific can result from iron limitation (Chavez *et al.*, 1999; Coale *et al.*, 1996). In the model, the fairly small influence of the biological production on the variability of DIC is related to the limitation by iron. Obata and Kitamura (2003) suggested, that incorporating such a limitation would increase the CO_2 flux variability. Results from a sensitivity study with this model, however, show a 35% decrease of the CO_2 flux variability in the equatorial Pacific, due to the limitation by iron (see section 7.1). First, an almost complete utilization of all upwelled nutrients within the equatorial region ultimately leads to a higher export and more remineralization of organic material and hence to a higher nutrient and DIC concentration underneath the Equator. Strong upwelling events, associated with e.g. La Niña events, bring the accumulated DIC to the surface, causing a strong outgassing of CO_2 from the ocean to the atmosphere. Second, the complete utilization of nutrients is resulting in very low oceanic pCO_2 during times of weak upwelling, associated with e.g. an El Niño event. In average conditions like 1995/96 about 0.6 PgC yr^{-1} are released to the atmosphere, which is slightly lower than the in situ and satellite derived estimates of 0.9±0.6 PgC yr^{-1} from Chavez *et al.* (1999). In association with the strong El Niño event in 1997/98 we find a reduction to 0.2 PgC yr^{-1}, which is in agreement with the observational evidence of 0.2±0.14 PgC (Chavez *et al.*, 1999). A comparison of the modeled CO_2 flux with an extensive data compilation by Feely *et al.* (2002) for the equatorial Pacific (0°to 5°S) is shown in Figure 5.7. The modeled fluxes and the variability agree reasonably well with the estimates from Feely *et al.* (2002), but the flux extremes are rather on the low side. The absolute collapse of the upwelling in the first half and its recovery in the second half of 1998 is not completely reproduced by the model. This might be due to the coarse resolution of the model and to deficiencies in the NCEP/NCAR reanalysis over the tropical Pacific region. For example, Chen (2003) has evaluated four wind products, including the NCEP/NCAR reanalysis and the new Florida State University (FSU) subjective analysis, suggesting that the single largest discrepancy in wind stress are detected after the 97/98 El Niño. In the FSU analysis a strong and persistent westerly wind anomaly exists, but this changes are not produced by the NCEP/NCAR reanalysis. Also, the FSU analysis produces a stronger easterly anomaly in wind stress in the month preceding the 1997/98 El Niño.

5.4   Southern Ocean

The global display of the standard deviations ($2\,\sigma$) in Figure 5.2 shows the highest interannual CO_2 flux variability in the region from 40°S to 60°S (±0.1 PgC yr^{-1} with the trend subtracted). The first EOF explains 23% of the CO_2 flux variance in the Southern Ocean south of 40°S with most of
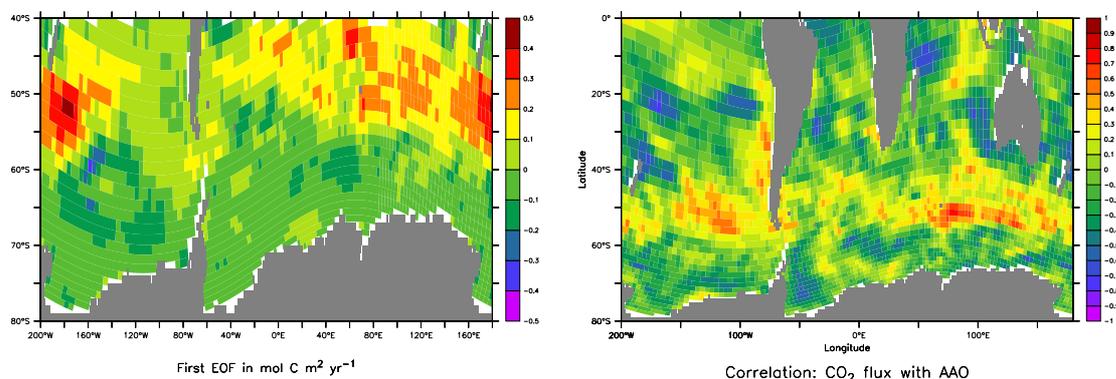
Fig. 5.8: *First Empirical Orthogonal Function (EOF1) of the interannual CO$_2$ flux variance in the Southern Ocean and the correlation of the CO$_2$ fluxes with the Antarctic Oscillation (AAO) Index (no lag).*

the structure between 40°S to 60°S. The first principal component (PC1) correlates with the AAO at r = 0.88 for 1948 to 2003 (no lag).

5.4.1   Interannual Variability

The trend in the region from 40°S to 60°S is 0.005 PgC yr^{-1} per year in the CR experiment. An important factor determining the air-sea CO$_2$ flux is the mixed layer depth, that is related to the buoyancy fluxes and the wind stress. The wind stress, modeled mixed layer depth, and the CO$_2$ fluxes show a high correlation with the Antarctic Oscillation (Thompson and Solomon, 2002, AAO, figure 5.9). Increased mixing leads to an increased CO$_2$ flux out of the ocean in the CR experiment, as deeper waters with higher DIC are mixed to the surface. In the experiment with anthropogenic CO$_2$ the uptake of anthropogenic CO$_2$ is also increasing, because anthropogenic CO$_2$ penetrates faster into the deeper layers due to enhanced ventilation.

The first EOF also shows a lateral structure different for the Indian, Atlantic and Pacific sector of the Southern Ocean. Also the interannual variability and the trend are different in each sector. Figures 5.10 to 5.12 plots the CO$_2$ flux in the Indian, Atlantic and Pacific Ocean together with the components of equation 5.2, which influence the interannual variations of DIC in the upper water column. Roughly all oceans from 14°S to 50°S show the same trend. But as the southern Pacific is clearly under the influence of the El Niño Southern Oscillation, the southern Atlantic and Indian Ocean show a much more random flux pattern with some decadal variation and a pronounced minimum in the 1960s. In the southern Indian Ocean the sea-air CO$_2$ flux is negative while in the southern Atlantic and

Pacific the sea-air CO_2 flux is positive. In the Southern Ocean from 50°S to Antarctica the Pacific sector is the only region with a strong trend, but the interannual variability is weak and noisy. The Indian and Atlantic sector have almost no trend but show some decadal structure.
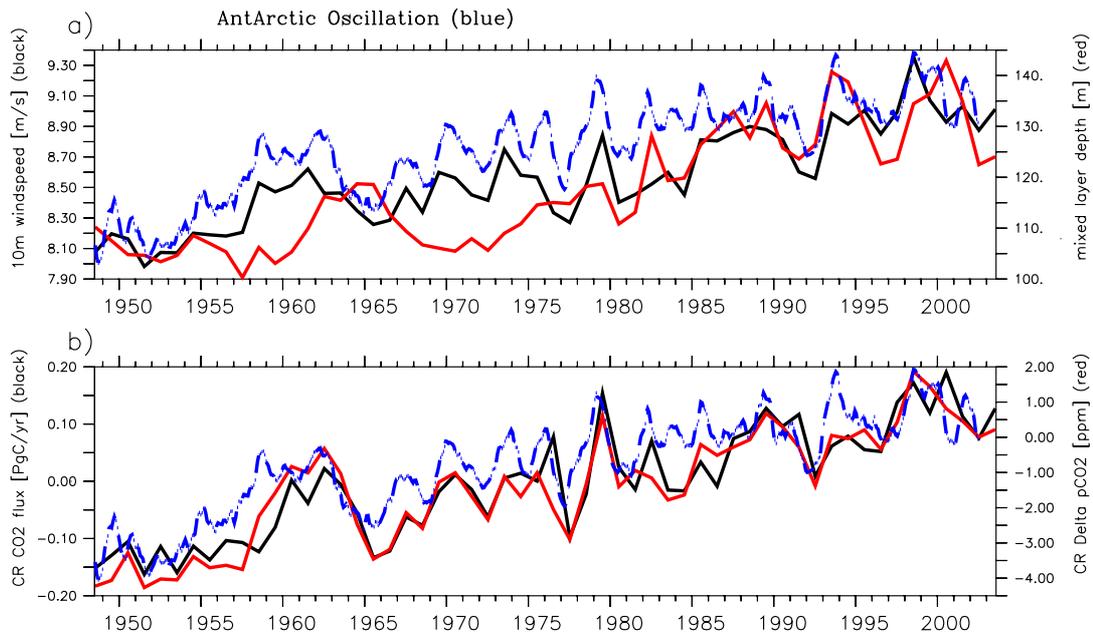
Fig. 5.9: *Yearly means for the Southern Ocean from 40°S to 60°S. a) Anomaly in the uptake of anthropogenic CO_2 (AR experiment) and the average mixed layer depth. b) CO_2 flux and ΔpCO_2 from the control run (CR). Shown in blue is the Antarctic Oscillation (AAO) Index.*
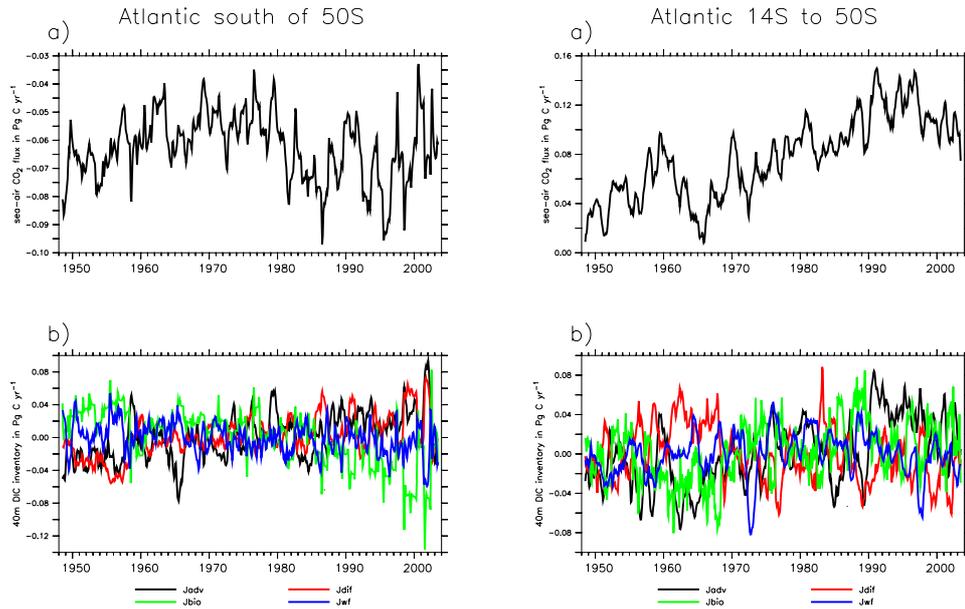
Fig. 5.10: *A) Sea-to-air CO$_2$ flux and B) components of equation (5.2) for the upper 42 m for the Atlantic sector of the Southern Ocean from 14°S to 50°S and south of 50°S. All fluxes are from the control run and smoothed with a 12 month running mean.*
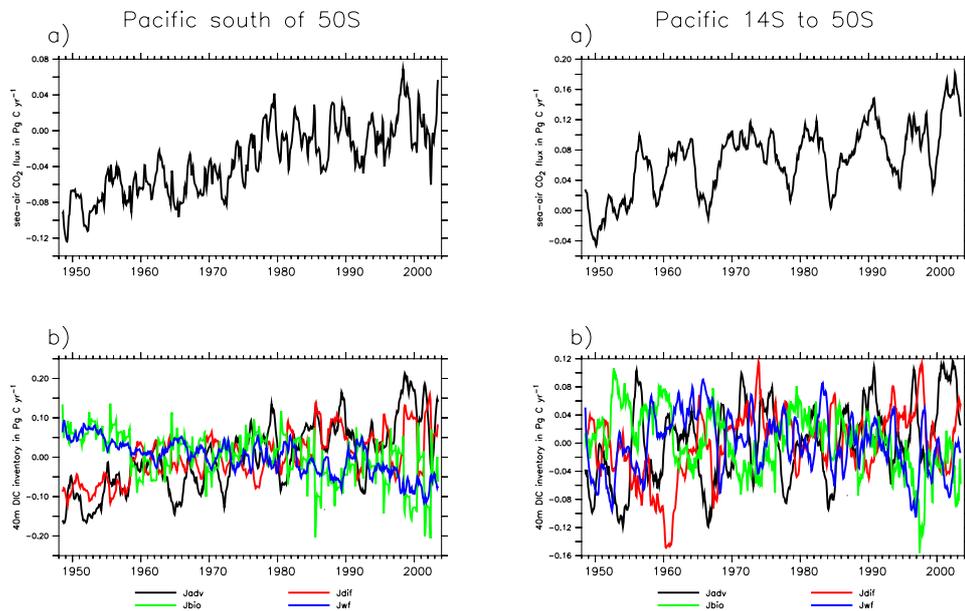
Fig. 5.11: *A) Sea-to-air CO$_2$ flux and B) components of equation (5.2) for the upper 42 m for the Pacific sector of the Southern Ocean from 14°S to 50°S and south of 50°S. All fluxes are from the control run and smoothed with a 12 month running mean.*
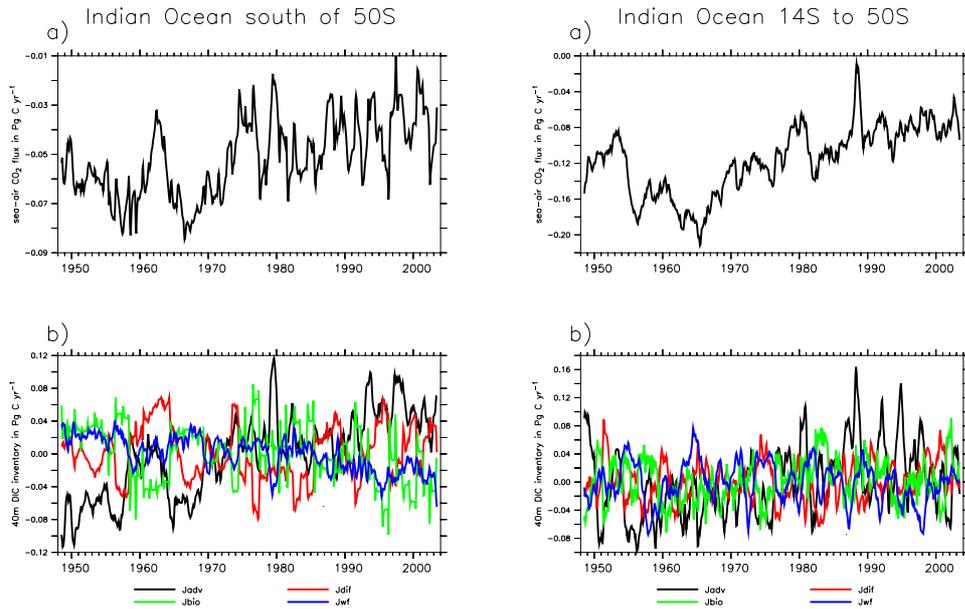
**Fig. 5.12:** *A) Sea-to-air CO_2 flux and B) components of equation (5.2) for the upper 42 m for the Indian Ocean sector of the Southern Ocean from $14°S$ to $50°S$ and south of $50°S$. All fluxes are from the control run and smoothed with a 12 month running mean.*

5.4.2   Annual Cycle

The seasonal cycle of pCO$_2$ in the Southern Ocean is controlled by biological production in summer and deep mixing in winter. The model has a strong seasonal cycle with a large CO$_2$ influx in December and January and outgassing from February to May. Figure 5.13 shows the seasonal cycle of all components of equation 5.1.

The CO$_2$ fluxes calculated from the climatology from Takahashi *et al.* (2002) show a weak seasonal cycle with a minimum influx of CO$_2$ in June/July. Atmospheric inversions by Roy *et al.* (2003) and Gurney (2004) indicate a stronger cycle, Roy *et al.* (2003) even find a weak outgassing for February to May, but their seasonal cycle is still less pronounced than in the model simulation.

5.5   North Atlantic

It is generally accepted that the high northern latitudes in the Atlantic are a strong sink for CO$_2$. The modeled CO$_2$ flux in the North Atlantic north of 50°N is - 0.31 PgC yr^{-1} on average in the control run and -0.41 PgC yr^{-1} on average for 1990-99 in the experiment with anthropogenic CO$_2$. In contrast,
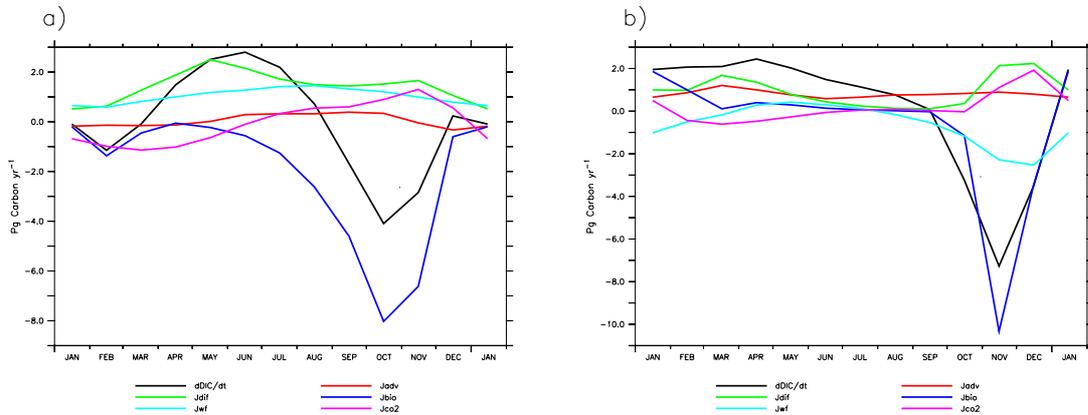
Fig. 5.13: *Climatological seasonal cycle of all components of equation 5.1 for the Southern Ocean a) from 14°S to 50°S and b) from 50°S to Antarctica.*

the simulated interannual CO$_2$ flux variability is rather small at ± 0.04 PgC yr^{-1}, what is in agreement with the minor interannual variability McKinley *et al.* (2004) find in their simulation. This seems to be in contradiction to the areas of high interannual CO$_2$ flux variability in the high northern latitudes in figure 5.2. However, the areas are small and the variations are not in phase with each other, resulting in a relatively low interannual variability of the entire North Atlantic. The first, second and third EOF of the annual CO$_2$ flux only represent 13%, 12% and 10% of the interannual variability respectively.
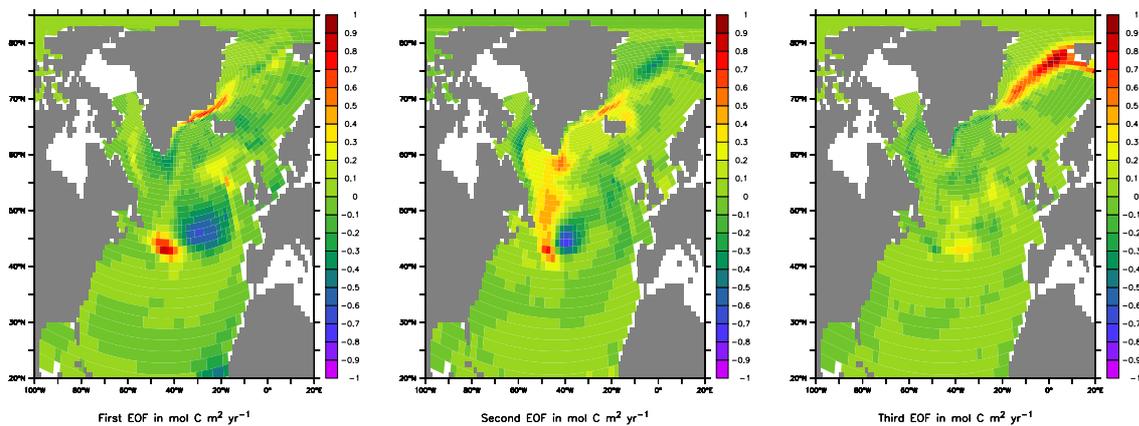
Fig. 5.14: *First, second and third Empirical Orthogonal Function of the annual CO$_2$ flux in the North Atlantic.*

5.5.1 Annual Cycle
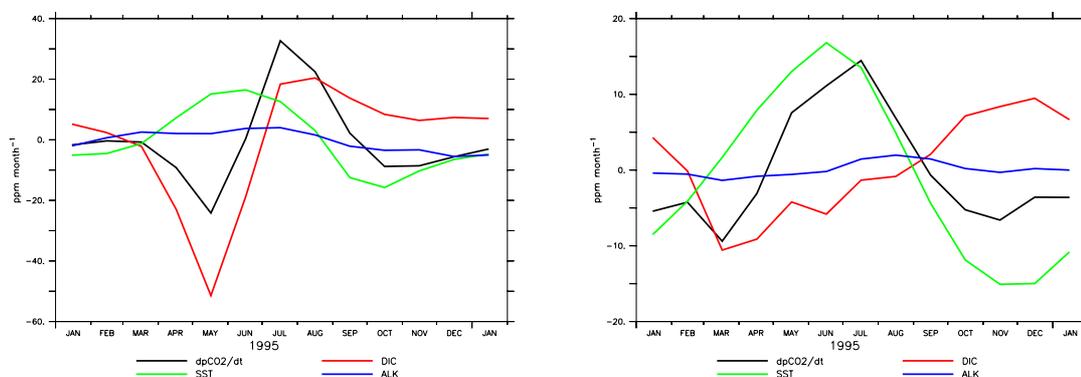
Fig. 5.15: *Left: Annual cycle of all terms of equation 5.1 for the North Atlantic from 50°N on northward. Right: Annual cycle of all terms of equation 5.1 for the North Atlantic from 50°N to 14°N.*

The North Atlantic has a strong seasonal cycle compared to the relatively low variability on interannual scales. The simulated annual cycle of all terms of equation 5.1 for the North Atlantic from 50°N to 14°N and from 50°N on northward (figure 5.15) indicates that DIC changes largely drive the pCO$_2$ in the subpolar North Atlantic, while temperature effects dominate the cycle in the subtropics. Results for the seasonal cycle of this model are in agreement with the analysis of the pCO$_2$ climatology by Takahashi *et al.* (2002) and are consistent with the study of McKinley *et al.* (2004). Differences between the seasonal cycles mostly reflect interannual changes in the convective mixing, mostly at the end of the winter. Following the mixing the biological export in the spring bloom neutralizes most of DIC anomaly.

5.5.2 Interannual Variability

An important index to analyze physical variability in the North Atlantic, the GIN and Labrador Seas is the North Atlantic Oscillation (NAO) index (Hurrell *et al.*, 2003; Hurrell, 1995). The NAO is the see-saw type difference between the a subtropical high-pressure system near the Azores and a subpolar low near Iceland. Gruber *et al.* (2002) and Bates *et al.* (2002) both have evaluated an 18-year time series of upper-ocean (mode water) DIC observations near Bermuda (Station S at 32°10‘N,64°30‘W and the BATS site at 31°50‘N,64°10‘W). The deduce that the carbon variability at this station is largely driven by variations in winter mixed layer depth (MDL) and by SST anomalies. They argue, that MLD and SST anomalies occur

in a basin-wide coordinated pattern associated with the NAO. Extrapolated over the full North Atlantic they estimate a possible variability of the CO$_2$ sink by ± 0.3 PgC yr^{-1}. This flux would be very significant for the net global variability, but the CO$_2$ flux point correlation in figure 5.21 demonstrates that according to the model is is not possible to interpolate the flux variability at Bermuda over the basin. This result is consistent with the study of McKinley *et al.* (2004).

Correlation: annual SST and winter NAO   Correlation: Shallow winter MLD and winter NAO
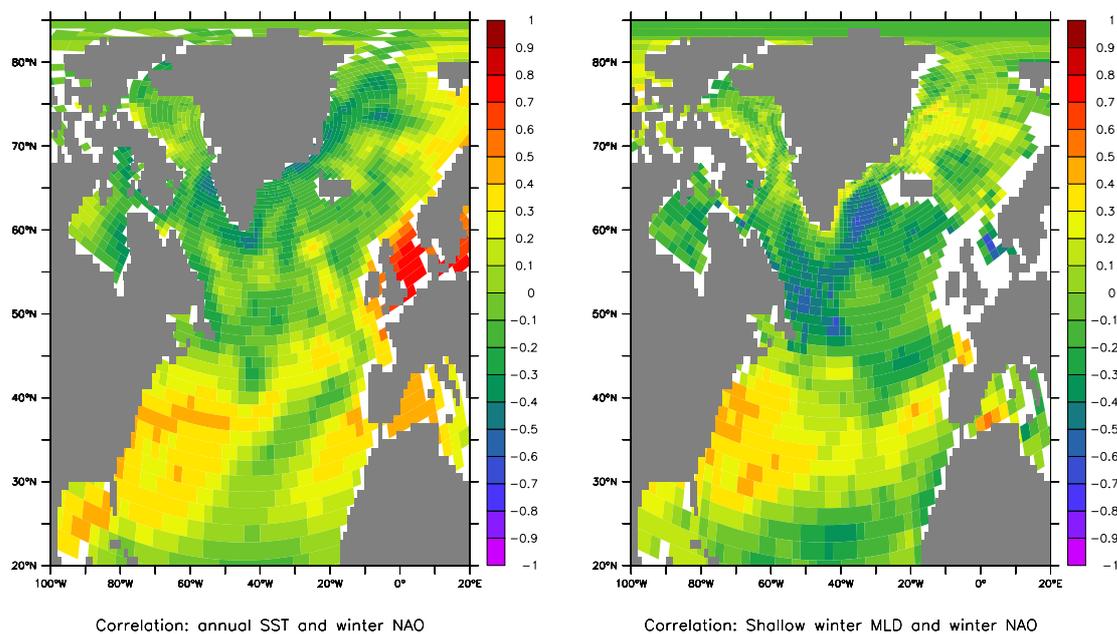
Fig. 5.16: *Correlations of the wintertime North Atlantic Oscillation (NAO) with yearly averages of the Sea Surface Temperature (SST) and shallow winter mixing (negative MLD).*

The next step to find the reason for the discrepancy is to analyze the behavior of the postulated physical drivers of the variability. Figure 5.16 shows the correlation pattern of the wintertime NAO with the annual averages of the SST and low wintertime MLD. In the North Atlantic a strong pressure difference (NAO high) correlates with positive SST anomalies in the subtropics and negative anomalies in the subpolar gyre (Cullen *et al.*, 2002). Along with higher SSTs goes a more shallow winter mixing (figure 5.16). This basin-wide coordinated pattern is reproduced in our simulation. Also reproduced is a positive correlation of the sea-air CO$_2$ flux with the SST and the NAO near Bermuda (figure 5.17), but this correlation does not scale over the full basin as postulated by Gruber *et al.* (2002) and Bates *et al.* (2002). Even so the physical variability is captured in the simulation and it does show a correlation with the NAO Index, the CO$_2$ flux in the

Correlation: CO_2 Flux and NAO

Correlation: Annual CO_2 Flux and annual SST
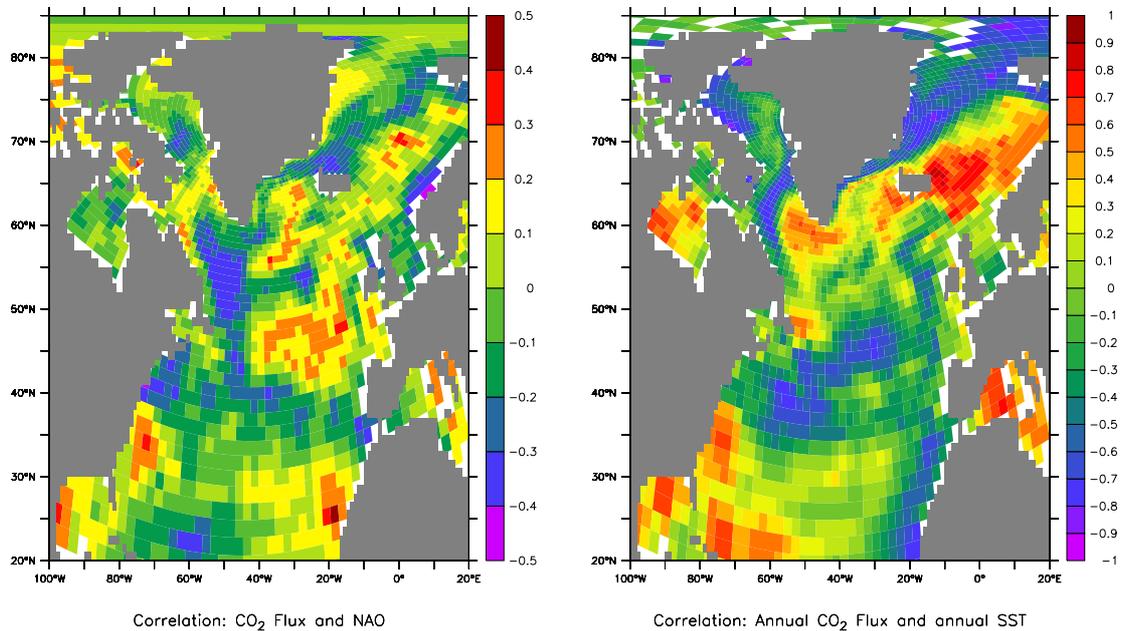
**Fig. 5.17:** *Correlation of the North Atlantic Oscillation (NAO) with yearly averages of the sea-air CO_2 flux and a correlation of yearly averages of the sea-air CO_2 flux with Sea Surface Temperatures.*

total North Atlantic shows no distinct correlation with the NAO Index, and is of minor importance for the net global variability.

So why does this model and the study by McKinley *et al.* (2004) indicate a decoupling of the interannual CO_2 flux variability from its physical drivers in the North Atlantic? In general, the surface DIC concentration and SST are the most important parameters for the CO_2 partial pressure (pCO_2). From the correlation plot in figures 5.16 and 5.17 it is obvious that they are not acting in phase over the North Atlantic. To understand which of the competing influences controls the annual CO_2 flux variation the areas of positive ($r \geq 0.5$) and and negative correlation ($r \leq$ -0.5) of the CO_2 flux with surface DIC (figure 5.18) are analyzed in figure 5.19. Regions defined by $r \geq 0.5$ are mostly in the subtropics and along the Gulf Stream, while most of the subpolar gyre is correlated with $r \leq$ -0.5. In regions defined by $r \geq 0.5$ most of the interannual CO_2 flux variations in this simulation is positively correlated to surface DIC variations and so is the winter MLD, while the SST anomalies in those areas are anti-correlated. The mechanism is straight forward. A high MLD brings deeper water which is cold and rich in DIC to the surface. Colder waters lower the pCO_2 but the dominating effect on the pCO_2 is the DIC concentration. A long term trend to higher windspeed over the simulation period also causes a trend in the CO_2 fluxes. Despite
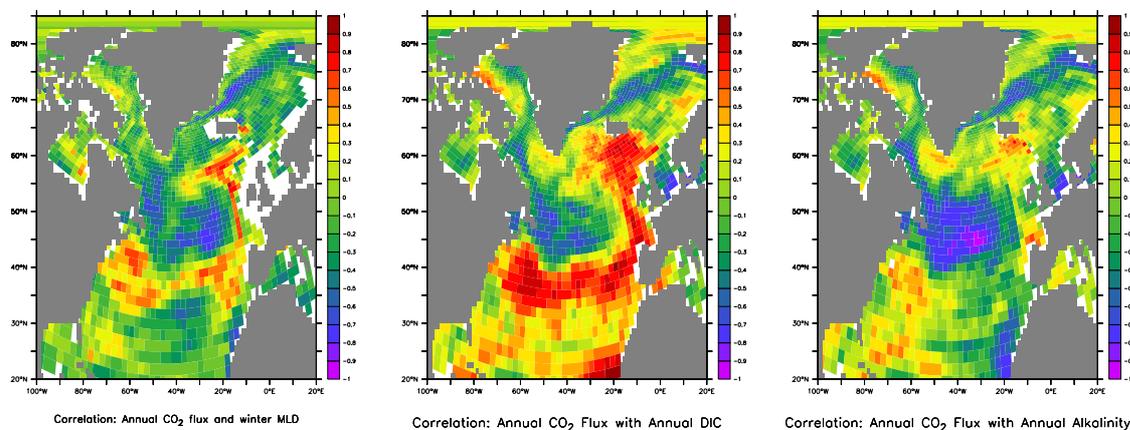
Fig. 5.18: *Left: Correlation of yearly averages of the sea-air CO$_2$ flux with the winter Mixed Layer Depth (MLD). Middle: Correlation of yearly averages of the sea-air CO$_2$ flux with surface (40m) DIC concentration. Right: Correlation of yearly averages of the sea-air CO$_2$ flux with surface (40m) Alkalinity concentration.*

the trend to higher winter mixing the SST is rising due to atmospheric warming.

In contrast, fluxes in regions defined by r ≤ -0.5 are anti-correlated to surface DIC variations and the winter MLD. But counter-intuitively the CO$_2$ flux is also anti-correlated to the SST. As in regions defined by r ≥ 0.5 the trend to higher windspeed also causes rising surface DIC concentrations and there also is a trend towards higher SSTs. At the same time the influx of CO$_2$ (negative sea-to-air CO$_2$ flux) increases over the simulation period and the interannual variability of the influx is correlated with the windspeed.

Reason for the different behavior of the two regions is the alkalinity distribution in the upper 300m. Not only subsurface DIC is mixed to the surface but also subsurface alkalinity. The approximation equation 6.2 shows that pCO$_2$ is proportional to DIC but anti-proportional to alkalinity. Figure 5.19 shows that in the region defined by r ≤ -0.5 the approximated pCO$_2$ is dominated by changes in alkalinity, not by DIC. In other words: Whether the CO$_2$ flux is correlated or anti-correlated with the MLD depends on the relation of DIC and alkalinity in the subsurface water column. Figure 5.20 shows profiles of DIC and alkalinity for regions defined by r ≥ 0.5 and by r ≤ -0.5. Simulated DIC distributions are similar in both regions with a strong gradient to higher DIC in deeper waters. The simulated alkalinity is almost uniform in the region defined by r ≥ 0.5. Stronger mixing will increase the surface DIC, but without changing the surface alkalinity much. In contrast, the simulated alkalinity in the region defined by r ≤ -0.5 shows a even stronger gradient then DIC. Stronger mixing will therefore increase
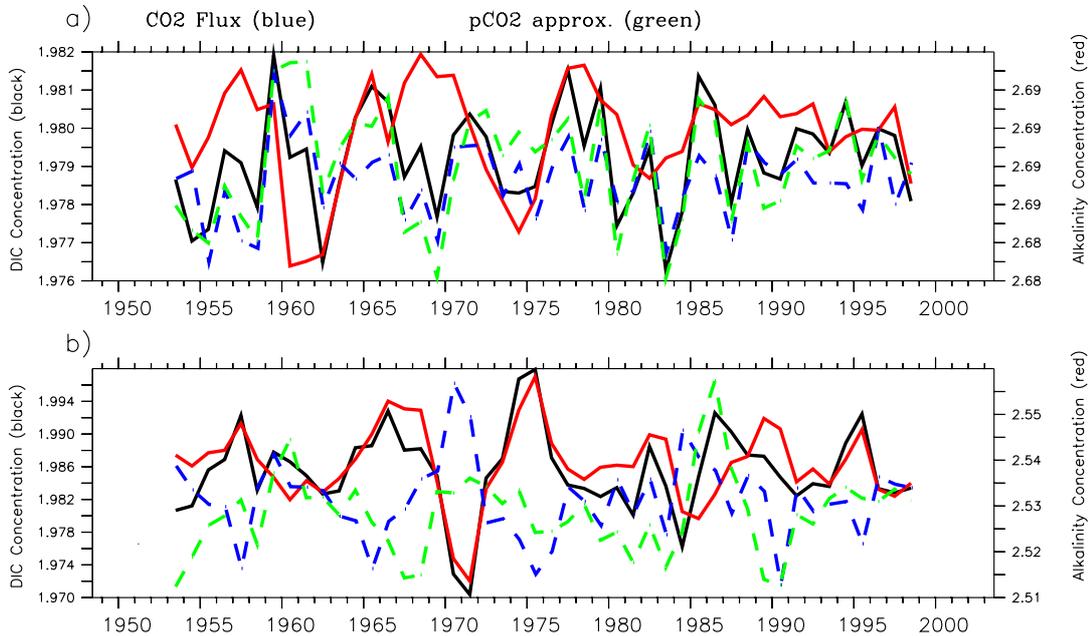
Fig. 5.19: *Annual values of surface (40m) DIC concentration (black, in mmol/l), surface alkalinity (red, in mmol/l), sea-air CO_2 flux (blue, in PgC yr^{-1} but shown without units) and the approximated pCO_2 from equation 6.2 (green, in ppm but shown without units). All parameters are plotted for a) areas from figure 5.18 where the correlation of the sea-air CO_2 flux with surface DIC concentrations is greater than 0.5 and b) areas from figure 5.18 where the correlation of the sea-air CO_2 flux with surface DIC concentrations is lower than -0.5. All trends are removed by subtracting a 10 years running mean.*

the surface DIC, but also change surface alkalinity even more. This explains the relationship of DIC and alkalinity in the two regions as shown in figure 5.19.

The dependence of pCO_2 to the SST is ignored in equation 6.2 and is of minor importance for the interannual variability in the North Atlantic. The dominating factor for the interannual flux variability and the long term trend is the increasing surface DIC in one region and the increasing surface alkalinity in the other region, both driven by wind induced mixing.

McKinley *et al.* (2004) have postulated that the interannual variability in the subpolar gyre and the subtropics is driven by the same processes as seasonal cycle. Their simulation indicates that DIC changes largely drive
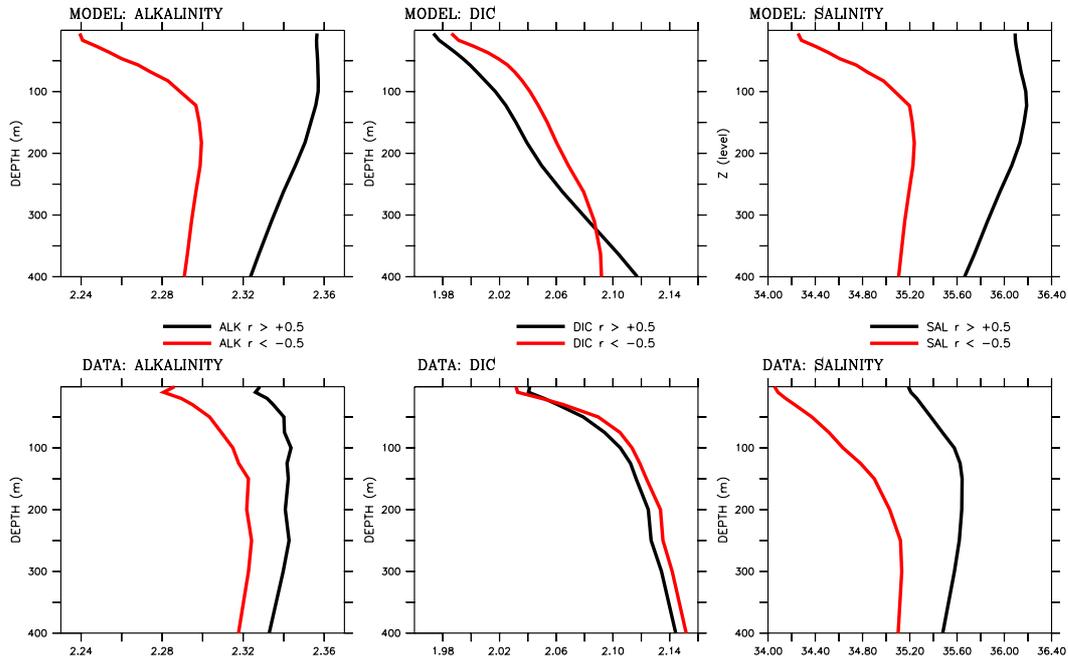
Fig. 5.20: *Annual average profiles of DIC concentrations [mmol/l] and alkalinity [mmol/l]. Simulation results for the model year 1995 and compiled data from the GLODAP project (Key et al., 2004). All parameters are plotted for areas from figure 5.18 where the correlation of the sea-air CO$_2$ flux with surface DIC concentrations is greater than 0.5 and for areas from figure 5.18 where the correlation of the sea-air CO$_2$ flux with surface DIC concentrations is lower than -0.5.*

the pCO$_2$ variance in the subpolar North Atlantic and temperature effects dominate the variance in the subtropics. The comparison of simulated profiles of DIC concentrations and alkalinity. with compiled data from the GLODAP project (Key *et al.*, 2004, figure 5.20) shows that the vertical DIC gradient is underestimated in both regions, whereas the vertical alkalinity gradient is overestimated in the area defined by r ≤ -0.5. This could be an indication that the model may overestimate the influence of alkalinity, and could therefore underestimate the total interannual CO$_2$ variability in the North Atlantic.
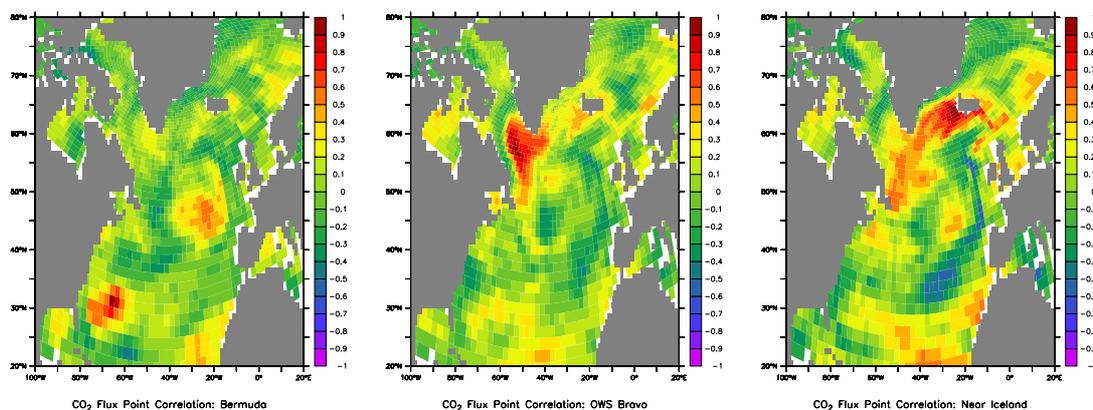
Fig. 5.21: *Point correlation between the simulated annual CO_2 flux variability in the North Atlantic and left: Bermuda; middle: OWS Bravo in the Labrador Sea and right: Iceland.*
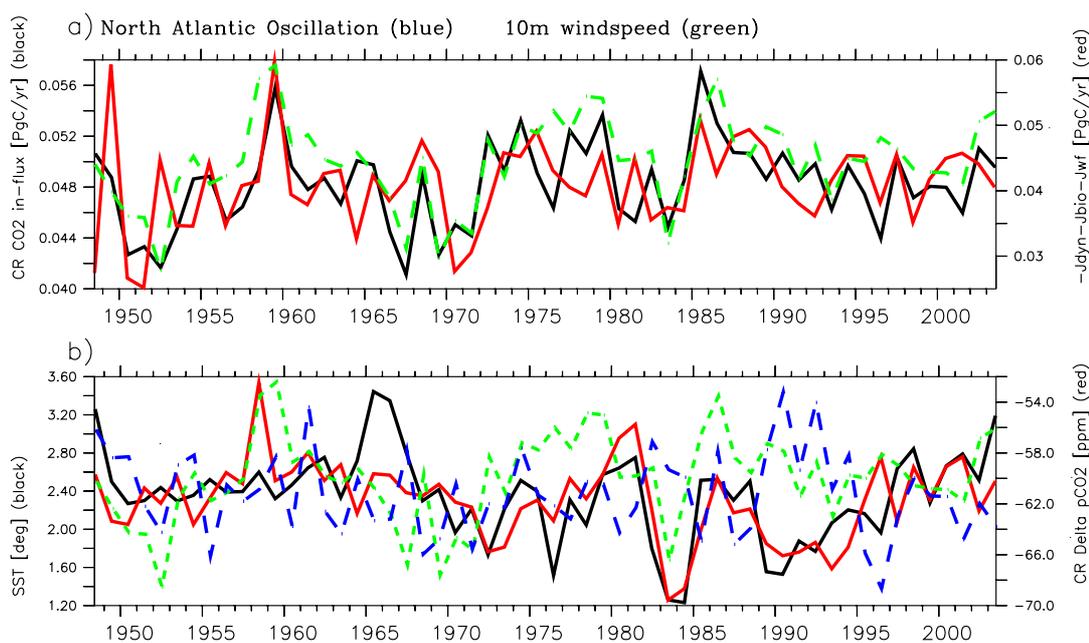
Fig. 5.22: *Analysis for ice-free regions of the Labrador Sea. A) Sea-air CO_2 flux (in black) and the sum of the terms $-J_{adv} - J_{dif} - J_{wf} - J_{bio}$ of equation (5.2 (in red). B) SST in $^\circ$Celsius (in black) and ΔpCO_2 (in red). The NAO Index and the 10 m windspeed are shown without units. All results are given as annual averages.*
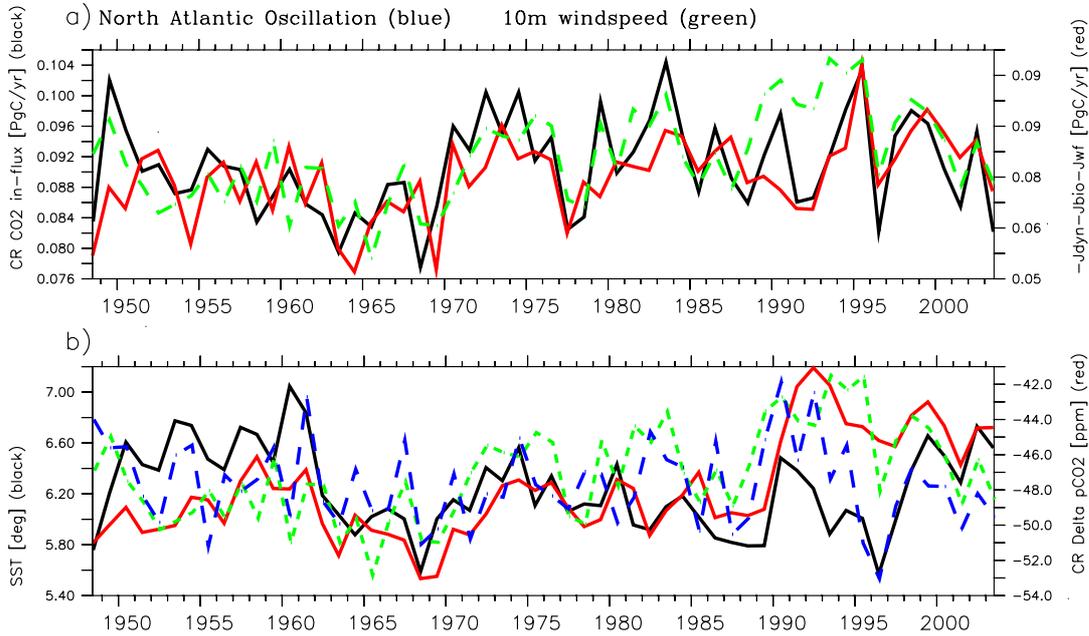
Fig. 5.23: *Analysis for ice-free regions of the Greenland, Iceland and Norwegian Sea. A) Sea-air CO_2 flux (in black) and the sum of the terms $-J_{adv} - J_{dif} - J_{wf} - J_{bio}$ of equation (5.2 (in red). B) SST in °Celsius (in black) and ΔpCO_2 (in red). The NAO Index and the 10 m windspeed are shown without units. All results are given as annual averages.*

5.6   Greenland, Iceland, Norwegian & Labrador Seas

Figure 5.2 shows areas of high interannual CO_2 flux variability in the high northern latitudes. Flux variability in the Arctic Ocean, parts of the Labrador Sea and along the coast of Greenland is strongly influenced by the interannual variations of the sea-ice cover. Areas with in-phase interannual CO_2 flux variations are generally small. The point-correlations in figure 5.21 demonstrate the limited correlation-range in the simulation and that the flux variability due to the sea-ice cover is not in phase with the variability in ice-free regions. All of this leads to a the relatively low interannual variability of the entire high latitude North Atlantic.

Variability in ice-free regions is analyzed in figure 5.23 and 5.22. The Greenland, Iceland and Norwegian (GIN) Seas and the Labrador Sea are deep water formation areas with an average CO_2 flux directed from the

atmosphere to the ocean and DIC transported from the surface into the deep ocean. CO_2 flux into the ocean, downward transported of DIC by ocean dynamics and biological export are highly correlated to the windspeed. In the Labrador Sea, the 10 m wind speed and the CO_2 fluxes are not correlated with the NAO index, whereas in the GIN Sea the 10 m wind speed is weakly correlated and so are the fluxes (see also figure 5.17).

Correlation: Annual CO_2 flux and pCO_2 pCO$_2$ Difference: Constant Minus Variable Gas Exchange
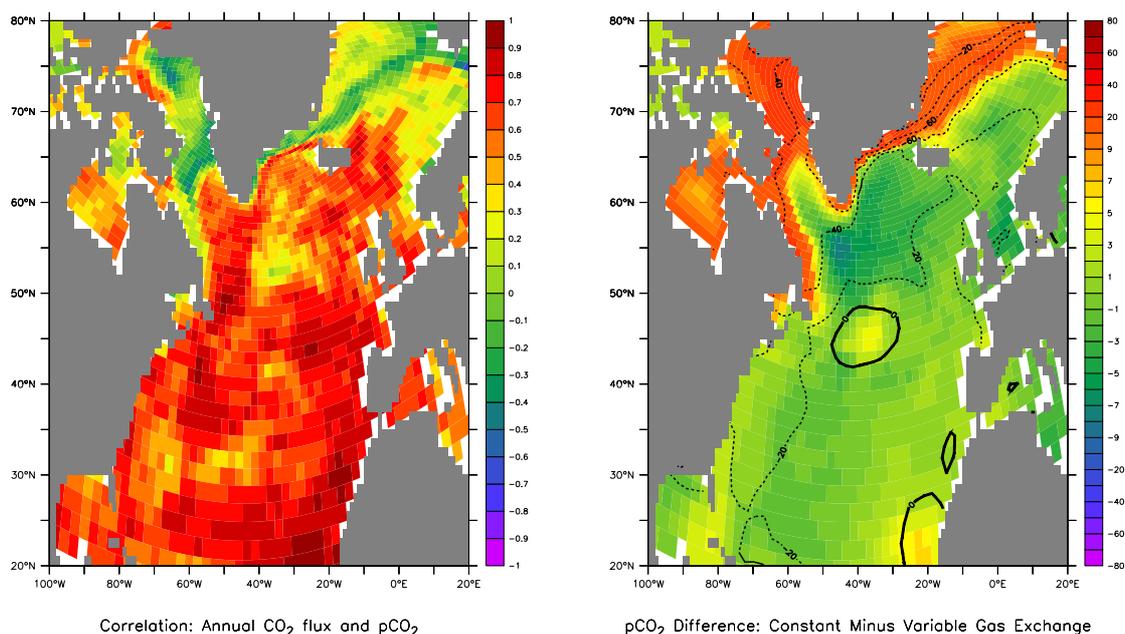
Fig. 5.24: *Left: Correlation of yearly averages of the sea-air CO_2 flux with the average oceanic CO_2 partial pressure (pCO_2). Right: Difference of yearly average pCO_2 in ice-free regions between the standard experiment with variable gas exchange (Wanninkhof, 1992) and a sensitivity study with fixed gas exchange. The overlayed contour lines show the average ΔpCO_2 in ice-free regions of the standard experiment with negative values given on the contour lines.*

The sea-air CO_2 flux and the partial pressure difference between ocean and atmosphere (ΔpCO_2) is highly correlated over almost the total North Atlantic (figure 5.24), but in areas covered by sea-ice in winter the correlation is negative. In summer times the biological production lowers the ΔpCO_2, but in winter when the ΔpCO_2 and the wind speeds, and therefore the gas exchange are much higher, those areas are covered by sea-ice and can not equilibrate with the atmosphere. In years with a higher net CO_2 flux (this requires a higher gas exchange coefficient) the ΔpCO_2 is not as low as in year with a lower net CO_2 flux. On other words: the CO_2 flux does not follow the ΔpCO_2, but the ΔpCO_2 rather follows the CO_2 flux. If

one replaces the variable sea-air gas exchange coefficient with a fix value, as done in one sensitivity study where an average value was applied (3 m/day, see also 7.2), the pCO$_2$ in those areas changes drastically (figure 5.24). The extremely low ΔpCO$_2$ values along the coasts of Greenland and Newfoundland in the standard experiment (as indicated by the contour lines in figure 5.24), are reduced to almost zero, whereas the rest of the North Atlantic shows only minor differences.

6. ANTHROPOGENIC CO$_2$ UPTAKE

6.1 Introduction

The atmospheric CO$_2$ concentration has increased from about 280 ppm in preindustrial times to 375 ppm by 2003 (Keeling and Whorf, 2004). The observed annual rate of increase from 1980 to 1999 is about 50% of that expected from the combustion of fossil fuel, cement production and land use change. This means that only half of the anthropogenic emissions stay in the atmosphere and the other half is taken up by the ocean and the terrestrial biosphere. Various methods have been employed to constrain the CO$_2$ fluxes. Houghton *et al.* (2001) use atmospheric N$_2$/O$_2$ observations (Keeling and Shertz, 1992) to derive the rates of anthropogenic CO$_2$ uptake. Another common technique is the calculation of the land and ocean CO$_2$ fluxes from atmospheric CO$_2$ data with an inverse atmospheric transport model (Rödenbeck *et al.*, 2003; Gurney, 2002).

The oceanic uptake of anthropogenic CO$_2$ can be also estimated from global chlorofluorocarbon (CFC) data sets (McNeil *et al.*, 2003) or radiocarbon (^{13}C) (Gruber and Keeling, 2001). Sabine *et al.* (2004a) use the ΔC* method (Gruber *et al.*, 1996) to separate the small anthropogenic CO$_2$ signal from the large natural background of Dissolved Inorganic Carbon (DIC) for an extensive global data set of DIC and various gases and nutrients. The Ocean Carbon Cycle Intercomparison Project (OCMIP-2) has evaluated a suite of 19 ocean carbon cycle models with radiocarbon and CFC-11 data (Matsumoto, 2004). Results from those studies are summarized and compared to results from this study in tables 6.3 and 6.4.

6.2 Revelle Factor

Anthropogenic CO$_2$ invades the ocean by gas exchange across the air-sea interface. The highest concentrations are therefore found in surface waters. Important for the surface concentration of anthropogenic CO$_2$ is the exposure time and the buffer factor. When CO$_2$ dissolves in seawater, there is only a small change in the actual CO$_2$ concentration, because the system is buffered by CO_3^{2-} ions.

$$CO_2 \;\rightleftharpoons\; HCO_3^- + H^+$$
$$HCO_3^- \;\rightleftharpoons\; CO_3^{2-} + H^+$$
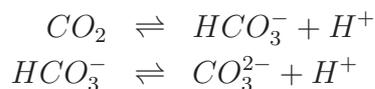
The buffer or Revelle factor (Revelle and Suess, 1957) is a quantitative expression for CO$_2$-buffering. It is defined as the ratio of the relative change in CO$_2$ concentration to the relative change in DIC concentration. The capacity of seawater to take up anthropogenic CO$_2$ is inversely proportional to the Revelle factor (see also section 2.3.3). The partial pressure (pCO$_2$) is proportional to the CO$_2$ concentration and the Revelle factor can be written as:

$$\gamma_{DIC} \;=\; \frac{\delta p CO_2}{\delta [DIC]} \frac{[DIC]}{p CO_2} \tag{6.1}$$

For practical purposes the approximation

$$p CO_2 \approx \frac{K_2}{K_0 K_1} \frac{(2[DIC] - [Alk])^2}{[Alk] - [DIC]} \tag{6.2}$$

can be applied. This yields an approximation for the Revelle factor that is temperature independent (Sarmiento *et al.*, 2004):

$$\gamma_{DIC} \;\approx\; \frac{3[Alk][DIC] - 2[DIC]^2}{(2[DIC] - [Alk])([Alk] - [DIC])} \tag{6.3}$$

Figure 6.1 shows the simulated Revelle factor for the model year 1994 and the Revelle factor calculated from data compilations for 1994, provided by the GLobal Ocean Data Analysis Project (GLODAP) [1] (Key *et al.*, 2004). In both cases the Revelle factor is calculated from DIC and total Alkalinity using the approximation from equation 6.3. The lower pictures in figure 6.1 show the anthropogenic CO$_2$ column inventory for the model simulation and for the data compilation provided by the GLODAP project, both for the year 1994. The highest anthropogenic CO$_2$ concentrations are found in the subtropical surface waters where the Revelle factor is low, and the lowest concentrations are in the Southern Ocean where the Revelle factor is high. In upwelling regions such as the Equatorial Pacific and Atlantic, intermediate-deep waters with high DIC concentrations but little anthropogenic CO$_2$ are transported to the surface. Therefore the Revelle factor is higher but the anthropogenic CO$_2$ are lower than in the surrounding regions. Concentrations in the Atlantic are generally higher than in the Pacific due to more favorable buffer factor and because of the faster ventilation. The North Atlantic deep water is the only place where large concentrations of anthropogenic CO$_2$ penetrate into mid and abyssal depth.

---

[1] Botteld data and 1°gridded distributions from the GLobal Ocean Data Analysis Project data are available through the GLODAP Web site at http://cdiac.ornl.gov/oceans/glodap/
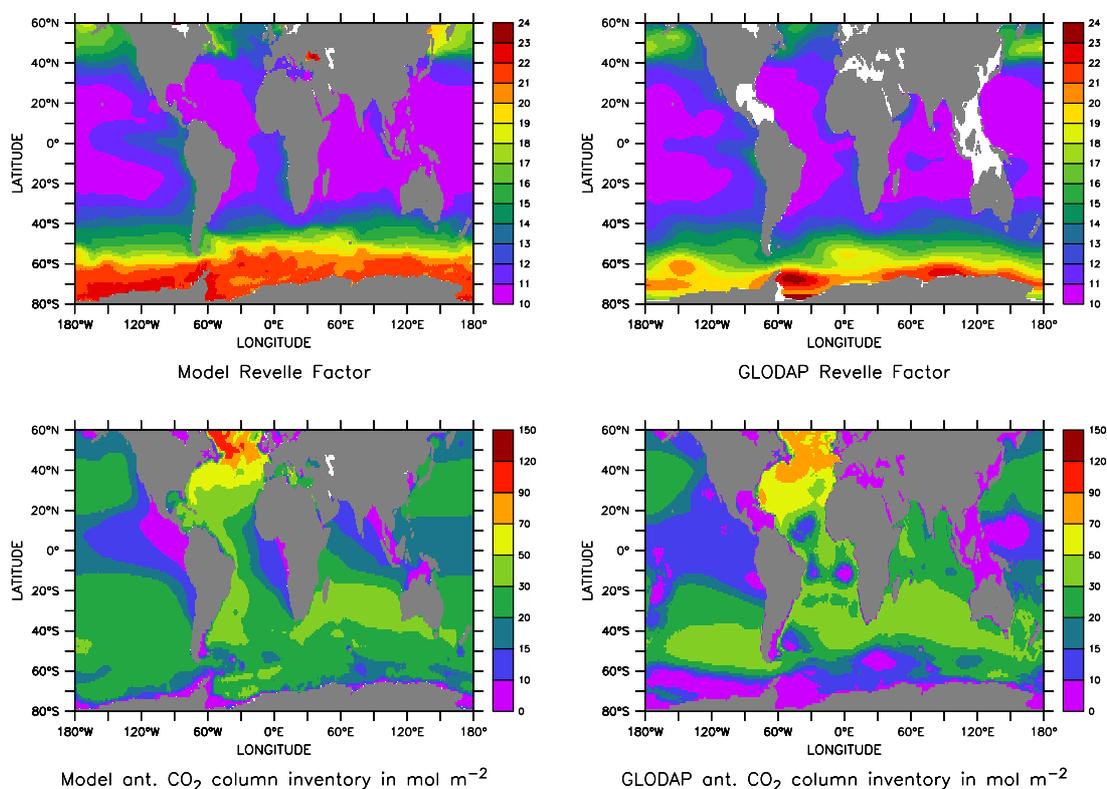
Fig. 6.1: *Revelle factor averaged over the upper 50m of the water column and anthropogenic CO$_2$ column inventory from the simulated year 1994 and data compilations for 1994 taken from GLODAP (Key et al., 2004).*

6.3 Anthropogenic CO$_2$ Uptake

We define the uptake of anthropogenic CO$_2$ as the difference between the CO$_2$ fluxes of the experiment with anthropogenic CO$_2$ forcing and the control run (AR and CR experiment). Because of the high variability and the trends in various ocean regions there is a considerable difference between the CO$_2$ flux of the AR experiment and the calculated uptake of anthropogenic CO$_2$. In upwelling regions, uptake of anthropogenic CO$_2$ means less outgassing compared to the CR. Uptake of anthropogenic CO$_2$ is high where older waters are mixed to the surface, such as in the northern and southern high latitudes and in the equatorial upwelling regions (Figure 6.3). Much of the anthropogenic carbon taken up in the high latitudes and in the upwelling regions is transported to the subtropics and stored there, mostly in the upper few hundred meters of the water-column. In the subtropics, with small anthropogenic uptake and low biological productivity, the oceanic

CO$_2$ partial pressure follows the partial pressure of the atmosphere almost directly. The deep water formation areas in the North Atlantic are characterized by a high uptake combined with large storage of anthropogenic CO$_2$.
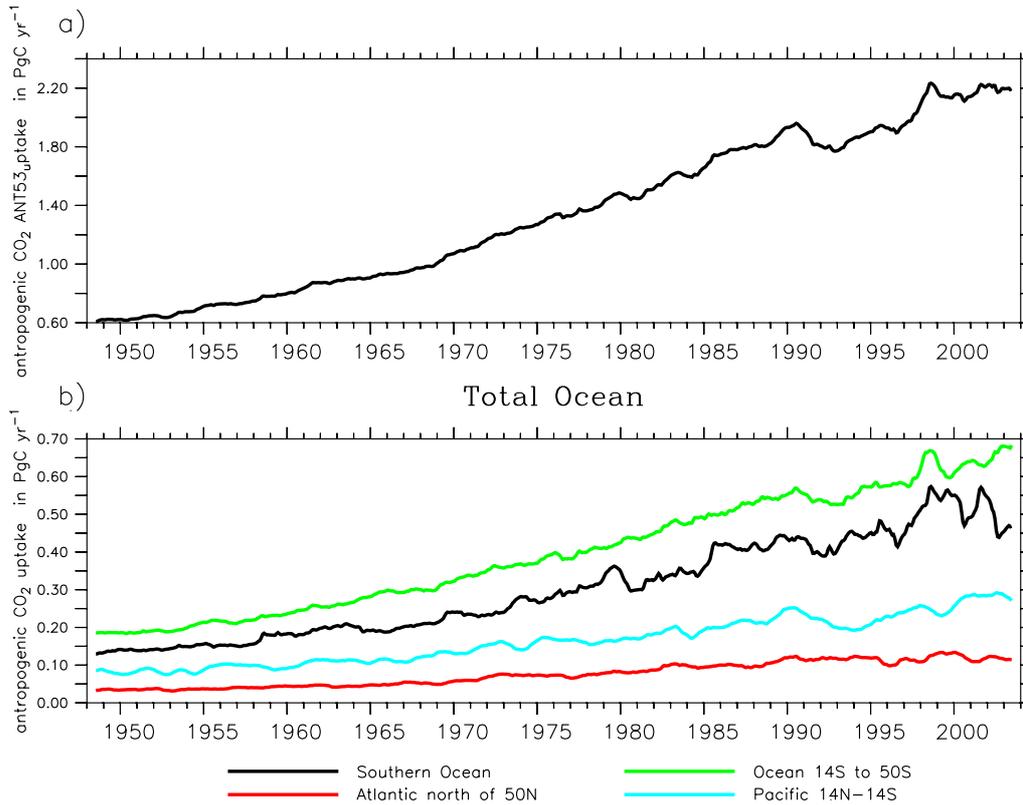
Fig. 6.2: *A) Global anthropogenic CO$_2$ uptake in PgC yr^{-1}. B) Uptake for various ocean regions in PgC yr^{-1}. Results from the run with anthropogenic CO$_2$ forcing (AR) smoothed with a 12 month running mean.*

We estimate an average uptake of anthropogenic CO$_2$ of 1.67 PgC yr^{-1} for 1980-89 and 1.94 PgC yr^{-1} for 1990-99. The interannual variability of the uptake of anthropogenic CO$_2$ is far less then the natural variability of the CO$_2$ fluxes (Figure 6.2). The phases of higher uptake mostly reflect deep mixing events in the Southern Ocean while the decrease in the 1990s is primarily caused by large scale effects in association with the El Niño events in 1993 and 1998. The model results are consistent with uptake estimates of anthropogenic CO$_2$ from CFC data (McNeil *et al.*, 2003) and within range of the coarser estimates from the oceanic ^{13}C inventory (Heimann and Maier-Reimer (1996); Gruber and Keeling (2001), see table 6.3).

In all areas, except some regions in the Southern Ocean where the mixing

Anthropogenic CO$_2$ column inventory (1994) in mol m^{-2}

Average anthropogenic CO$_2$ uptake (1990 to 1999) in mol m^{-2} yr^{-1}
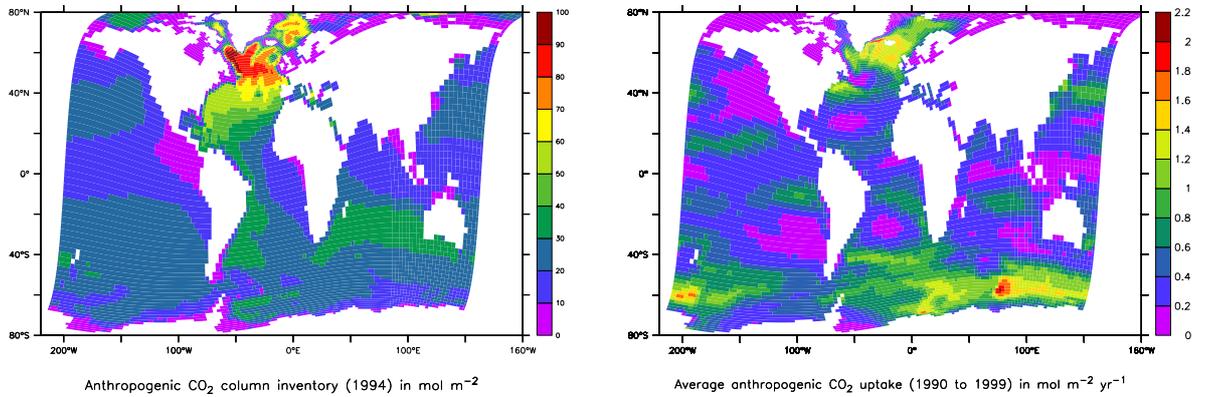
Fig. 6.3: *Left: Simulated anthropogenic CO$_2$ column inventory in the year 1994. Right: Simulated average uptake for the years 1990 to 1999.*

Time span	This Study	CFC data [a]	OCMIP-2[b]	^{13}C inventory
1980-1989	-1.67	-1.6±0.4	-1.9±0.2	
1990-1999	-1.93	-2.0±0.4	-2.2±0.2	
1970-1990				-2.1±0.9 [c]
1985-1995				-1.5±0.9 [d]

[a]McNeil *et al.* (2003) [b]Matsumoto (2004) [c]Heimann and Maier-Reimer (1996) [d]Gruber and Keeling (2001)

Tab. 6.1: Estimated uptake of anthropogenic CO$_2$ in PgC yr^{-1} .

is constantly increasing due to the wind stress, the increasing dissolved inorganic carbon (DIC) is raising the buffer factor and slowing down further uptake (Figure 6.4). First of all, the slowdown is noticeable in regions with a shallow mixed layer depth. The El Niño events in 1993 and 1998 are clearly recognizable by a decrease in uptake In figure 6.4 the El Niño events correlate with 356 ppm and 364 ppm. As a future perspective this would means that the oceanic uptake fraction within the global carbon cycle is decreasing. On the long term both positive and negative feedbacks between the ocean and the atmosphere are possible. This includes possible changes in the ocean dynamics such as circulation and stratification as well as changes in the biological production such as export and calcification (Sarmiento and Gruber, 2004).
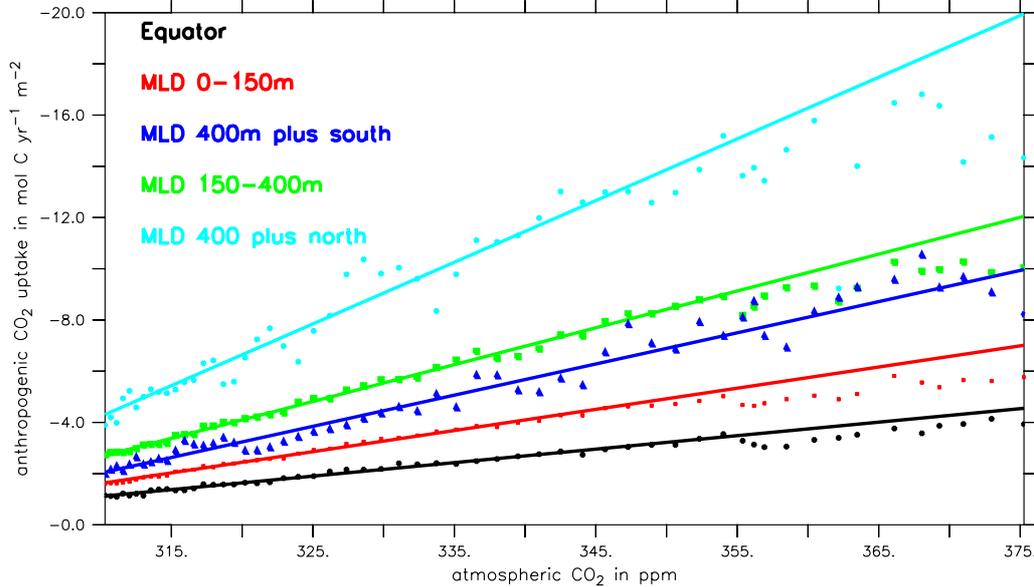
Fig. 6.4: *Yearly averages of anthropogenic CO$_2$ uptake vs. atmospheric CO$_2$ concentrations. The uptake rates are computed for the equatorial regions, regions with an average mixed layer depth of up to 150m, 150m to 400m and over 400m in the northern and southern hemisphere. The linear regression lines are computed for 310ppm to 345ppm and extended over the full range.*

6.4 Anthropogenic CO$_2$ Fluxes

The effective flux of CO$_2$ represents the sum of the natural CO$_2$ fluxes and the uptake of anthropogenic CO$_2$. Because of the trend of the fluxes of the CR experiment, the total flux of CO$_2$ into the ocean between 1980 and 2000 is about 0.18 PgC yr^{-1} smaller than the computed uptake of anthropogenic CO$_2$. The average flux of -1.49 PgC yr^{-1} for 1980-89 and -1.74 PgC yr^{-1} for 1990-99 agrees reasonably well with the estimates from atmospheric inversions (Rödenbeck *et al.* (2003); Gurney (2002); see table 6.4).

In contrast to our results, estimates from N$_2$/O$_2$ ratio measurements indicate a decreased CO$_2$ flux into the ocean from 1980-89 to 1990-99 (IPCC report, Houghton *et al.* (2001)). Their estimates assume a zero net sea-to-air flux of O$_2$. This assumption may not hold for the period 1980-99. Bopp *et al.* (2002) estimate a correction for 1990-95 of -0.5 PgC yr^{-1} using the observed heat fluxes and a modeled O$_2$ flux to heat flux relationship. Apply-
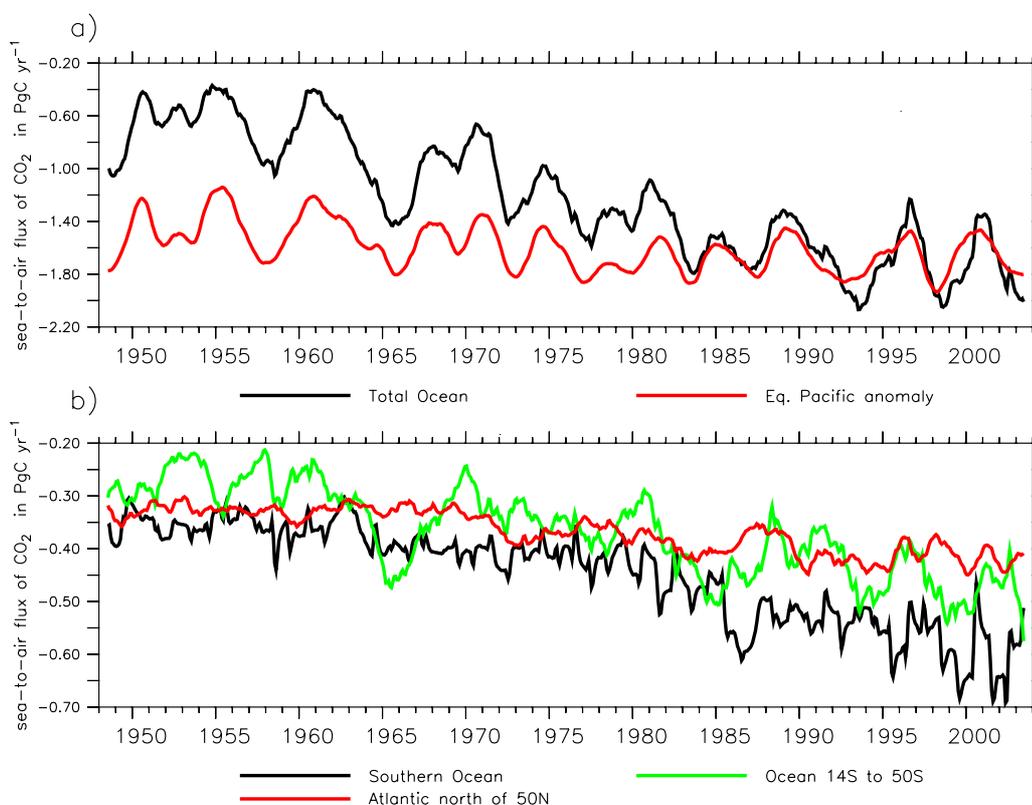
Fig. 6.5: *A) Global CO$_2$ flux in PgC yr^{-1}. B) CO$_2$ flux in various ocean regions in PgC yr^{-1}. Results from the run with anthropogenic CO$_2$ forcing (AR) smoothed with a 12 month running mean.*

ing this relationship yields a higher CO$_2$ flux of -2.3 PgC yr^{-1} for 1990-99. From the O$_2$ and N$_2$ fluxes simulated in this study, we calculate an inter-annual variability of the N$_2$/O$_2$ correction term of ± 0.20 PgC yr^{-1} $(2\,\sigma)$. Quite contrary to Bopp *et al.* (2002), we find an average net uptake of O$_2$ during 1980-89 and 1990-99. This would require a minor reduction (-0.07 PgC yr^{-1} for 1980-89 and -0.05 for 1990-99) of the oceanic flux estimates of Houghton *et al.* (2001).

6.5   Anthropogenic CO$_2$ Inventory

Anthropogenic CO$_2$ in the water-column is estimated analogous to the uptake of anthropogenic CO$_2$ is section 6.3. The inventory of anthropogenic carbon is computed as the difference between the dissolved inorganic carbon (DIC) inventory of the AR and the CR experiment. The regions where anthropogenic CO$_2$ is taken up by the ocean are not necessarily the regions

	Time	South ≤20 PgC yr^{-1}	Tropics PgC yr^{-1}	North ≥20 PgC yr^{-1}	Total PgC yr^{-1}
CR experiment	80-99	-0.11	1.18	-0.88	+0.18
AR experiment	80-89	-0.90	0.65	-1.26	-1.50
	92-96	-1.00	0.54	-1.32	-1.78
	96-99	-1.03	0.60	-1.29	-1.72
	95	-1.05	0.64	-1.34	-1.75
Rödenbeck *et al.* (2003)	80-89				-1.2±0.3
	90-96	-1.0±0.1	0.9±0.2	-1.6±0.1	-1.7±0.3
	96-99	-1.2±0.2	1.1±0.2	-1.7±0.1	-1.7±0.4
Gurney (2002)	92-96	-0.9±0.7	0.5±0.6	-1.1±0.4	-1.5±0.4
Takahashi *et al.* (2002)[a]	95	-1.51	0.90	-1.03	-1.64
Houghton *et al.* (2001)	80-89				-1.9±0.6
	90-99				-1.7±0.5

[a]Corrected fluxes from the web site at www.ldeo.columbia.edu/CO2/ using the Wanninkhof (1992) gas transfer coefficient.

Tab. 6.2: Sea-to-air flux of CO$_2$ into the northern hemisphere, tropics and the southern hemisphere in PgC yr^{-1}.

where the anthropogenic CO$_2$ is stored in the ocean, as shown in Figure 6.3. Storage of anthropogenic CO$_2$ is high in areas with a low buffer factor (or Revelle factor). The buffer factor depends on temperature, salinity and the actual state of the carbon chemistry. It is generally higher in cold waters of the high latitudes. Most of the anthropogenic carbon that is taken up in the high latitudes and the upwelling regions is transported to the subtropics, and accumulated mostly in the upper few hundred meters of the water-column. Deep entrainment of anthropogenic CO$_2$ mainly occurs in the deep water formation areas of the North Atlantic. The model also shows some deeper entrainment near the Weddell Sea in the Southern Ocean. In the equatorial regions and elsewhere in the high latitudes, the concentrations of anthropogenic CO$_2$ are low.

Various authors have used the $\Delta C^\star$ technique (Gruber *et al.*, 1996), to separate the small anthropogenic CO$_2$ signal from the large natural background of DIC. The method is based on the assumption that the stoichiometric ratios between carbon, nitrate and oxygen are constant and that the carbon cycle was in a steady state before the anthropogenic perturbation. With this postulate one can define a quasi-conservative tracer $\Delta C^\star$:

$$
\begin{aligned}
\Delta C^\star = \ & C - C_{eq}\left(S, T, Alk^0\right)|_{fCO_2=280\mu atm} \qquad (6.4)\\
& -r_{C:O_2}\left(O_2 - O_2^{sat}\right)\\
& -\frac{1}{2}\left(Alk - Alk^0 + r_{N:O_2}\left(O_2 - O_2^{sat}\right)\right),
\end{aligned}
$$

where C$_{eq}$ is the preindustrial equilibrium CO$_2$ concentration, S is the salin-

Atlantic Ocean	Year	South of Equator	North of Equator	Total
Lee (2003)	1994	18.5±3.9	28.4±4.7	46.9±8.6
This Study	1994	13.3	25.2	38.5
Pacific Ocean	Year	South of Equator	North of Equator	Total
Sabine *et al.* (2002)	1994	28.0	16.5	44.5±5.0
This Study	1994	27.0	17.5	44.5
Indian Ocean	Year	South of 35S	North of 35S	Total
Sabine *et al.* (1999)	1995	13.6±2.0	6.7±1.0	20.3±3.0
This Study	1995	13.6	7.4	21.0
Total Ocean	Year			
Lee & Sabine Sabine *et al.* (2004a)[a]				112±17
evaluated regions (fig.6.1)	1994			106±17
global estimate [b]	1994			118±19
GLODAP 1°gridded	1994	63.0	41.4	104.4
This Study	Year	South of Equator	North of Equator	Total
Regions analog to Sabine *et al.* (2004a)[a]		57.6	42.6	100.1
Total Ocean	1994	57.6	46.7	104.3
Total Ocean	1995	58.6	47.5	106.2

[a]Because the Arctic Ocean north of 65°N and the marginal basins have a limited data coverage they are excluded from the GLODAP analysis and Sabine *et al.* (2004a).

[b]Sabine *et al.* (2004a) estimate the inventory of the excluded regions to be about 12 PgC. In the AR experiment they only account for 4.2 PgC.

Tab. 6.3: Global anthropogenic carbon inventory. Compared are estimates from observations, evaluated with the "$\Delta C^\star$"technique (Gruber *et al.*, 1996), and model results from the AR experiment. All values are given in PgC.

ity, T is the temperature, Alk^0 is the preformed alkalinity, and O$_2$ and O$_2^{sat}$ are the in situ and saturation concentrations of oxygen. Preformed alkalinity is estimated from salinity, oxygen and phosphate (Broecker and Peng, 1982). If the assumptions are right, the variability of $\Delta C^\star$ reflects only the ocean uptake of anthropogenic CO$_2$ and the CO$_2$ disequilibrium at the time the water parcel lost contact with the atmosphere. Lee (2003), Sabine *et al.* (2002) and Sabine *et al.* (1999) use this technique to estimate an inventory of anthropogenic CO$_2$ for the Atlantic, Pacific and the Indian Ocean. Based on the "$\Delta C^\star$"technique and the data compilation of the GLODAP project Sabine *et al.* (2004a) present an estimate of the anthropogenic CO$_2$ inventory for the global ocean between 60°N and 80°S (see figure 6.1). In table 6.5 their results are compared to results of the AR experiment.

The modeled global spatial distribution and concentrations of anthro-

pogenic DIC are in good agreement with the estimates by the ΔC* technique. In the Pacific and the Indian Ocean the simulated inventory almost matches the calculations of Sabine *et al.* (2002) and Sabine *et al.* (1999), however our estimate for the Atlantic is about 25% lower than the calculation by Lee (2003). Also the 1°x1°gridded Atlantic estimate of the GLODAP project is in line with the model results (table 6.7). The difference may be related to the different approaches of Sabine *et al.* (2002),Sabine *et al.* (1999) and Lee (2003) to estimate the air-sea CO$_2$ disequilibrium term for shallow surfaces.

6.6   Southern Hemisphere

The global figure of anthropogenic CO$_2$ uptake in figure 6.3 shows the highest rates of anthropogenic CO$_2$ uptake in the region from 50°S to 70°S. Variability and trend of the Southern Ocean CO$_2$ flux in the CR experiment are discussed in detail in section 5.4. An important factor for the uptake and the air-sea CO$_2$ fluxes is the mixed layer depth, that is related to the buoyancy fluxes and the wind stress. The wind stress, modeled mixed layer depth, and the CO$_2$ fluxes show a high correlation with the Antarctic Oscillation (Thompson and Solomon, 2002, AAO, figure 5.9). Increased mixing leads to an increased CO$_2$ flux out of the ocean in the CR experiment, as deeper waters with higher DIC are mixed to the surface. The uptake of anthropogenic CO$_2$ is also increasing, because anthropogenic CO$_2$ penetrates faster into the deeper layers due to enhanced ventilation. Recent estimates from atmospheric inversions (Roy *et al.*, 2003; Rödenbeck *et al.*, 2003; Gurney, 2002) show a flux of about -1 PgC yr^{-1} for the southern hemisphere, but vary considerably in the partitioning between the Southern Ocean and the mid latitudes. Numbers are listed in table 6.6. The model shows the highest influx south of 50°S (Figure 6.3, which is in agreement with Gurney (2002) but in disagreement with Rödenbeck *et al.* (2003).

Estimates based on interpolated pCO$_2$ measurements show a high CO$_2$ flux into the ocean in the southern hemisphere (Takahashi *et al.*, 2002). Metzl *et al.* (1999) extrapolate a flux of about -1 PgC yr^{-1} for the sub-Antarctic zone from about 40°S-50°S alone. Estimates from atmospheric inversions and findings from this study indicate a smaller CO$_2$ influx. The remote Southern Ocean has a sparse data coverage, particular in winter, so it is necessary to extrapolate the regional estimates over the seasonal cycle, which may explain the discrepancies. The model has a strong seasonal cycle with a large CO$_2$ influx in December and January and outgassing from February to May. The CO$_2$ fluxes calculated from the climatology from Takahashi *et al.* (2002) show a weak seasonal cycle with a minimum influx of CO$_2$ in June/July. Atmospheric inversions by Roy *et al.* (2003) and Gurney (2004) indicate a stronger cycle, Roy *et al.* (2003) even find a weak outgassing for February to May, but their seasonal cycle is less pronounced than predicted

	Year	50°S-90°S	14°S-50°S	Total
Roy *et al.* (2003)	91-97	-0.3	-0.7	-1.0
Rödenbeck *et al.* (2003)	90-99	0.0±0.1	-1.0±4.7	-1.0
Gurney (2002)	92-96	-0.5	-0.4	-0.9
Gurney (2004)[a]	92-96	-0.55±0.33	+0.07±0.54	-0.48
Takahashi *et al.* (2002)	1995	-0.35	-1.16	-1.51
This Study	90-99	-0.56	-0.45	-1.1

[a] The main difference to Gurney (2002) is the removal of the Darwin CO_2 observing station from the analysis.

Tab. 6.4: Sea-to-air CO_2 fluxes in PgC yr^{-1} partitioned between the Southern Ocean and the mid-latitudes of the southern hemisphere. The total anthropogenic carbon inventories are given in PgC. Compared are estimates from observations, evaluated with the $\Delta C^\star$ technique (Gruber *et al.*, 1996), taken from the GLODAP project (Key *et al.*, 2004) and model results from the AR experiment.

	14°S-50°S	50°S-90°S	SO Indian	SO Atlantic	SO Pacific
storage (80-89)	6.1	1.9	0.5	0.5	0.9
uptake (80-89)	4.9	3.7	1.1	0.8	1.8
storage (90-99)	7.3	2.1	0.6	0.6	1.0
uptake (90-99)	5.8	4.6	1.5	1.1	2.0
Total Inventory					
Model (1994)	36.6	11.0	2.6	3.0	5.4
GLODAP (1994)	42.0	10.3	1.9	2.8	6.2

Tab. 6.5: Uptake and storage of anthropogenic CO_2 in the Southern Ocean and the mid-latitudes of the southern hemisphere in PgC.

by the model.

The uptake rates of anthropogenic carbon for 1980-89 and for 1990-99 in the Southern Ocean are almost comparable to the uptake rates in the deep water formation areas in the North Atlantic. The model shows the highest uptake rates in the Southern Ocean from 50°S to 70°S (figure 6.3), while the highest storage occurs out of the Southern Ocean north of 50°S (figure 6.3). Half of the anthropogenic CO_2 taken up by the Southern Ocean is transported northward into the subtropical convergence (table 6.6), which is supported by the study of Caldeira and Duffy (2000).

The estimated distribution of anthropogenic CO_2 by Sabine *et al.* (2004a), Sabine *et al.* (2002), Sabine *et al.* (1999) and Lee (2003) are generally in good agreement with the model. These studies indicate relatively little storage of anthropogenic CO_2 in the Southern Ocean and high storage in the subtropical convergence. The model estimates compare very well with the inventories for the Pacific and the Indian Ocean given by Sabine *et al.*

(2002) and Sabine *et al.* (1999). In the Atlantic, model estimates are lower than results from Lee (2003). An interesting exception is the Weddell Sea between 60°E and 20°W, where deep convection in coherence with the formation of sea ice is entraining anthropogenic CO$_2$ into the deep Southern Ocean (figure 6.3). This study predicts about 1.3 Pg anthropogenic CO$_2$ in the Atlantic from 70°S to 60°S by 1995, which is 1 PgC more than the estimate by Lee (2003). The model inventory in the Southern Ocean sector of the Atlantic is also higher than the GLODAP estimates (table 6.6).

6.7   North Atlantic, Greenland, Iceland, Norwegian & Labrador Seas

It is generally accepted that the North Atlantic is a strong sink for CO$_2$. The modeled CO$_2$ flux and variability of the North Atlantic north of 50°N is -0.31±0.04 PgC yr^{-1} in the CR and -0.41±0.05 for 1990-99 in the AR experiment.

The model produces a deep penetration of anthropogenic CO$_2$ in the high northern latitudes of the Atlantic. This is in agreement with $\Delta C^\star$ technique estimates by Lee (2003) and Gruber (1998) and CFC data estimates from McNeil *et al.* (2003). Most important are the deep water formation areas north of 50°N, the Labrador, Greenland, Iceland and Norwegian (GIN) Seas. The high inventories of anthropogenic CO$_2$ in the high latitudes of the North Atlantic reach deeper than anywhere else in the world. However, Völker *et al.* (2002) raised the question, if this implies that the flux of carbon from the atmosphere into the North Atlantic has increased over its preindustrial value. Uptake and storage of anthropogenic CO$_2$ in the North Atlantic are summarized in table 6.7. Similar to the southern hemisphere, the accumulation of anthropogenic CO$_2$ in the mid-latitudes is higher than the oceanic uptake of anthropogenic CO$_2$ by air-sea gas exchange. The Arctic Ocean is fed by waters from the Bering Strait and the West Spitsbergen Current that are well equilibrated with the atmospheric CO$_2$ concentrations. The storage in the Arctic Ocean is estimated to be four times higher than the uptake by the air-sea gas exchange. In areas of North Atlantic Deep Water formation, e.g. GIN and Labrador Seas, intense surface cooling and deep winter convection carry the anthropogenic CO$_2$ signal down to the bottom of the ocean. Accumulation of anthropogenic CO$_2$ in the GIN sea is lower than the uptake of anthropogenic CO$_2$ by air-sea gas exchange. Most of the water masses transported into the GIN sea originate in the North Atlantic Current and are not fully equilibrated with the atmospheric CO$_2$ concentrations, and a significant fraction of the anthropogenic CO$_2$ taken up by air-sea gas exchange is transported out of the GIN sea with the East Greenland Current, the Denmark Strait and the Faroe-Shetland overflow. In the Labrador Sea and the remaining part of the North Atlantic from 70°N-50°N (excluding

	50°N-14°N	70°N-50°N [a]	GIN sea	Labrador	Arctic
storage (80-89)	2.07	0.57	0.24	0.15	0.30
uptake (80-89)	1.06	0.46	0.31	0.12	0.07
storage (90-99)	2.52	0.60	0.17	0.16	0.41
uptake (90-99)	1.17	0.59	0.35	0.14	0.10
Total Inventory	50°N-14°N	65°N-50°N [a]	GIN sea	Labrador	Arctic
Model (1994)	14.3	4.4	1.5	0.9	2.6
GLODAP (1994)	16.0	3.4			

[a]Excluding the GIN and Labrador seas.

Tab. 6.6: Uptake and storage of anthropogenic CO_2 in the North Atlantic and the northern high-latitudes in PgC.

the GIN and Labrador seas) the in- and out-flows of anthropogenic CO_2 are roughly in balance. Highest rates of anthropogenic CO_2 uptake are simulated in deep convection areas near Greenland. This uptake is reduced by a rising buffer factor, causing only a small increase from 1980-89 to 1990-99 (table 6.7).
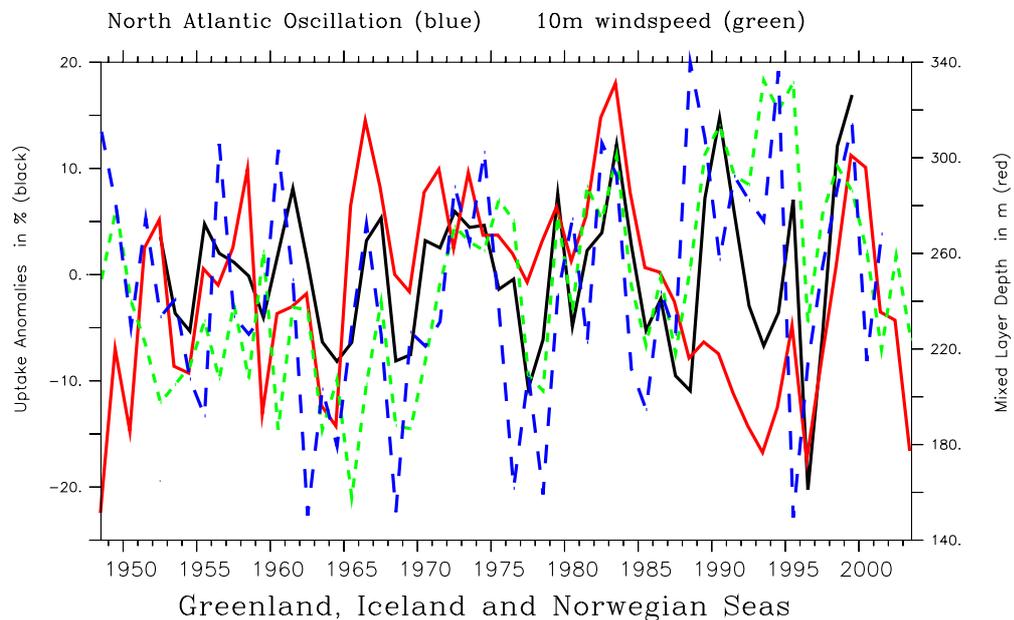

Fig. 6.6: *Correlation of the wintertime North Atlantic Oscillation (NAO) with yearly averages for the Greenland, Iceland and Norwegian Seas. In blue is the NAO Index and in green is the 10 m wind speed from the NCEP reanalysis. Shown are the uptake anomalies of anthropogenic CO_2 (black, AR experiment) and the average mixed layer depth (red).*

North Atlantic Oscillation (blue)   10m windspeed (green)
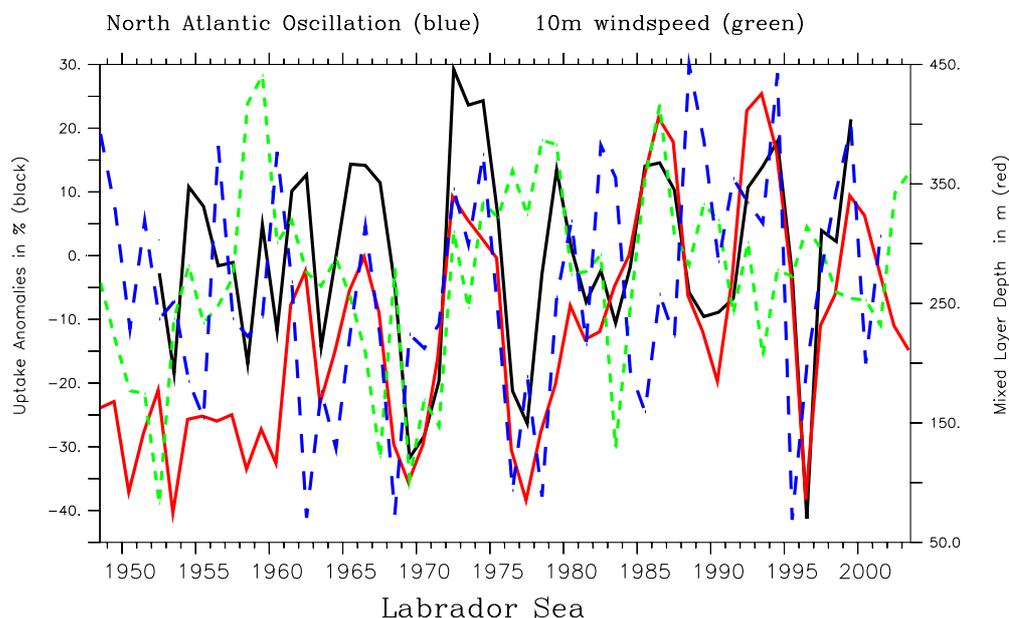

Fig. 6.7: *Correlation of the wintertime North Atlantic Oscillation (NAO) with yearly averages for the Labrador Sea. In blue is the NAO Index and in green is the 10 m wind speed from the NCEP reanalysis. Shown are the uptake anomalies of anthropogenic CO$_2$ (black, AR experiment) and the average mixed layer depth (red).*

Section 5.5.2 deals in detail with the CO$_2$ flux variability and correlation patterns with the to the North Atlantic Oscillation (Hurrell *et al.*, 2003; Hurrell, 1995, NAO). The CO$_2$ flux in the North Atlantic is only weakly correlated to the NAO Index. This results from the competing influences of the physical and chemical drivers. Interannual variations in the uptake of anthropogenic CO$_2$ is mostly controlled by changes in the mixed layer depth (MLD). The simulated oceanic uptake of anthropogenic CO$_2$ north of 50°N is correlated with the winter NAO Index; between 40°N and 30°N it is anti-correlation with the winter NAO index.

Uptake of anthropogenic CO$_2$ in the Labrador Sea is tightly connected to the MLD, which itself is correlated to the NAO index, but also responds to the wind speed (figure 6.7). The 10 m wind speed in the Labrador Sea has almost no correlation with the NAO index. In the GIN Sea, the MLD does not correlate to the NAO index, but the 10m wind speed does. Like in the Labrador Sea, the uptake depends on the wind and the MLD (figure 6.6).

6.8 North-South Gradient
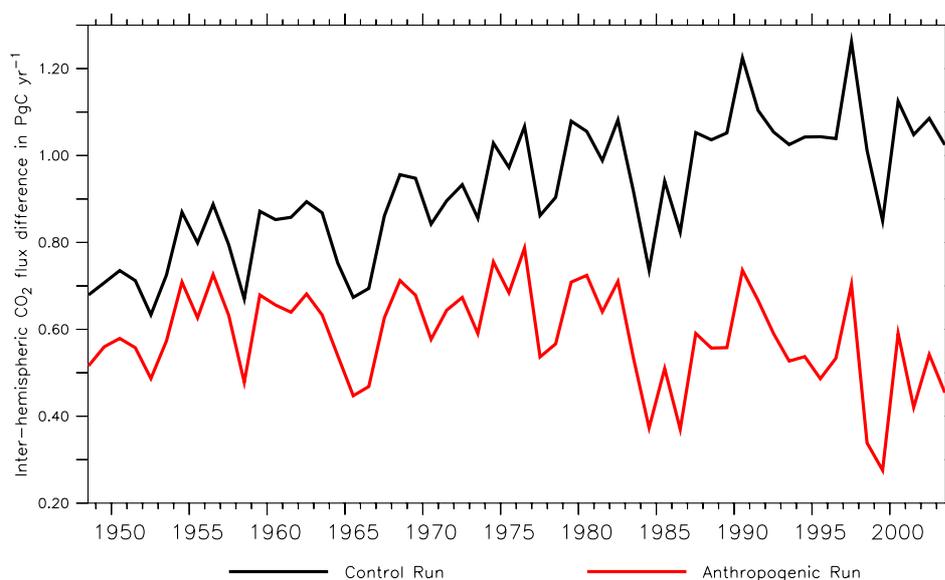
Fig. 6.8: *Yearly averages of CO_2 flux difference between the northern and the southern hemisphere in the Control Run (CR) experiment and the experiment with anthropogenic CO_2 forcing.*

Another much debated aspect of the global CO_2 fluxes is the north-south asymmetry. Keeling et al. [1989] extrapolated changes in the difference between the atmospheric CO_2 concentrations at stations Mauna Loa and South Pole. They calculated a preindustrial atmospheric north-south gradient of 0.82 ppm and concluded a preindustrial north-south transport of 1 PgC yr^{-1} in the ocean. We find a pre-industrial, cross-equatorial transport of about 0.75 PgC yr^{-1} in the 1950s and 1960s. Due to increased outgassing in the Southern Ocean, the inter-hemispheric flux difference rises to 1.06 PgC yr^{-1} in the 1990s (figure 6.8). The cross-tropical transport is about 0.26 PgC yr^{-1} smaller on average. The Ocean Carbon-Cycle Model Intercomparison Project (OCMIP) has investigated this pre-industrial transport with a variety of ocean carbon cycle models. None of the OCMIP-1 models produced a southward transport of more than 0.1 PgC yr^{-1} (Sarmiento *et al.*, 2000). OCMIP-2 found a larger range of southward transport, but, with one exception, still below 0.35 PgC yr^{-1} (Orr, 2001). Aumont *et al.* (2001) added a riverine carbon input to the IPSL model, and found an increase of the simulated southward carbon transport by 0.1-0.3 PgC yr^{-1} . A riverine carbon input in not considered in this study. The high pre-industrial north-south

transport in this model is due to the iron limitation that is strongly affecting the the biological production in the Southern Ocean. Without the iron limitation the otherwise identical model with identical surface forcing does not produce a considerable north-south carbon transport. The variability of the inter-hemispheric flux difference with the trend removed is 0.2 PgC yr^{-1} ($2\,\sigma$) and almost identical in the anthropogenic and the control run.

With the uptake of anthropogenic carbon rising faster in the southern hemisphere the inter-hemispheric flux difference is decreasing. The relationship between the decrease and the atmospheric CO$_2$ concentration is almost linear (-0.008 PgC yr^{-1} per ppm). But even so the inter-hemispheric flux difference is getting smaller, in contrast to Takahashi *et al.* (2002) we still find a higher CO$_2$ uptake in the northern hemisphere in the 1990s. Rödenbeck *et al.* (2003) and the TransCom3 inversion intercomparison study (Gurney, 2002) also conclude a larger oceanic uptake in the northern hemisphere. In addition to the higher uptake in the southern hemisphere the model shows an average flow of 0.15 PgC yr^{-1} of anthropogenic CO$_2$ into the North Atlantic for the 1990s. That is because the North Atlantic deep water that feeds the Deep Western Boundary Current flowing southward still contains relatively low anthropogenic CO$_2$ compared to the surface waters that flow into the North Atlantic.

7. SENSITIVITY EXPERIMENTS

In addition to the standard experiment, two sensitivity experiments were performed during this thesis. First, the sensitivity of the sea-air CO_2 flux variability to the iron limitation was tested in an identical setup, but without the iron limitation. Second, the sensitivity of the sea-air CO_2 flux to the gas exchange was tested in an experiment with a constant gas exchange coefficient. Global results for all sensitivity studies are shown in figure 7.1. Even so the changes to the system are considerable, the global variability only varies by about $\pm 20\%$.
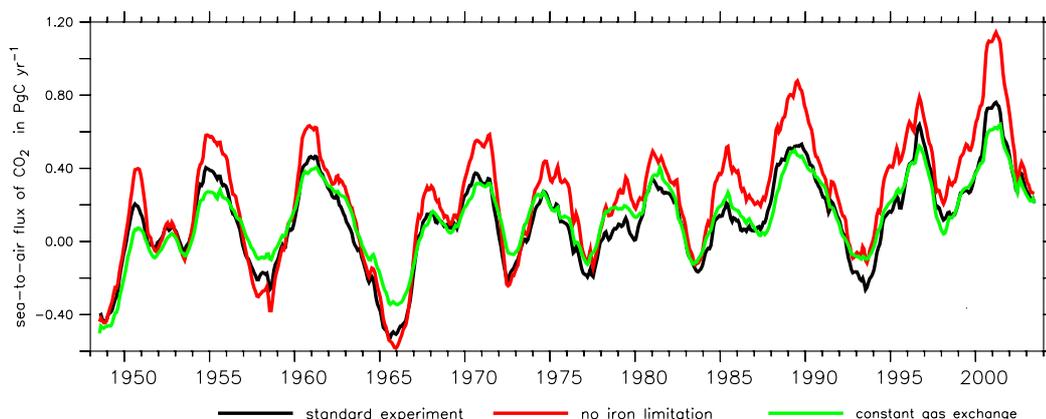
Fig. 7.1: *Comparison of global CO_2 fluxes from the standard experiment and the sensitivity studies without iron-limitation and with constant gas exchange velocity. All results are monthly smoothed with a 12 month running mean.*

7.1 Experiment without Iron Limitation

Observations show "lower than expected" chlorophyll concentrations in the Southern Ocean, the eastern and central equatorial and the western Pacific, now commonly referred to as "High Nutrient Low Chlorophyll" ("HNLC")

regions. Martin and Fitzwater (1988) proposed that phytoplankton growth in this areas is limited in particular by the micronutrient iron. The hypothesis is supported by iron enrichment experiments in the Southern Ocean (Boyd and et al., 2000, SOIREE) and in the Equatorial Pacific (Coale *et al.*, 1996, IRONEX II). In the standard version of HAMOCC5 iron is taken up by marine organisms with a fixed ratio to phosphate ($R_{Fe:P}$). Dissolved,biologically available iron is deposited by dust on the surface. The dust fields used in the main experiment are taken from an model simulation by Timmreck and Schulz (2004). In order to test the sensitivity of the CO_2 fluxes to the iron limitation, the experiment is repeated without iron limitation. Otherwise the setup is identical. Globally, the interannual CO_2 flux variability only changes from ± 0.49 PgC yr^{-1} to ± 0.64 PgC yr^{-1}, but there are strong changes in the flux distribution.
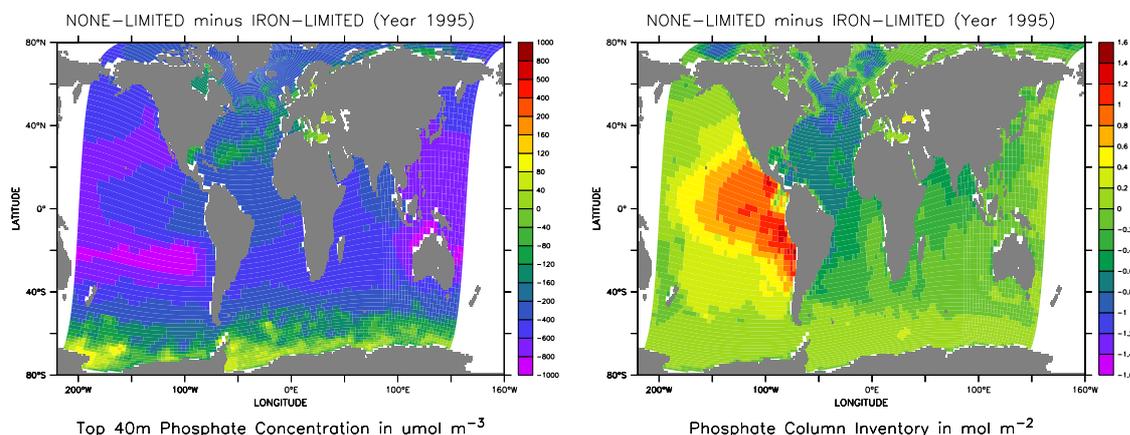

Fig. 7.2: *Comparison of the standard model to a setup without iron limitation. Shown is the non-limited distribution minus the iron-limited distribution of phosphate in the model year 1995. Left:Surface concentration im $\mu mol m^{-3}$. Right: total CO_2 column inventory in $mol m^{-2}$.*

Phosphate is a representative for nutrient and DIC distributions, because the gradients are large and it is not exchanged with the atmosphere. Figure 7.2 is a difference plot of the phosphate distribution between the non-limited and the iron-limited simulation. The column inventory shows a shift in the distribution towards the Pacific, reflecting the large scale "conveyor belt"structure of the global current system. As the deep ocean water masses travel with the "conveyor belt"from the Atlantic via the Southern Ocean in to the North Pacific they accumulate the nutrients exported from the surface. If the biological export production is larger, with no limitation by iron availability, the deep waters accumulate more nutrients and the gradient becomes stronger. This goes hand in hand with generally lower surface concentrations. But there is one exception in the Southern Ocean

(figure 7.2, left side). South of about 60°S the surface concentrations are actually higher in the system without iron limitation. This is somewhat surprising as the Southern Ocean is the area where one would expect the largest limitation of the biological production. Reason for this "paradox"is the deep winter mixing in the area and the higher nutrient concentration in the deep Southern Ocean. Of course, the short spring and summer bloom is larger in the system without iron limitation, but on the annual average the concentration in the top 40 m is higher.
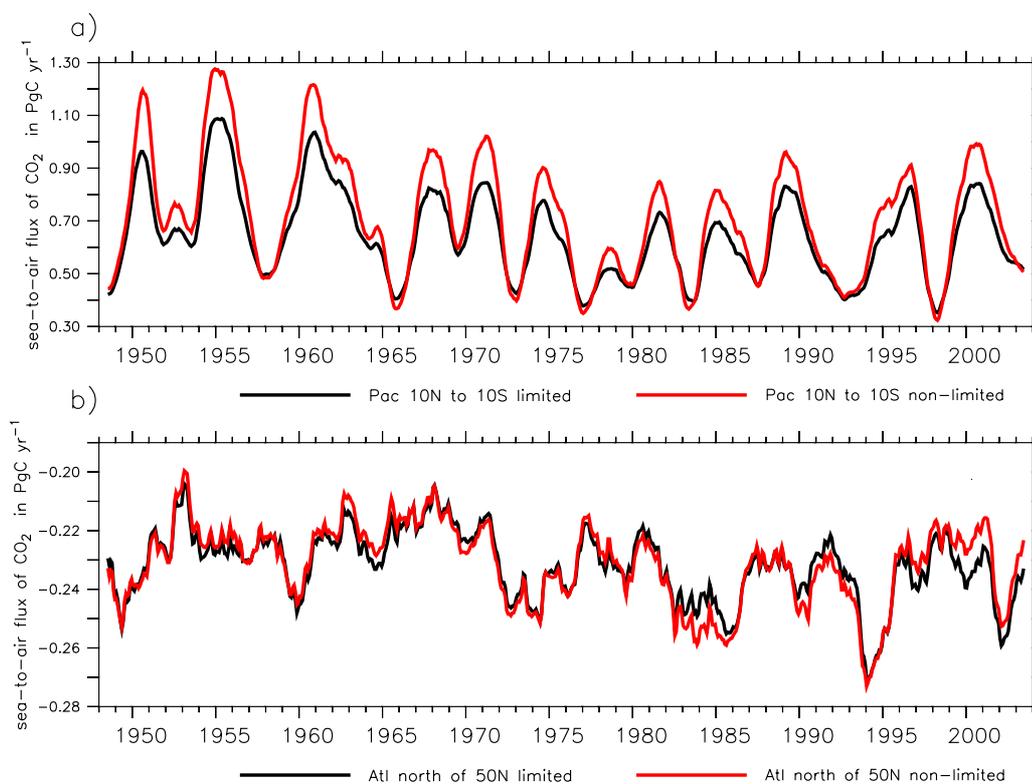

Fig. 7.3: *Comparison of the standard model to a setup without iron limitation. Shown is the CO_2 flux in the Equatorial Pacific from $10°N$ to $10°S$ and the CO_2 flux in the North Atlantic north of $50°N$. All results are monthly values smoothed with a 12 month running mean.*

The comparison of CO_2 fluxes in figure 7.3 and 7.4 reflects differences in the DIC distribution, which is similar to the phosphate distribution. Without the limitation almost all nutrients in the subtropical gyres of the Pacific and most of the nutrients in the southern hemisphere between 14°S and 50°S are utilized (figure 7.2, left side). As a result the net flux, that is almost neutral in the experiment with iron limitation, is directed into the ocean.
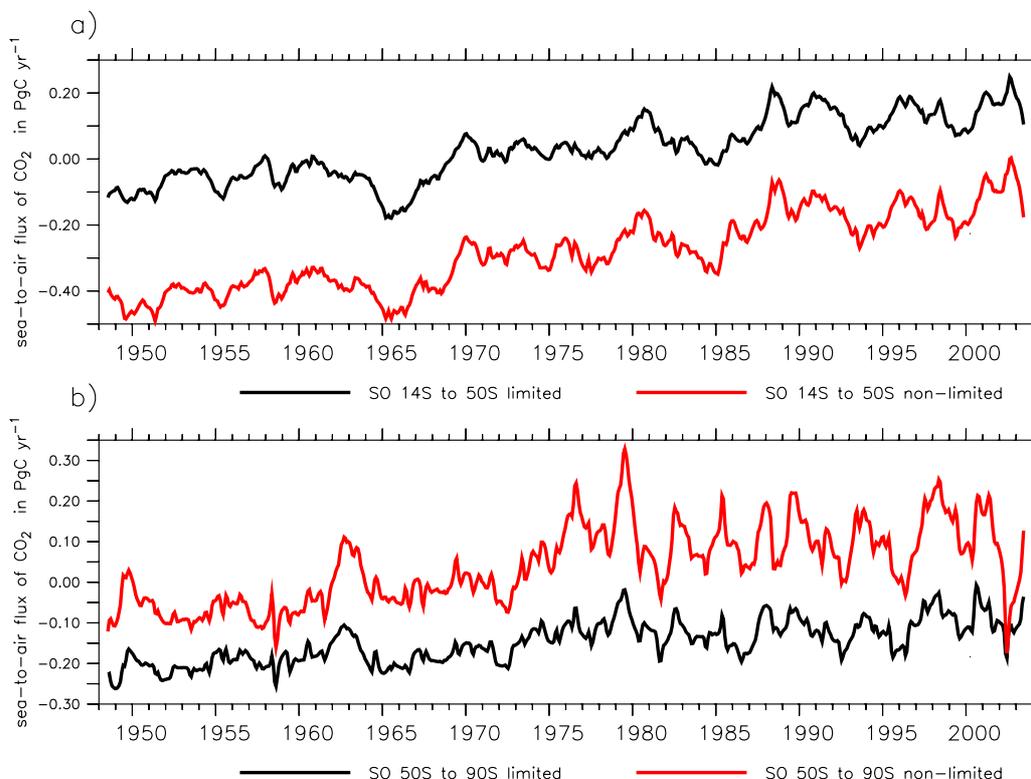
Fig. 7.4: *Comparison of the standard model to a setup without iron limitation. Shown is the CO_2 flux in the southern hemisphere between $14°S$ and $50°S$ and the CO_2 flux in the Southern Ocean south of $50°S$. All results are monthly values smoothed with a 12 month running mean.*

The net flux in the Southern Ocean south of 50 °S, that is negative in the experiment with iron limitation, is positive without the iron limitation. The total net flux in the southern hemisphere is only 0.1 PgC yr^{-1} lower without than with iron limitation, but the distribution is completely different. Strong mixing events bring the higher DIC concentrations from the deep ocean to the surface. The interannual CO_2 flux variability in the Southern Ocean south of 50 °S is twice as large without iron limitation (± 0.2 PgC yr^{-1}) as in the standard setup(± 0.1 PgC yr^{-1}).

Surface concentrations of phosphate in the North Atlantic are only slightly lower without the iron limitation. Due to the Saharan dust deposition the North Atlantic is not iron limited in the model and the lower surface concentrations reflect the large scale shift in the nutrient distribution from the North Atlantic towards the Pacific (figure 7.2, right side). Figure 7.3 shows almost no difference in the net sea-air flux of CO_2 for the North Atlantic

north of 50°N.

The phosphate concentration underneath the Equatorial Pacific depends on the transport in intermediate and deep waters into the Pacific and on the remineralization of organic material exported from the surface. An almost complete utilization of all upwelled nutrients within the equatorial region ultimately leads to a higher export and more remineralization of organic material and hence to a higher nutrient and DIC concentration underneath the Equator. Strong upwelling events, associated with e.g. La Niña events, bring the accumulated DIC to the surface, causing a strong outgassing of CO_2 from the ocean to the atmosphere. Second, the complete utilization of nutrients is resulting in very low oceanic pCO_2 during times of weak upwelling, associated with e.g. an El Niño event. This model shows a 35% decrease in the CO_2 flux variability in the equatorial Pacific, due to the limitation by iron. Obata and Kitamura (2003) suggested, that such a limitation would lower the biological production and the biological CO_2 uptake at strong upwelling events (La Niña) and therefore increase the CO_2 flux variability. In this model, the fairly small influence of the biological production on the variability of DIC is related to the limitation by iron, but the effect on the CO_2 flux variability is of second order.

7.2 Experiment with Constant Gas Exchange

In models, the CO_2 flux is computed from the CO_2 partial pressure difference between the ocean and the atmosphere (ΔpCO_2) using a gas exchange coefficient. In the standard simulation this exchange coefficient is computed with the square of the 10 m wind speed analogous to Wanninkhof (1992) (section 2.3.4). Beside the formulation from Wanninkhof (1992), Nightingale *et al.* (2000) and Liss and Merlivat (1986) have proposed alternative parameterizations to calculate the gas exchange coefficient. In order to test the sensitivity of the CO_2 fluxes to the gas exchange coefficient, the experiment is repeated with a constant gas exchange coefficient (piston velocity 2.8 m/d). Otherwise, the setup is identical.

If the CO_2 fluxes are derived from a ΔpCO_2 climatology, the flux is a linear function of the gas exchange coefficient (k).

$$Flux = \Delta pCO_2 * k \qquad (7.1)$$

This is the case for the fluxes from Takahashi *et al.* (2002), that are often used as *a priori* input in an inverse model approach (Gurney, 2002) or for carbon cycle model comparison (McKinley *et al.*, 2004). In a carbon cycle model and in the real ocean, ΔpCO_2 is also function of the CO_2 flux. The flux is mostly generated by inner oceanic processes, i.e. the import of DIC-enriched water in regions of upwelling. The details of the formulation of the
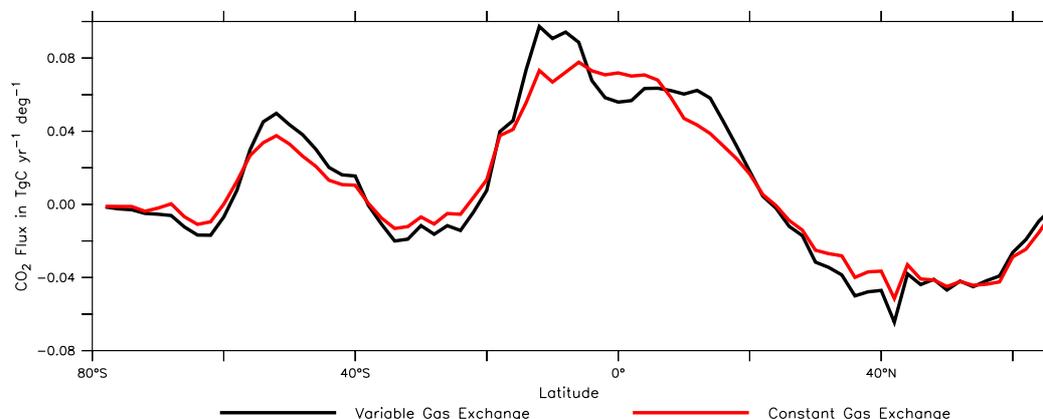
Fig. 7.5: *Comparison of the standard model to a setup with constant gas exchange coefficient. Shown is the annual sum of CO_2 fluxes from North to South along the Pacific ocean for the simulation year 1998 in units of $TgCyr^{-1}deg^{-1}$*

gas exchange coefficient determine just the horizontal pattern of ΔpCO_2 and the relationship should be formulated as:

$$\Delta pCO_2 = \frac{Flux}{k} \tag{7.2}$$

As an example, figure 7.5 shows a section of the summed up CO_2 fluxes over the Pacific ocean for the simulation year 1998. The standard model with a wind speed dependent gas exchange coefficient shows much more structure, but the total CO_2 flux integral is relatively insensitive to the gas exchange parameterization.

A global map of pCO_2 differences between the standard experiment and sensitivity study with fix gas exchange is shown in figure 7.6. In most areas the differences are minor. As discussed above in upwelling region one can see a movement of higher pCO_2 to neighboring ares. The large differences along the coasts of Greenland and Newfoundland are discussed in detail in section 5.6. There, biological production lowers the ΔpCO_2 in summer and sea-ice stops the equilibrate with the atmosphere in winter. Higher gas exchange in the summer month by the fix gas exchange coefficient changes the ΔpCO_2 considerably.

The total interannual CO_2 flux variability is only about 16% lower than in the standard experiment (figure 7.1). The variability in the Equatorial Pacific between 10°N and 10°S (figure 7.7) is lower when the variability is high during the first part of the simulation (1948 to 1977, compare section 5.3.1). But, as discussed above, it is mostly the pattern that changes and
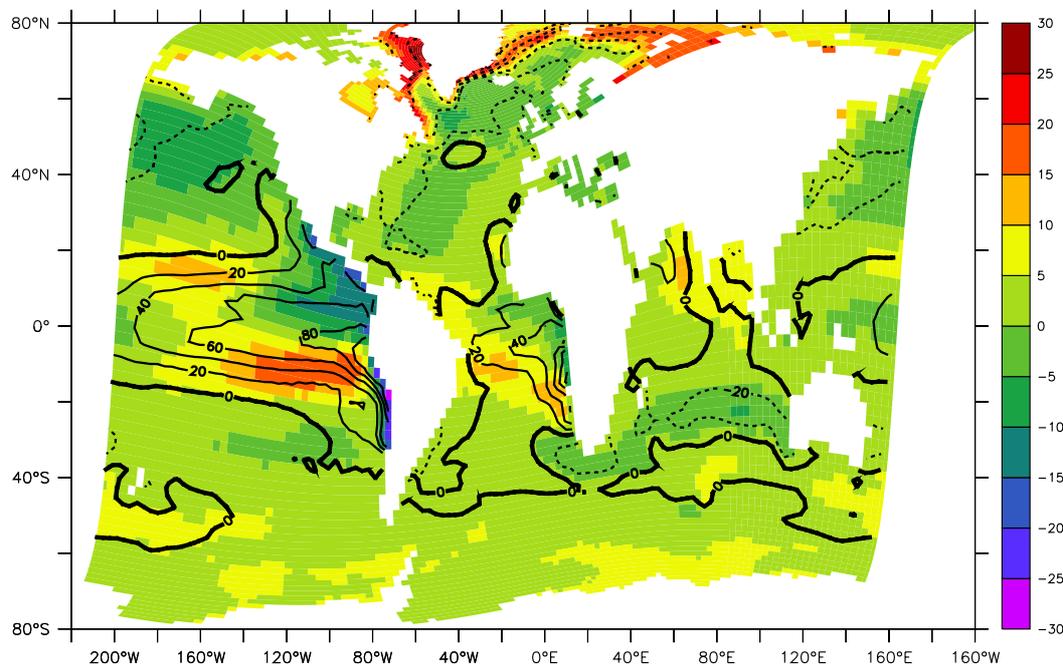
pCO$_2$ Difference: Constant Minus Variable Gas Exchange

Fig. 7.6: *Difference of yearly average pCO$_2$ in ice-free regions between the standard experiment with variable gas exchange (Wanninkhof, 1992) and a sensitivity study with fix gas exchange. The overlayed contour lines show the average ΔpCO_2 in ice-free regions of the standard experiment.*

the outgassing is stronger north and south of the Equatorial Pacific. For this reason the fluxes in the southern hemisphere between 14°S and 50°S are generally higher during the first part of the analysis. Apart from that, the sensitivity study shows, consistent with the analysis in section 5.4, that the variability in the Southern Ocean is mostly driven by ocean dynamics.

The situation is different in areas in the North Atlantic, which are partly covered by sea-ice in winter. Here the variability does depend to the gas exchange coefficient, but as discussed in section 5.5, the total variance integrated over the North Atlantic is not important for the global interannual variability. Also consistent with the analysis in section 5.5 the sensitivity study shows, that the trend towards a higher influx in the standard experiment is also driven by the increasing gas exchange coefficient.
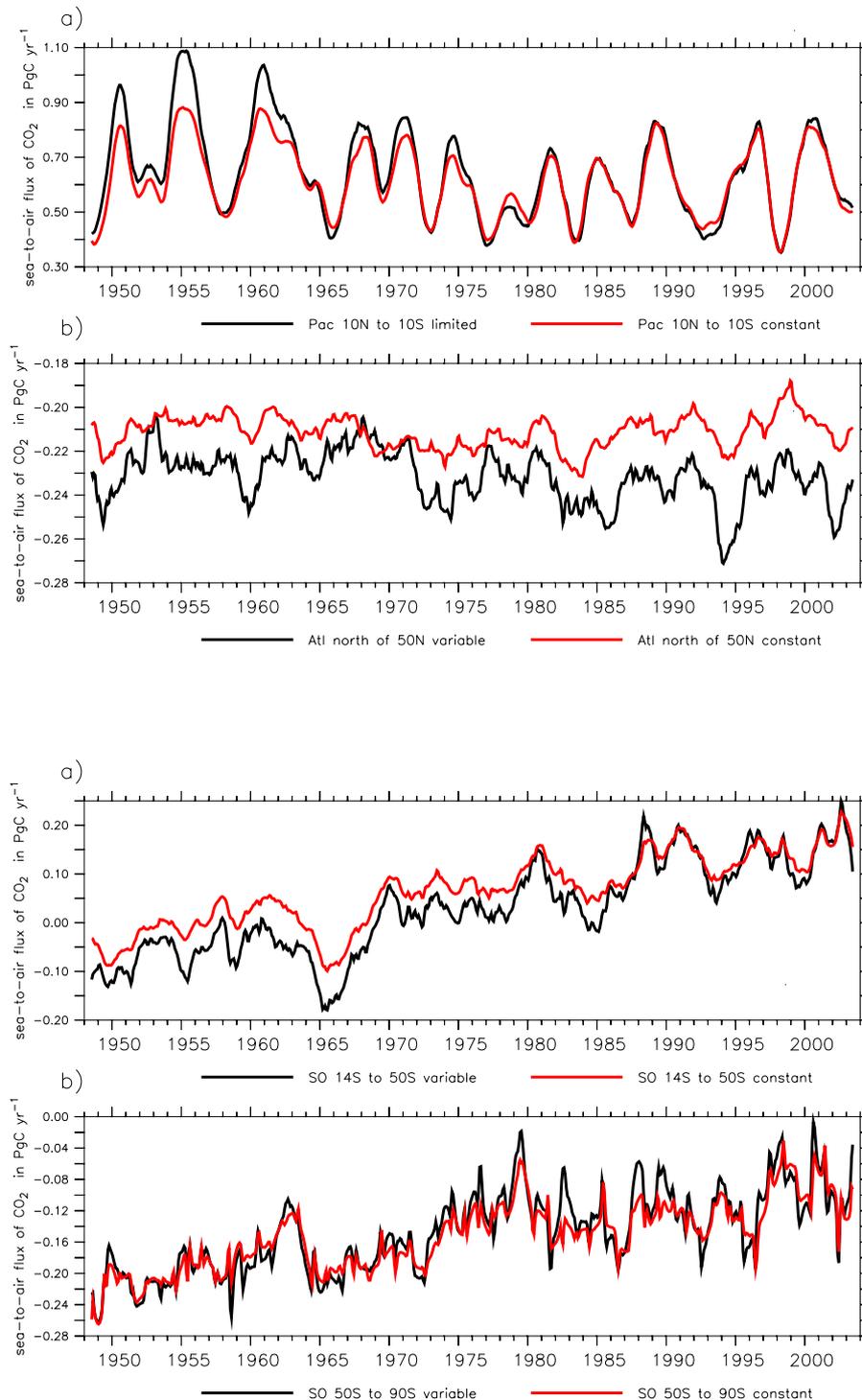
Fig. 7.7: *Comparison of the standard model to a setup with constant gas exchange coefficient. Upper: CO_2 flux in the southern hemisphere between $14°S$ and $50°S$ and the CO_2 flux in the Southern Ocean south of $50°S$. Lower: CO_2 flux in the Equatorial Pacific from $10°N$ to $10°S$ and the CO_2 flux in the North Atlantic north of $50°N$. All results are monthly values smoothed with a 12 month running mean.*

8. DISCUSSION

Decadal and interannual variability of sea-air CO_2 fluxes is investigated with a fully prognostic biogeochemical carbon cycle model (HAMOCC5) coupled on-line to a global ocean general circulation model (MPI-OM). The model is forced with surface fluxes computed from the NCEP/NCAR reanalysis for the period 1948 to 2003. The natural variability and the trends are analyzed in a control run with preindustrial atmospheric CO_2 concentrations. In addition, the response of the system to anthropogenic atmospheric CO_2 concentrations is tested. A series of sensitivity experiments are conducted in order to constrain the model dependency of the results.

The total interannual variability of the model is $\pm$ 0.50 PgC yr^{-1} $(2\,\sigma)$. This is within the range of previous ocean model studies (Le Quéré *et al.*, 2000; Obata and Kitamura, 2003; McKinley *et al.*, 2004) and recent atmospheric inversions (Rödenbeck *et al.*, 2003). The CO_2 flux is -1.49 PgC yr^{-1} for 1980-1989 and -1.74 PgC yr^{-1} for 1990-1999. The simulated mean fluxes agree well with flux estimates from atmospheric inversions (Rödenbeck *et al.*, 2003; Gurney, 2002, table 6.4)

Specific regions of the ocean have profoundly different biochemical characteristics, which determine the CO_2 flux variance. The experiments yield the following results:

1. Equatorial Pacific

   In agreement with other global ocean carbon cycle model studies (Le Quéré *et al.*, 2000; Obata and Kitamura, 2003; McKinley *et al.*, 2004), the equatorial Pacific in this study also dominates the global CO_2 flux variability. In the control run (CR) experiment, the equatorial Pacific from 10°N to 10°S accounts for ± 0.33 PgC yr^{-1} $(2\,\sigma)$, which is about 65% of the global interannual CO_2 flux variability. In addition to the interannual variability, the Pacific climate also undergoes decadal-scale shifts which affect the sea surface temperature and the trade winds (Trenberth and Hurrell, 1994). In agreement with observational evidence (McPhaden and Zhang, 2002), the model simulates a slowdown of the overturning circulation of about 25% at the regime shift in 1975-1977. The simulated wind-driven overturning of both equatorial cells decreases from 100±11 Sv to 77±5 Sv and the in-

terannual flux variability changes from ± 0.33 PgC yr^{-1} (1948 to 1976) to ± 0.27 PgC yr^{-1} (1977 to 2003). The shift can also be seen in the Pacific Decadal Oscillation Index (Mantua *et al.*, 1993, figure 5.4).

2. Southern Ocean

The Southern Ocean accounts for over 20% of the global interannual CO_2 flux variability. With ± 0.1 PgC yr^{-1} (the trend subtracted), the region from 40°S to 60°S has the highest variability and also shows a trend of 0.005 PgC yr^{-1} per year in the CR experiment. The reason for this trend is the wind stress over the Southern Ocean, that increases over the full 56 year period of the reanalysis. Directly related to the buoyancy fluxes and the wind stress is the mixed layer depth, which is an important factor determining the air-sea CO_2 flux. Therefore the wind stress, the modeled mixed layer depth, and the CO_2 fluxes are strongly coupled, and they all correlate with the Antarctic Oscillation (Thompson and Solomon, 2002, AAO, or Southern Annual Mode). In the experiment with anthropogenic CO_2 (AR) the uptake of anthropogenic CO_2 also increases, because anthropogenic CO_2 penetrates faster into the deeper layers due to enhanced ventilation. The simulated seasonal cycle of pCO_2 in the Southern Ocean is generally larger than the estimates from the Takahashi *et al.* (2002) climatology or atmospheric inversions (Roy *et al.*, 2003; Gurney, 2004) indicate.

3. North Atlantic

The Atlantic is a strong sink for CO_2, and in the control run the flux north of 50°N is -0.31 PgC yr^{-1} on average. In the AR experiment the average CO_2 flux for the years 1990-1999 is -0.41 PgC yr^{-1}. Local areas in the North Atlantic show a strong interannual CO_2 flux variability, but the areas are small, the drivers of the variability are different and the variations are not in phase with each other. Overall, the simulated interannual CO_2 flux variability is rather small at ± 0.04 PgC yr^{-1}, which is in agreement with the simulation by McKinley *et al.* (2004).

Extrapolating the flux variability of an 18-year time series near Bermuda over the North Atlantic basin, Gruber *et al.* (2002) and Bates *et al.* (2002) postulate a possible variability of the CO_2 sink of ± 0.3 PgC yr^{-1}. According to results presented here, this is unlikely, because the drivers of the variability are not homogeneous over the whole basin. The dominating effect for the interannual variability of the CO_2 partial pressure in the subtropics and along the Gulf Stream is the dissolved inorganic carbon (DIC) concentration, while alkalinity variations are most important in the subpolar gyre. In this simulation, the drivers of the interannual variability are different to the drivers

of the seasonal cycle. The seasonal cycle of CO_2 partial pressure in the subpolar North Atlantic is largely driven by changes in the DIC, whereas temperature effects dominate the cycle in the subtropics.

4. Greenland, Iceland, Norwegian & Labrador Seas

The Greenland, Iceland and Norwegian (GIN) Seas and the Labrador Sea are areas of deep water formation. They are characterized by a downward transport of water and DIC into the deep ocean and an average CO_2 flux directed into the ocean. CO_2 flux, downward transport of DIC by ocean dynamics and biological export are highly correlated to the windspeed. In areas covered by sea-ice in winter, the simulation shows a negative correlation between the interannual variance of $\Delta p CO_2$ and the sea-to-air CO_2 flux. The CO_2 flux does not follow $\Delta p CO_2$, but $\Delta p CO_2$ rather follows the CO_2 flux, as determined by the gas exchange coefficient. In one sensitivity study, the variable sea-air gas exchange coefficient is replaced by an average value that is higher in summer. The CO_2 partial pressure in this region changes drastically, whereas the rest of the North Atlantic shows only minor differences.

Uptake of anthropogenic CO_2 is defined as the difference between the CO_2 fluxes of the AR experiment and the control run. The uptake of anthropogenic CO_2 is 1.65 PgC yr^{-1} for 1980-89 and 1.91 PgC yr^{-1} for 1990-99, with an accumulation of about 106 Pg of anthropogenic carbon by 1995 (table 6.5). The inventory estimate is compatible with results from chlorofluorocarbon (McNeil *et al.*, 2003) and from $\Delta C^\star$ technique estimates (Sabine *et al.*, 2004a). Subtropical surface waters have the highest concentrations of anthropogenic CO_2, while the lowest concentrations are found in the Southern Ocean and in upwelling regions such as the Equatorial Pacific. Only in North Atlantic Deep Water (NADW) do large concentrations of anthropogenic CO_2 penetrate to mid and abyssal depth. Although concentrations of anthropogenic carbon are low in the Southern Ocean, uptake rates of anthropogenic carbon are almost comparable to the deep water formation areas in the North Atlantic. The reason for this apparent paradox is that half of the anthropogenic CO_2 taken up by the Southern Ocean is transported northward into the subtropical convergence zone, a finding which is also supported by the study of Caldeira and Duffy (2000).

The interannual variability of the uptake of anthropogenic CO_2 is far less than the natural variability of the CO_2 fluxes (Figure 6.2). The phases of higher uptake mostly reflect deep mixing events in the Southern Ocean. In the 1990s, two large El Niño events interrupted the upwelling of intermediate-deep waters, which are low in anthropogenic CO_2, and thereby reduced the uptake of anthropogenic CO_2.

The regime shift in 1975-1977 reduced the mean outgassing of CO_2 in the equatorial Pacific in the control run from 0.70 PgC yr^{-1} to 0.58 PgC yr^{-1}. Nevertheless, the total sea-to-air flux increases by 0.006 PgC yr^{-1} per year on average. This trend is not due to the slowly increasing global sea surface temperatures, but it mainly originates in the southern hemisphere and is caused by the increasing wind stress. In the years 1980-89 and 1990-99 the total flux of CO_2 is about 0.18 PgC yr^{-1} smaller than the computed uptake of anthropogenic CO_2. However, the results have to be viewed with caution because of uncertainties in the observations and uncertainties in the model.

In addition, one has to keep in mind that the trends also depend on the initial conditions. The distribution of biogeochemical and physical ocean tracers at the beginning of the experiment reflect the mean state of the system over the 1620 years of initial integration time. In our case we have tuned the system to a cyclo-stationary state with a NCEP/NCAR forcing set detrended with respect to 1948. A long term trend shows how this initial distribution changes with the changing conditions, but no matter how good our model and the surface forcing is, the initial settings remain uncertain.

HAMOCC5 includes a dynamic biological model and the ecosystem dominates the seasonal cycle, but it is the changes in ocean circulation and mixing, acting on biogeochemical tracers such as DIC and alkalinity, that are the main cause of interannual variability and trends in the model. Nevertheless, this study underlines the fact that marine biology has a significant influence on the interannual variability by shaping the distribution of the biogeochemical tracers. An example is the effect that iron limitation has in the equatorial Pacific. The limited production changes the vertical DIC distribution and reduces the interannual CO_2 flux variability. This demonstrates that for a meaningful estimate of variability and trends, ocean dynamic and biological production have to be realistic and consistent with each other.

9. APPENDIX

Symbol	Description	Value
α_{if}	freezing sea-ice albedo	0.75
α_{im}	melting sea-ice albedo	0.70
α_{sf}	freezing snow albedo	0.85
α_{sm}	melting snow albedo	0.70
α_w	sea water albedo	0.10
λ	wind mixing stability parameter	0.03 kg m^{-3}
ε	emissivity of sea water	0.97
ρ_a	density of air	1.3 kg m^{-3}
ρ_i	density of sea-ice	910 kg m^{-3}
ρ_s	density of snow	330 kg m^{-3}
ρ_w	density of sea water	1025 kg m^{-3}
σ	Stefan-Boltzmann constant	5.5$\times$10^{-8} W m^{-2} K^{-4}
Λ_V	eddy viscosity relaxation coefficient	0.6
Λ_D	eddy diffusivity relaxation coefficient	0.6
c_a	specific heat capacity of air	1004 J kg^{-1} K^{-1}
c_w	specific heat capacity of sea water	4.0$\times$10^3 J kg^{-1} K^{-1}
e	ratio of principle axis of yield ellipse	2.0
g	acceleration due to gravity	9.81 m s^{-2}
k_i	thermal conductivity of sea ice	2.17 W m^{-1} K^{-1}
k_s	thermal conductivity of snow	0.31 W m^{-1} K^{-1}
z_0	wind mixing penetration depth	40 m
A_b	PP background vertical viscosity	1.0$\times$10^{-4} m^2 s^{-1}
A_w	PP wind mixing	5.0$\times$10^{-4} m^2 s^{-1}
A_{VO}	PP vertical viscosity parameter	1.0$\times$10^{-2} m^2 s^{-1}
B_H	biharmonic horizontal viscosity	1.1$\times$10^{-6} s^{-1} $\times$ $(\Delta x^4, \Delta y^4)$
BBL$_{max}$	maximum BBL thickness	500 m
C	empirical internal ice pressure const.	20
C_{RA}	PP viscosity tuning constant	5.0
C_{RD}	PP diffusivity tuning constant	5.0
C_W	ocean-ice stress bulk transfer	0.0045
D_b	PP background vertical diffusivity	1.0$\times$10^{-5} m^2 s^{-1}
D_H	harmonic horizontal diffusion	2.5 $\times$ 10^{-3} m s^{-1} $\times$ $(\Delta x, \Delta y)$
D_w	PP wind mixing	5.0$\times$10^{-4} m^2 s^{-1}
D_{VO}	PP vertical diffusivity parameter	1.0$\times$10^{-2} m^2 s^{-1}
L_f	latent heat of fusion	2.5 $\times$ 10^6 J kg^{-1}
L_s	latent heat of sublimation	2.834 $\times$ 10^6 J kg^{-1}
L_v	latent heat of vaporisation	2.5 $\times$ 10^6 J kg^{-1}
P^*	empirical internal ice pressure const.	5000 N m^{-1}
S_{ice}	salinity of sea-ice	5 psu
T_{freeze}	freezing temperature of sea water	-1.9°C
T_{melt}	melting temperature of sea ice/snow	0°C
W_T	wind mixing amplitude parameter	5.0$\times$10^{-4} m^2 s^{-1}

Tab. 9.1: Constants and parameters used in the ocean/sea ice model. Table is taken from Haak (2004).

Symbol	Description	Value
stoichiometry		
$R_{-O2:P}$	$-O_2$:P ratio	172 mol O_2 mol P^{-1}
$R_{C:P}$	C:P ratio	122 mol C mol P^{-1}
$R_{N:P}$	N:P ratio	16 mol N mol P^{-1}
$R_{Fe:P}$	Fe:P ratio	$6*10^{-4}$ mol Fe mol P^{-1}
upper ocean biogeochemistry: layers 1 to k_{eu}		
phytoplankton		
α	initial slope of P-vs-I curve	0.002 d^{-1} (W m-2)$^{-1}$
k_w	light attenuation coeff. of water	$4*10^{-2}$ m^{-1}
k_c	light attenuation coeff. of chlorophyll	$7.32*10^5$ m^{-1} (kmol P m^{-3})$^{-1}$
$R_{C:Chl}$	C:Chl ratio of phytoplankton	60 g C g Chl $^{-1}$
$K^{PO_4}_{PHY}$	half-sat. constant for PO_4 uptake	10^{-8} kmol P m^{-3}
$K^{SI(OH)_4}_{PHY}$	half-sat. constant for $Si(OH)_4$ uptake	10^{-6} kmol Si m^{-3}
$R_{Si:P}$	Opal:P uptake ratio	25 mol Si mol P^{-1}
$R_{Ca:P}$	$CaCO_3$:P uptake ratio	35 mol C mol P^{-1}
M_{CACO_3}	max. fraction of phytosynthesis as $CaCO_3$ production	0.2
PHY_0	min. concentration	10^{-11} kmol P m^{-3}
$\lambda^{surf}_{PHY,DET}$	mortality rate	0.008 d^{-1}
$\lambda_{PHY,DOM}$	exudation rate	0.003 d^{-1}
zooplankton		
μ_{ZOO}	max. grazing rate	0.08 d^{-1}
K_{ZOO}	half-saturation constant for grazing	$4*10^{-8}$kmol P m^{-3}
ZOO_0	min. concentration	10^{-11} kmol P m^{-3}
$1 - \epsilon_{ZOO}$	fraction of grazing egested	0.8
$\omega_{graz,ZOO}$	assimilation efficiency	0.5
$\lambda_{ZOO,DOM}$	excretion rate	0.006 d^{-1}
λ^{surf}_{ZOO}	mortality rate	0.0008 d^{-1}
ω_{mort,PO_4}	fraction of mortality as PO_4	0.95
dissolved organic matter		
$\lambda^{surf}_{DOM,PO_4}$	remineralization rate	0.0025 d^{-1}

Tab. 9.2: Parameters with their names in text and code in the biogeochemical model HAMOCC5.

Symbol	Description	Value
deep remineralization		
$\lambda_{\text{DET,PO}_4}^{deep}$	detritus remineralization rate	0.0025 d^{-1}
$\lambda_{\text{DOM,PO}_4}^{deep}$	DOM remineralization rate	0.003 d^{-1}
$\lambda_{\text{PHY,DET}}^{deep}$	phytoplankton mortality rate	0.01 d^{-1}
$\lambda_{\text{ZOO,DET}}^{deep}$	zooplankton mortality rate	0.002 d^{-1}
dissolution of opal and CaCO$_3$		
$\lambda_{\text{OPAL,SI(OH)}_4}$	opal dissolution rate	0.001 d^{-1}
$\lambda_{\text{CACO}_3\text{,DIC}}$	calcium carbonate disolution rate	dep. on saturation d^{-1}
others		
μ_{NFix}	nitrogen fixation rate	0.002 d^{-1}
$\epsilon_{Fe} \times S_{Fe}$	weight fraction of iron	6.267*10^{-6}
	in dust times iron solubility	
FE$_0$	limit value for excess diss. iron	0.6*10^{-9} kmol Fe m^{-3}
λ_{Fe}	complexation rate of excess diss. iron	0.000137d^{-1}

Tab. 9.3: Parameters with their names in text and code in the biogeo-chemical model HAMOCC5.

BIBLIOGRAPHY

Arrhenius, S., 1896. On the influence of carbonic acid in the air upon the temperature of the ground. *Philosophical Magazine*, **41**, 237.

Aumont, O., J. Orr, P. Monfray, W. Ludwig, P. Amiotte-Suchet and J. Probst, 2001. Riverine-driven interhemispheric transport of carbon. *Global Biogeochem. Cycles*, **15**, 393–405.

Bates, N., A. Pequignet, R. Johnson and N. Gruber, 2002. A short term sink for atmospheric CO_2 in subtropical mode water of the north atlantic ocean. *Nature*, **420**, 489–493.

Bender, M., T. Sowers and L. Labeyrie, 1994. The dole effect and its variations during the last 130,000 years as measured in the vostok ice core. *Global Biogeochem. Cycles*, **8**, 363–376.

Bopp, L., C. L. Quéré, M. Heimann, A. Manning and P. Monfray, 2002. Climate-induced oceanic oxygen fluxes: Implications for the contemporary carbon budget. *Global Biogeochem. Cycles*, **16**, doi:10.1029/2001GB001445.

Boyd, P. W. and et al., 2000. A mesoscale phytoplankton bloom in the polar southern ocean stimulated by iron fertilization. *Nature*, **407**, 695–702.

Broecker, W. and T.-H. Peng, 1982. *Tracer in the Sea*. Eldigio Press, Columbia University, Palisades, New York.

Caldeira, K. and P. Duffy, 2000. The role of the southern ocean in uptake and storage of anthropogenic carbon dioxide. *Science*, **287**, 620–622.

Chavez, F., J. Ryan, S. Lluch-Cota and M. . N. C., 2003. From anchovies to sardines and back: Multidecadal change in the pacifc ocean. *Science*, **299**, 217–221.

Chavez, F., P. Strutton, G. Friederich, R. Feely, G. Feldman, D. Foley and M. McPhaden, 1999. Biological and chemical response of the equatorial pacific ocean to the 1997/98 El Niño. *Science*, **286**, 2126–2131.

Chen, D., 2003. A comparison of wind products in the context of enso prediction. *Geophys. Res. Lett.*, **30**, 1107.

Cloern, J., C. Grenz and L. Videgar-Lucas, 1995. An empirical model of the phytoplankton:carbon ratio – the conversion factor between productivity and growth rate. *Limnology and Oceanography*, **40**, 1313.

Coale, K., S. Kenneth, S. Johnson, E. Fitzwater, R. M. Gordon, S. Tanner, F. Chavez, L. Ferioli, C. Sakamoto, P. Rogers, F. Millero, P. Steinberg, P. Nightingale, D. Cooper, W. Cochlan, M. Landry, J. Constantinou, G. Rollwagen, A. Trasvina and R. Kudela, 1996. A massive phytoplankton bloom induced by an ecosystem-scale iron fertilization experiment in the equatorial pacific ocean. *Nature*, **383**, 495–501.

Conkright, M., S. Levitus, T. O'Brien, T. Boyer, J. Antonov and C. Stephens, 1998. World ocean atlas 1998, cd-rom data set documentation. In *Tech. Rep. 15, NODC Internal Report*, p. 16 pp. Silver Spring, MD.

Cullen, H., R. D'Arrigo and E. Cook, 2002. Multiproxy reconstruction of the north atlantic oscillation. *Paleoceanography*, **16**, 27–39.

Dickson, A. and e. C. Goyet, 1994. Handbook of methods for the analysis of the various parameters of the carbon dioxide system in sea water. Technical report, ORNL/CDIAC-74.

Doney, S., K. Lindsay, K. Caldeira, J.-M. Campin, H. Drange, J.-C. Dutay, M. Follows, Y. Gao, A. Gnanadesikan, N. Gruber, A. Ishida, F. Joos, G. Madec, E. Maier-Reimer, J. C. Marshall, R. J. Matear, P. Monfray, A. Mouchet, R. Najjar, J. C. Orr, G.-K. Plattner, J. Sarmiento, R. Schlitzer, R. Slater, I. J. Totterdell, M.-F. Weirig, Y. Yamanaka and A. Yool, 2004. Evaluating global ocean carbon models: The importance of realistic physics. *Global Biogeochem. Cycles*, **18**, doi:10.1029/2003GB002150.

Dutay, D.-C., J. Bullister, S. Doney, J. Orr, R. Najjar, K. Caldeira, J.-M. Campin, H. Drange, M. Follows, Y. Gao, N. Gruber, M. Hecht, A. Ishida, F. Joos, K. Lindsay, G. Madec, E. Maier-Reimer, J. C. Marshall, R. Matear, P. Monfray, A. Mouchet, G.-K. Plattner, J. Sarmiento, R. Schlitzer, R. Slater, I. J. Totterdell, M.-F. Weirig, Y. Yamanaka and A. Yool, 2002. Evaluation of ocean model ventilation with cfc-11: comparison of 13 global ocean models. *Ocean Modelling*, **4**, 89–120.

Enting, I., T. Wigley and M. Heimann, 1994. Future emissions and concentrations of carbon dioxide: key ocean/atmosphere/land analysis. Tech. pap. 31, Div. of Atmos. Res., Commonw. Sci. and Ind. Res. Org., Melbourne, Australia.

Feely, R., J. Boutin, C. Cosca, Y. Dandonneau, J. Etcheto, H. Inoue, M. Ishii, C. L. Quéré, D. Mackey, M.McPhaden, N. Metzl, A. Poisson

and R. Wanninkhof, 2002. Seasonal and interannual variability of CO_2 in the equatorial pacific. *Deep-Sea Research II*, **49**, 2443–2469.

Feely, R., R. Wanninkhof, T. Takahashi and P. Tans, 1999. Influence of El Niño on the equatorial pacific contribution to atmospheric CO_2 accumulation. *Nature*, **398**, 597 pp.

Francey, R., P. Tans, C. Allison, I. Enting, J. White and M. Trolier, 1995. Changes in oceanic and terrestrial carbon uptake since 1982. *Nature*, **373**, 326–330.

Fung, I., S. Meyn, I. Tegen, S. Doney, J. John and J. Bishop, 2000. Iron supply and demand in the upper ocean. *Global Biogeochem. Cycles*, **14**, 281–295.

Gattuso, J.-P., M. Frankignoulle and R. Wollast, 1998. Carbon and carbonate metabolism in coastal aquatic ecosystems. *Annual Review of Ecology and Systematics*, **29**, 405–434.

Gent, P., J. Willebrand, T. McDougall and J. McWilliams, 1995. Parameterizing eddy-induced tracer transport in ocean circulation models. *J. Phys. Oceanogr.*, **25**, 463–474.

Gibson, J., P. Källberg, S. Uppala, A. Hernandez, A. Nomura and E. Serrano, 1997. ECMWF re-analysis project report. In *ERA description*, Volume 55 of *Project Rep. Series 1*, p. 72 pp. ECMWF, Reading, England.

Gruber, N., 1998. Anthropogenic CO_2 in the atlantic ocean. *Global Biogeochem. Cycles*, **12**, 165 pp.

Gruber, N. and C. Keeling, 2001. An improved estimate of the isotopic air-sea disequilibrium of CO_2: Implications for the oceanic uptake of anthropogenic CO_2. *Geophys. Res. Lett.*, **28**, 555–558.

Gruber, N., C. Keeling and N. Bates, 2002. Interannual variability in the north atlantic ocean carbon sink. *Science*, **298**, 2374–2378.

Gruber, N., J. L. Sarmiento and T. F. Stocker, 1996. An improved method for detecting anthropogenic CO_2 in the oceans. *Global Biogeochem. Cycles*, **10**, 809–837.

Gurney, e. a., K. R., 2004. Transcom 3 inversion intercomparison: Model mean results for the estimation of seasonal carbon sources and sinks. *Global Biogeochem. Cycles*, **18**, doi:10.1029/2003GB002111.

Gurney, K. e. a., 2002. Towards robust regional estimates of CO_2 sources and sinks using atmospheric transport models. *Nature*, **415**, 626–630.

Haak, H., 2004. *Simulation of Low-Frequency Climate Variability in the North Atlantic Ocean and the Arctic*, Volume 1. Max Planck Institute for Meteorology.

Hall, M. and H. Bryden, 1982. Direct estimates and mechanisms of ocean heat transport. *Deep Sea Res.*, **29**, 339–359.

Heimann, M. and E. Maier-Reimer, 1996. On the relations between the oceanic uptake of CO_2 and its carbon isotopes. *Global Biogeochem. Cycles*, **10**, 89–110.

Heinze, C., A. Hupe, E. Maier-Reimer, N. Dittert and O. Ragueneau, 2003. Sensitivity of the marine biospheric Si cycle for biogeochemical parameter variations. *Global Biogeochem. Cycles*, **17**, doi:10.1029/2002GB001943.

Heinze, C. and E. Maier-Reimer, 1999. The hamburg oceanic carbon cycle circulation model version "HAMOCC2s" for long time integrations. Technical Report 20, Deutsches Klimarechenzentrum, Modellberatungsgruppe, Hamburg.

Hibler, W., 1979. A dynamic thermodynamic sea ice model. *J. Phys. Oceanogr.*, **9**, 815–846.

Houghton, J., Y. Ding, D. Griggs, M. Noguer, P. van der Linden and D. X. (Eds.), 2001. Climate change 2001: The scientific basis, contribution of working group I to the third assessment report of the intergovernmental panel on climate change (IPCC). *Cambridge University Press, UK.*.

Hurrell, J., 1995. Decadal trends in the north atlantic oscillation: Regional temperatures and precipitation. *Science*, **269**, 676–679.

Hurrell, J., Y. Kushnir, G. Ottersen, and M. Visbeck, 2003. The north atlantic oscillation: Climate significance and environmental impact. *Eds. Geophysical Monograph Series*, **134**, 279 pp.

Johnson, K. S., R. M. Gordon and K. H. Coale, 1997. What controls dissolved iron concentrations in the world ocean? *Mar. Chem.*, **57**, 137–161.

Joos, F., R. Meyer, M. Bruno and M. Leuenberger, 1999. The variability in the carbon sinks as reconstructed for the last 1000 years. *Geophys. Res. Lett.*, **26**, 1437–1440.

Kalnay, E. et al., 1996. The NCEP/NCAR 40 year-reanalysis project. *Bull. Amer. Meteor. Soc.*, **77**, 437–470.

Keeling, C. and T. Whorf, 2004. Atmospheric CO_2 records from sites in the SIO air sampling network. In *Trends: A Compendium of Data on Global Change*. Carbon Dioxide Information Analysis Center, Oak Ridge National Laboratory, U.S. Department of Energy, Oak Ridge, Tenn., U.S.A.

Keeling, C., T. Whorf, M. Wahlen and J. van der Plicht, 1995. Interannual extremes in the rate of rise of atmospheric carbon dioxide since 1980. *Nature*, **375**, 666–670.

Keeling, R. and S. Shertz, 1992. Seasonal and interannual variations in atmospheric oxygen and implications for the global carbon cycle. *Nature*, **358**, 723–727.

Keeling, R., B. Stephens, R. Najjar, S. Doney, D. Archer and M. Heimann, 1998. Seasonal variations in the atmospheric O_2/N_2 ratio in relation to the air-sea exchange of O_2. *Global Biogeochem. Cycles*, **12**, 141–164.

Key, R., A. Kozyr, C. Sabine, R. W. K. Lee, J. Bullister, R. Feely, F. Millero, C. Mordy and T.-H. Peng, 2004. A global ocean carbon climatology: Results from GLODAP. *Global Biogeochem. Cycles*, p. In press.

Latif, M. and T. Barnett, 1994. Causes of decadal climate variability over the north pacific and north america. *Science*, **266**, 634–637.

Laws, E., P. Falkowski, W. Smith, H. Ducklow and J. McCarthy, 2000. Temperature effects on export production in the open ocean. *Global Biogeochem. Cycles*, **14**(4), 1231 pp.

Le Quéré, C., J. Orr, P. Monfray and O. Aumont, 2000. Interannual variability of the oceanic sink of CO_2 from 1979 through 1997. *Global Biogeochem. Cycles*, **14**, 1247–1265.

Lee, K., R. Wanninkhof, T. Takahashi, S. Doney and R.A.Feely, 1998. Low interannual variability in recent oceanic uptake of atmospheric cabon dioxide. *Nature*, **396**, 155 pp.

Lee, K. e. a., 2003. An updated anthropogenic CO_2 inventory in the atlantic ocean. *Global Biogeochem. Cycles*, **17**, doi:10.1029/2003GB002067.

Levitus, S., T. P. Boyer, M. E. Conkright, T. O'Brien, J. Antonov, C. Stephens, L. Stathoplos, D. Johnson and R. Gelfeld, 1998. World Ocean Database 1998: Volume 1: Introduction. NOAA Atlas NESDIS 18, Ocean Climate Laboratory, National Oceanographic Data Center, U.S. Gov. Printing Office, Wash., D.C.

Liss, P. and L. Merlivat, 1986. Air-sea exchange rates: introduction and synthesis. In *The role of air-sea exchange in geochemical cycle* (edited by P. Buat-Menard), pp. 113–127. NATO ASI Series Series C: Mathematical ad physical science.

Maier-Reimer, E., 1993. Geochemical cycles in an ocean general circulation model. preindustrial tracer distribution. *Global Biogeochem. Cycles*, **7**, 645–677.

Maier-Reimer, E. and K. Hasselmann, 1987. Transport and storage of CO_2 in the ocean - an inorganic ocean-circulation carbon cycle model. *Climate Dynamics*, **2**, 63–90.

Maier-Reimer, E., U. Mikolajewicz and A. Winguth, 1996. Future ocean uptake of CO_2 - interaction between ocean circulation and biology. *Climate Dynamics*, **12**, 711–721.

Mantua, N., S. Hare, Y. Zhang, J. Wallace and R. Francis, 1993. A pacific interdecadal climate oscillation with impacts on salmon production. *Bull. Amer. Meteor. Soc.*, **78**, 1069–1079.

Marland, G., T. Boden and R. J. Andres, 2004. In *Trends: A Compendium of Data on Global Change*. Carbon Dioxide Information Analysis Center, Oak Ridge National Laboratory, U.S. Department of Energy, Oak Ridge, Tenn., U.S.A.

Marsland, S. J., H. Haak, J. H. Jungclaus, M. Latif and F. Roeske, 2003. The Max-Planck-Institute global ocean/sea ice model with orthogonal curvilinear coordinates. *Ocean Modelling*, **5**, 91–127.

Martin, J. H. and S. E. Fitzwater, 1988. Iron deficiency limits phytoplankton growth in the northeast pacific subarctic. *Nature*, **331**, 341–343.

Matsumoto, e. a., K., 2004. Evaluation of ocean carbon cycle models with data-based metrics. *Geophys. Res. Lett.*, **31**, doi:10.1029/2003GL018970.

McKinley, G., M. J. Follows and J. Marshall, 2004. Mechanisms of air-sea CO_2 flux variability in the equatorial pacific and the north atlantic. *Global Biogeochem. Cycles*, **18**, doi:10.1029/2003GB002179.

McNeil, B., R. Matear, R.M.Key, J. Bullister and J. Sarmiento, 2003. Anthropogenic CO_2 uptake by the ocean based on the global chlorofluorocarbon data set. *Science*, **299**.

McPhaden, M. and D. Zhang, 2002. Slowdown of the meridional overturning circulation in the upper pacific ocean. *Nature*, **415**, 603–608.

Metzl, N., B. Tilbrook and A.Poisson, 1999. The annual fco_2 cycle and the air-sea CO_2 flux in the sub-antarctic ocean. *Tellus, Ser. B*, **51**, 849–861.

Monterey, G. and S. Levitus, 1997. Climatological cycle of mixed layer depth in the world ocean. NOAA Atlas NESDIS 18, Ocean Climate Laboratory, National Oceanographic Data Center, U.S. Gov. Printing Office, Wash., D.C.

Nightingale, P., G. Malin, C. Law, A. Watson, P. Liss, M. Liddicoat, J. Boutin and R. Upstill-Goddard, 2000. In situ evaluation of air-sea gas exchange parameterizations using novel conservative volatile tracers. *Global Biogeochem. Cycles*, **14**(1), 373–387.

Obata, A. and Y. Kitamura, 2003. Interannual variability of sea-air exchange of CO_2 from 1961 to 1998 with a global ocean circulation biogeochemistry model. *J. Geophys. Res.*, **108**, doi:10.1029/2001JC001088.

Oberhuber, J., 1988. An atlas based on the COADS data set: The budget of heat, buoyancy and turbulent kinetic energy at the surface of the global ocean. Technical Report 15, Max-Planck Institut für Meteorologie (MPI).

Orr, J., 2001. Global ocean storage of anthropogenic carbon. *(GOSAC), Final Report*, **1**, Contract ENV4–CT97–0495.

Orr, J., E. Maier-Reimer, U. Mikolajewicz, P. Monfray, J. Sarmiento, J. Toggweiler, N. Tayler, J. Palmer, N. Gruber, C. Sabine, C. L. Quéré, R. Key and J. Boutin, 2001. Estimates of anthropogenic carbon uptake from four three-dimensional global ocean models. *Global Biogeochem. Cycles*, **15**, 43–60.

Rayner, P., I. Enting, R. Francey and R. Langenfelds, 1999a. Reconstructing the recent carbon cycle from atmospheric CO_2, $\Delta13C$ and N_2/O_2 observations. *Tellus, Ser. B*, **51**, 213–232.

Rayner, P., R.Law and R. Dargaville, 1999b. The relationship between tropical CO_2 fluxes and the El Niño southern oscillation. *Geophys. Res. Lett.*, **26**, 493–496.

Revelle, R. and H. Suess, 1957. Carbon dioxide exchange between atmosphere and ocean and the question of an increase of atmospheric CO_2 during the past decades. *Tellus*, **9**, 18–27.

Rödenbeck, C., S. Houweling, M. Gloor and M. Heimann, 2003. CO_2 flux history 1982-2001 inferred from atmospheric data using a global inversion of atmospheric transport. *Atmos. Chem. Phys.*, **3**, 1919–1964.

Roemmich, D. and C. Wunsch, 1985. Two transatlantic sections: meridional circulation and heat flux in the subtropical north atlantic ocean. *Deep Sea Res.*, **32**, 619–664.

Roy, T., P. Rayner, R. Matear and R. Francey, 2003. Southern hemisphere ocean CO_2 uptake: reconciling atmospheric and oceanic estimates. *Tellus, Ser. B*, **55**, 701–710.

Sabine, C., R. Feely, N. Gruber, R.M.Key, K. Lee, J.L.Bullister, R. Wanninkhof, C. Wong, D. Wallace, B. Tilbrook, F.J.Millero, T.-H. Peng, A. Kozyr, T. Ono and A. Rios, 2004a. The oceanic sink for anthropogenic CO_2. *Science*, **305**, 367–371.

Sabine, C., R. Feely, R. Key, J. Bullister, F. Millero, K. Lee, T.-H. Peng, B. Tilbrook, T. Ono and C. S. Wong, 2002. Distribution of anthropogenic CO_2 in the pacific ocean. *Global Biogeochem. Cycles*, **16**, doi:10.1029/2001GB001639.

Sabine, C., M. Heimann, P. Artaxo, D. Bakker, C.-T. Chen, C. Field, N. Gruber, C. L. Quéré, R. Prinn, J. Richey, P. Lankao, J. Sathaye and R. Valentini, 2004b. Integrating humans, climate, and the natural world. In *The Global Carbon Cycle* (edited by B. Christopher, M. Raupach and R. Victoria), Volume 62 of *SCOPE*, pp. 17–44. Island Press, Washington DC.

Sabine, C., R. Key, K. Johnson, F. Millero, A. Poisson, J. Sarmiento, D. Wallace and C. Winn, 1999. Anthropogenic CO_2 inventory of the indian ocean. *Global Biogeochem. Cycles*, **13**, 179–198.

Saltzmann, X., 1993. *J. Geophys. Res.*, **98**, 16481–16486.

Sarmiento, J., J. Dunne, A. Gnanadesikan, R. Key, K. Matsumoto and R. Slater, 2002. A new estimate of the $CaCO_3$ to organic carbon export ratio. *Global Biogeochem. Cycles*, **16**, doi:10.1029/2002GB001919.

Sarmiento, J. and N. Gruber, 2004. *Chapter 8: The Ocean Carbon Cycle*, Volume 1. Textbook in preparation, Princeton University Press.

Sarmiento, J., P. Monfrey, E. Maier-Reimer, O.Aumont, R.J.Murnane and J. Orr, 2000. Sea-air CO_2 fluxes and carbon transport: A comparison of three ocean general circulation models. *Global Biogeochem. Cycles*, **14**, 1267–1281.

Sarmiento, J., R. Slater, R. Barber, L. Bopp, S. Doney, A. Hirst, J. Kleypas, R. Matear, U. Mikolajewicz, P. Monfray, V. Soldatov, S. A. Spall and R. Stouffer, 2004. Response of ocean ecosystems to climate warming. *Global Biogeochem. Cycles*, **18**, doi:10.1029/2003GB002134.

Schlitzer, R., 2000. Applying the adjoint method for biogeochemical modeling: export of particulate organic matter in the world ocean. *Geophysical Monograph Series*, **114**, 107–124.

Six, K. and E. Maier-Reimer, 1996. Effects of plankton dynamics on seasonal carbon fluxes in an ocean general circulation model. *Global Biogeochem. Cycles*, **10**(4), 559–583.

Storch, H. v. and F.W.Zwiers, 1999. *Statistical Analysis in Climate Research*. Cambridge University Press, Trumpington Street, Cambridge CB2 1RP, UK.

Sweby, P., 1984. High resolution schemes using flux limiters for hyperbolic conservation laws. *SIAM J. Numer. Anal.*, **21**, 995–1011.

Takahashi, T., J. Olafsson, J. Goddard, D. Chipman and S. Sutherland, 1993. Seasonal variation of CO_2 and nutrients in the high-latitude surface oceans: A comparative study. *Global Biogeochem. Cycles*, **7**, 843–878.

Takahashi, T., S. Sutherland, C. Sweeney, A. Poisson, N. Metzl, B. Tilbrook, N. Bates, R. Wanninkhof, R. Feely, C. Sabine, J. Olafsson and Y. Nojiri, 2002. Global sea-air CO_2 flux based on climatological surface ocean pCO_2, and seasonal biological and temperature effects. *Deep-Sea Research II*, **49**, 1601–1622.

Thompson, D. W. J. and S. Solomon, 2002. Interpretation of recent southern hemisphere climate change. *Science*, **296**, 895–899.

Timmreck, C. and M. Schulz, 2004. Significant dust simulation differences in nudged and climatological operation mode of the AGCM ECHAM. *J. Geophys. Res.*, **109**, doi:10.1029/2003JD004381.

Trenberth, K. and J. Hurrell, 1994. Decadal atmosphere-ocean variations in the pacific. *Climate Dyn.*, **9**, 303–319.

Trenberth, K. E. and A. Solomon, 1994. The global heat balance: heat transports in the atmosphere and ocean. *Clim. Dyn.*, **10**, 107–134.

Volk, T. and M. Hoffert, 1985. Ocean carbon pumps: Analysis of relative strengths and efficiencies in ocean-driven atmospheric CO_2 changes. *Geophysical Monograph Series*, **32**, 99 pp.

Völker, C., D. Wallace and D. Wolf-Gladrow, 2002. On the role of heat fluxes in the uptake of anthropogenic carbon in the north atlantic. *Global Biogeochem. Cycles*, **16**, Art. No. 1138.

Wanninkhof, R., 1992. Relationship between wind speed and gas exchange over the ocean. *J. Geophys. Res.*, **97**, 7373–7382.

Weiss, R., 1970. The solubility of nitrogen, oxygen and argon in water and sea water. *Deep-Sea Res.*, **17**, 721–735.

Winguth, A., M. Heimann, K. Kurz, E. Maier-Reimer, U. Mikolajewicz and J. Segschneider, 1994. El Niño-southern oscillation related fluctuations of the marine carbon cycle. *Global Biogeochem. Cycles*, **8**, 39–63.

Zeebe, R. and D. Wolf-Gladrow, 2001. *CO_2 in seawater: equilibrium, kinetics,isotopes*, Volume 1. Elsevier Oceanographiy Series.

Zeng, N., A. Mariotti and P. Wetzel, 2004. Mechanisms of interannual CO_2 variability. *Global Biogeochem. Cycles*, **submitted**.

Zhang, D., M. McPhaden and E. Williams, 2003. Oberservational evidence for flow between the subtropical and tropical Atlantic: the Atlantic Subtropical Cells. *J. Phys. Oceanogr.*, p. submitted.

Acknowledgments

Beginn einer neuen Veröffentlichungsreihe des MPIM, welche die vorherigen Reihen "Reports" und "Examensarbeiten" weiterführt:

"Berichte zur Erdsystemforschung" , "Reports on Earth System Science", ISSN 1614-1199
Sie enthält wissenschaftliche und technische Beiträge, inklusive Dissertationen.